

NONLINEAR OPTICAL PROPERTIES OF LEAD
SILICATE AND EUROPIUM-DOPED
ALKALI-SILICATE GLASSES

By

SHABBIR M. MIAN

Bachelor of Science

Berea College

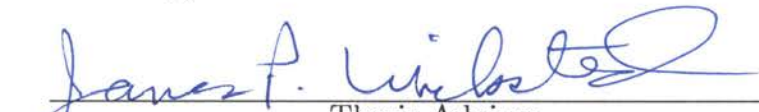
Berea, Kentucky

1990


Submitted to the Faculty of the
Graduate College of the
Oklahoma State University
in Partial fulfillment of
the Requirements for
the Degree of
DOCTOR OF PHILOSOPHY
December, 1996

NONLINEAR OPTICAL PROPERTIES OF LEAD
SILICATE AND EUROPIUM-DOPED
ALKALI-SILICATE GLASSES

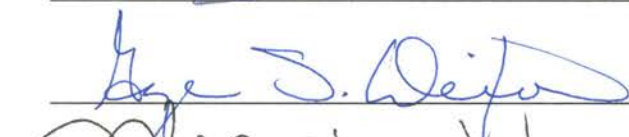
Thesis Approved:

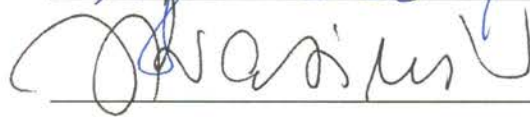



Thesis Adviser



Bull







Dean of the Graduate College

Dedicated to my Mom and Dad

ACKNOWLEDGMENT

Many people have contributed to this dissertation, either directly or indirectly, and it is only fair that I acknowledge their support. I would first like to thank my dissertation advisor Dr. Jim Wicksted for giving me the opportunity to work with him. He has always guided me with a gentle hand and offered kind words of encouragement when needed most. I am very grateful to him for his friendship, inspiration, and support throughout the doctoral program. I would also like to thank Carol Wicksted for her love and support. I am indebted to her for taking good care of me during my wisdom teeth extraction and stuffing me with pumpkin pie during the holidays.

I would like to thank my other dissertation committee members, Drs. J. J. Song, G. Dixon, B. Ackerson, and J. Krasinski. I have benefited from their thought-provoking questions and insights. The education I received from the OSU physics department faculty has been exceptional. Drs. L. Scott, S. Nandi, P. Westhaus and R. Hauenstein have been very instrumental in piquing my interest in physics. I am very grateful to the faculty and staff at the physics department for making my stay at OSU memorable.

Abdulatif Hamad has been a fellow graduate student in the Wicksted research group for the last five years. We have grown to be very good friends over the years, and I have benefited tremendously from our friendship. I would also like to thank Bahman Taheri for giving me sound experimental and theoretical

advice and being a good friend. I thank all the other graduate students who have helped me during my stay at OSU.

I would like to thank my parents for the love and support they have given me all my life. They provided a stable and nurturing environment that enabled me to grow. Their faith in my abilities instilled confidence in me. If I had a choice in deciding whom my parents would be, I would most definitely choose them. The hard work and perseverance of my brother Shahid have inspired me never to give up. I am most grateful to my brother Anwar for the love and understanding he has given me over the years. My sister-in-law Maya and my beautiful niece Shafia and nephew Munna have always brought a smile to my face. I thank all the members of my family for their love and moral support.

I would like to thank Pam Gerassimides for her love and endless support both at Berea College and during my stay at OSU. At times when I found it difficult to continue, she provided moral encouragement. She has experienced the ups and downs of the doctoral program with me through our daily conversations. I am eternally grateful to her for always being there for me.

This dissertation would not have been possible without the glass samples. I gratefully acknowledge D. H. Blackburn of N.I.S.T for providing the lead silicate glasses and Eu-doped alkali-silicate glasses with systematic alkali variation. I would also like to acknowledge P. L. deRochemont of C² Technologies for providing the Eu-doped alkali-silicate glasses with systematic Eu variation.

Above all, I would like to thank Allah for his many blessings and guidance. I hope and pray that I may use the knowledge that I have gained for the benefit of humanity. As acquiring knowledge is an unending process, I pray that I am given the strength to continue to learn.

TABLE OF CONTENTS

Chapter	Page
I. INTRODUCTION.....	1
II. THEORY	6
1. Nonlinear Optics	6
(a) Z-scan.....	9
(i) Introduction	9
(ii) Theory.....	15
(iii) Theoretical Results.....	19
(b) Intensity-scan	23
(i) Introduction	23
(ii) Theory.....	24
(iia) Closed aperture.....	29
(iib) Open aperture.....	32
(iii) Theoretical Results.....	33
2. Brillouin Scattering	35
III. EXPERIMENT	42
1. Z-scan and Optical Limiting.....	42
2. Intensity-scan (nanosecond)	47
3. Intensity-scan (millisecond).....	51
4. Brillouin Scattering	60
5. Temperature-dependent absorption measurements	64
6. Refractive index and density measurements.....	67
IV. RESULTS AND DISCUSSION	72
1. Lead Silicate.....	72
(a) Structure and Properties	72
(b) Brillouin Scattering	80
(c) Temperature-dependent absorption measurements.....	97
(d) Intensity-scan (millisecond).....	105
(e) Z-scan and Optical Limiting	113
2. Eu-doped Alkali-Silicate.....	124
(a) Brillouin Scattering	124
(b) Intensity-scan (nanosecond)	131
(c) Intensity-scan (millisecond).....	137

Chapter	Page
V. SUMMARY AND RECOMMENDATIONS	142
BIBLIOGRAPHY	145
APPENDICES	150
A. Effects of beam ellipticity on Z-scan measurements	151
B. Elliptic beam propagation in Kerr medium	163
C. Tandem Fabry-Perot Interferometer	170

LIST OF TABLES

Table	Page
III.1 Sample designation and relevant parameters for lead silicate glasses.....	43
III.2 Nomenclature and composition for Eu-doped alkali-silicate glasses with systematic Eu variation.....	49
III.3 Nomenclature and composition for Eu-doped alkali-silicate glasses with dual alkali ions	49
III.4 Refractive index, absorption coefficient, density and sample thickness values of all Eu ³⁺ -doped alkali-silicate glasses.....	50
III.5 Nomenclature and composition for Eu-doped alkali silicate glasses where M = Li, Na, K, Rb, and Cs	52
III.6 The linear index of refraction, absorption coefficient, and sample thickness values of lead silicate glasses and Eu-doped alkali-silicate glasses.....	52
IV.1 The density, refractive index and Brillouin shifts for lead silicate glasses for a right-angle geometry	84
IV.2 The velocities of the LA and TA phonons and their corresponding elastic constants of the lead silicate glasses obtained from a right-angle scattering geometry.....	86
IV.3 The Brillouin shift of the LA phonon, and its corresponding velocity and elastic constant for lead silicate glasses obtained in a back-scattering geometry	86
IV.4 Poisson's ratio, Young's Modulus and bulk modulus for lead silicate glasses. The values for L42 for could not be calculated because no TA phonon was detected.....	89
IV.5 The ξ value and correction factors for the lead silicate glasses	92
IV.6 The photoelastic constants of the lead silicate glasses and ratio of integrated intensity for the TA to LA phonon	93
IV.7 The lattice and atomic effects and p_{44} of the lead silicate glasses	95

Table	Page
IV.8 The UV cutoff wavelength λ_c , the slope $d\lambda_c/dT$ and the corresponding “optical band-gap” E_0 for the lead silicate glasses.....	103
IV.9 Values of γ_{th} , L_{eff} , and transmission slopes of the lead glasses.....	108
IV.10 Values of β_{ex} and $(dn/dT)_{\sigma \neq 0}$ for the lead glasses	112
IV.11 Values of the nonlinear refraction and absorption coefficients	120
IV.12 Values of the electrostrictive nonlinear refraction coefficients	123
IV.13 The density, refractive index, and Brillouin shifts for the Eu-glasses....	125
IV.14 The sound velocities, and elastic constants for the Eu-glasses	125
IV.15 Young’s modulus, Poisson’s ratio, and Bulk modulus of Eu-glasses	127
IV.16 Correction factors for the Eu-doped alkali-silicate glasses.....	129
IV.17 The photoelastic constants of the Eu-doped alkali-silicate glasses.....	129
IV.18 Nonlinear refraction coefficient, ratio of slopes and density values of the Eu-doped alkali-silicate glasses.....	133
IV.19 The thermal nonlinear refraction coefficients for the alkali-silicate glasses along with the absorption coefficients.....	139
IV.20 The laser induced stress dn/dT for the alkali-silicate glasses along with photoelastic constants and Poisson’s ratio	141
IV.21 The electrostrictive contribution to the total nonlinear refraction coefficient along with LA sound velocity and density.....	141

LIST OF FIGURES

Figure	Page
II.1 Setup for Z-scan experiment.....	10
II.2 A positive nonlinearity is used to demonstrate the Z-scan technique.....	11
II.3 Typical Z-scan signature for a (a) closed and (b) open aperture.....	13
II.4 Theoretical plots of Z-scan showing the effects of (a) the nonlinear absorption coefficient β (in cm/GW) with $\gamma = 6 \times 10^{-19}$ m ² /W, and (b) the nonlinear refraction coefficient γ (in 10 ⁻¹⁹ m ² /W) with $\beta = 0$ cm/GW	21
II.5 Theoretical plots of (a) Z-scan and (b) optical limiting of beams with ellipticity $e = 1, 2,$ and 4	22
II.6 (a) Theoretical plot of closed aperture Intensity-scan with positive nonlinearity, and sample positions before and after the focus. (b) Theoretical plot of open aperture intensity-scan with positive nonlinear absorption.....	34
II.7 Diagram for first-order photon-phonon scattering.....	36
III.1 Setup for Z-scan/Optical Limiting	45
III.2 Setup for Intensity-scan.....	55
III.3 Pulse distortions for L62 at different input powers	58
III.4 Intensity-scan for L62.....	59
III.5 Experimental setup for right-angle Brillouin Scattering.....	62
III.6 Experimental setup for temperature-dependent absorption measurements.....	66
III.7 Setup for measuring the refractive index using a CCD camera and laser beam profiler.....	69
IV.1 Possible structures of lead silicate glass for high PbO content after Mydlar <i>et al.</i>	75

Figure	Page
IV.2 Raman scattering from binary lead silicate glasses with PbO concentrations of 32, 42, 52, 62% all in mole %	79
IV.3 Brillouin spectra for lead silicate glasses in a back-scattering geometry. (a) L32; (b) L42; (c) L52; (d) L62.....	82
IV.4 Brillouin spectra for lead silicate glasses in a right-angle scattering geometry. (a) L32; (b) L42; (c) L52; (d) L62	83
IV.5 Elastic properties of the lead silicate glasses	88
IV.6 Density-dependence of the photoelastic constants for lead glasses	94
IV.7 The absorption coefficients of lead silicate glasses.....	99
IV.8 Temperature-dependent absorption measurements for L32 to L62.....	101
IV.9 The temperature dependence of the UV cutoff wavelength for the lead silicate glasses	103
IV.10 Intensity-scan data for the lead silicate glasses	106
IV.11 The change in refractive index for the lead silicate glasses.....	106
IV.12 Z-scan/Optical Limiting data for L62 using a 1 mm thick sample.....	115
IV.13 Z-scan/Optical Limiting data for L62 using a 1.5 mm thick sample.....	116
IV.14 Optical Limiting data for all the lead silicate glasses. The thicknesses are (a) 1 mm thick, and (b) 1.5 mm thick	119
IV.15 Eu concentration dependence of the elastic constants of B5 to B10.....	126
IV.16 Eu concentration dependence of the photoelastic constants of B5 to B10.....	128
IV.17 Intensity-scan data for B10. (a) closed-aperture, and (b) open-aperture. $\gamma = 21 \times 10^{-7} \text{ cm}^2/\text{GW}$	132
IV.18 Plot of the nonlinear refraction coefficient for B5 through B10 and also showing fused quartz.....	134
IV.19 Intensity-scan data for the Eu-doped alkali silicate glasses	138
IV.20 The change in refractive index for the Eu-doped alkali silicate glasses.....	138
IV.21 Plot of γ_{th} versus α for the Eu-doped alkali silicate glasses	140
A.1 A contour plot of the closed aperture transmission.....	158

Figure	Page
A.2	Specific examples of the effects of beam ellipticity on the closed aperture Z-scan signature..... 159
A.3	A beam with an ellipticity of $e = 5.5$ ($w_y = 1.1$ mm, $w_x = 0.2$ mm) and a sample nonlinearity of $\Delta\Phi_0 = 0.1$, is shown in a closed aperture Z-scan where an extra peak is observed 160
A.4	The nonlinear decrease of the ratio $\Delta T_{p-v}/\Delta\Phi_0$ as a function of ellipticity 160
A.5	A contour plot of the open aperture transmission..... 161
A.6	Specific examples of the effects of beam ellipticity on an open aperture Z-scan signature..... 162
A.7	An open aperture Z-scan for a beam with waists $w_y = 0.8$ mm, and $w_x = 0.2$ mm and a focusing lens of 250 mm is shown 162
B.1	Elliptic beam propagation in Kerr media. In (a) $P=2.5$ KW, (b) $P=10$ KW,(c) $P=20$ KW, and (d) $P=21.25$ KW..... 168
B.2	Elliptic beam propagation in Kerr media. In (a) $P=22$ KW, (b) $P=31.25$ KW, (c) $P=42.5$ KW, and (d) $P=44$ KW..... 169
C.1	A transmission spectrum of a Fabry-Perot interferometer 172
C.2	Compound translation stage of the FP interferometer with two mirrors mounted on the stage 173
C.3	Reflection spectra of the tandem FP interferometer..... 176
C.4	Brillouin spectra of Si (001) showing bulk transverse (T) and longitudinal (L), surface phonon (R), and central mode with the Rayleigh line using 514.5 nm..... 177

CHAPTER I

INTRODUCTION

The focus of this dissertation is the nonlinear optical properties of binary lead silicate and Eu-doped alkali-silicate glasses. Nonlinear optics is a very important field of physics that deals with the study of light-matter interaction under intense laser illumination. Among the many nonlinear optical responses of a material, self-focusing is one that is well understood. This effect manifests itself by changing the index of refraction of the material. The nonlinear effect that we discuss and study in the dissertation is the third-order nonlinear optical process of self-focusing inasmuch as is relevant to our glasses.

Glasses have a special place among the variety of materials that are investigated by nonlinear optical techniques. They are easily fabricated and can be drawn into fibers. They also have other useful properties, such as negligible linear loss, that makes them highly desirable to the communications industry. Glasses with large nonresonant nonlinear refraction coefficients are good candidates for all-optical switching. They have fast electronic response times and small two-photon absorption coefficients at the infra-red wavelengths used for communications. There is also a fundamental interest in the nonlinear optical properties of glasses. At the basic physics level, there is not a clear understanding of the origin and dispersion of the nonlinear refraction coefficient in glasses. Two-photon absorption in glasses is also poorly understood since glasses do not have

long-range periodicity like semiconductors and hence a direct application of a two-band model is questionable.

The objective of our study was to characterize the nonlinear optical properties of these glasses on nanosecond and millisecond time scales. We investigated two different categories of glasses. The first category included lead silicate glasses where the PbO concentration was varied systematically and forms a family of its own. The second category had two families of Eu-doped alkali-silicate glasses. The first family consisted of sodium alkali-silicate based glasses that had a systematic variation of Eu concentration. This family also had two samples with dual-alkali ions. The glasses in the second family had the same percent of Eu but varied the alkali ion systematically from Li to Cs. We studied the effects of composition on the self-focusing properties of each family of glasses on both time-scales.

Since self-focusing arises from a change in the refractive index, it is convenient to denote this index change as $\Delta n = \gamma I$, where I is the intensity and γ is the nonlinear refraction coefficient. The parameter γ characterizes the nonlinearity of the material and is directly related to the third-order nonlinear susceptibility $\chi^{(3)}$. Finding the value of γ for glasses within a family will provide information as to what microscopic or macroscopic material properties affect it. Therefore, we have explored the nonlinearities of the glasses in terms of their γ values.

The nonlinear optical properties of the glasses were investigated using the well-established Z-scan and, more recent, related Intensity-scan techniques. The beam used in our Z-scan experiment was of elliptic Gaussian spatial profile and it was necessary to incorporate the beam ellipticity in our modeling. Thus, we generalized the theory behind these two techniques that was originally applicable only to circular Gaussian beams to account for a beam with *any* ellipticity. A

Gaussian beam-optics theory for optically *thin* media and a wave-optics theory for optically *thick* media were developed for the case of an elliptic Gaussian beam. The theories predict new features to occur in the Z-scan signature.

Although the same experiments were performed on each glass in a given family, they were not performed on all the families. This was due to sample availability and time constraints. The elliptic beam Z-scan and Optical Limiting experiments were performed on the lead silicate glasses on a nanosecond time scale from which we were able to derive the nonlinear refraction and nonlinear absorption coefficients. The Optical Limiting experiment on the lead silicate glasses was part of a larger project that was conducted to find glasses that would safely limit dangerous levels of laser radiation so as to protect sensitive devices. The nanosecond Intensity-scan was performed only on the first family of Eu-doped alkali-silicate glasses. We should point out that this is the first such application of the Intensity-scan technique to a nanosecond time-scale. To investigate thermal nonlinearities, we developed a highly sensitive version of the Intensity-scan technique for the millisecond time-scale. As this technique is new, not all of its features have been fully explored. However, we were able to derive γ values that arose predominantly from thermal effects for the lead silicate and the second family of Eu-doped alkali-silicate glasses. We also performed temperature-dependent absorption measurements on the lead silicates to compliment the thermal lensing experiments. Brillouin scattering measurements were performed on the lead silicate and the first family of Eu-doped alkali-silicate glasses to study their elastic and photoelastic properties. More importantly, Brillouin scattering provided information that could be used to evaluate the effects of laser-induced stress on our nonlinear optical measurements such as electrostriction and stress-induced contribution to the thermo-optic coefficient.

In Chapter II, we present the theory behind our nonlinear optical and Brillouin scattering measurements. The first part of the chapter concerns nonlinear optics. After a brief discussion of what is meant by optical nonlinearity, we discuss the theory behind the Z-scan and Intensity-scan techniques that were used in our experiments. The elliptic beam Z-scan theory for optically *thick* media is first presented. It is based on a Gaussian beam-optics approach. Next, we present the wave-optics version of the elliptic beam Intensity-scan theory that is applicable to optically *thin* medium. The chapter concludes with the well-known Brillouin scattering theory for isotropic media that was used to study the elastic and photoelastic properties of the glasses.

Chapter III details the experimental techniques employed in the study of the nonlinear optical properties of the glasses. Some of the experimental problems that were encountered and methods devised to circumvent these difficulties are also included. The sample compositions and nomenclature used to describe the glasses are presented in this chapter. The nanosecond Z-scan technique using an elliptic Gaussian beam is first presented. This section is followed by the nanosecond Intensity-scan technique. The next section is about the millisecond version of the Intensity-scan technique we developed to study thermal nonlinearities of glasses. The Brillouin scattering experimental procedure using a Fabry-Perot interferometer of the Sandercock design is then described. The temperature-dependent absorption measurements are then discussed. The experimental chapter concludes with a very quick and accurate method of determining the refractive index of materials based on the Brewster's angle technique that we developed and used to measure the refractive index of some of the glasses.

Chapter IV contains the results and discussion of our experimental findings. The chapter consists of lead silicate and Eu-doped alkali-silicate parts. In

the lead silicate part, we first try to synthesis a structural model from several x-ray diffraction data and other structural studies that have been done. This is particularly difficult to do since the sources are not all in agreement with each other regarding the structure of lead silicate glasses. The Brillouin scattering results are then presented which we try to interpret with the available structural models. The next section consists of the temperature-dependent absorption measurements that helped us understand our thermal lensing measurements better. The millisecond Intensity-scan results are then presented. These focus on the thermal nonlinearity of these glasses including the effects of laser-induced stress. Finally, the nanosecond Z-scan results are described.

The last part of Chapter IV contains the results and discussion for the Eu-doped alkali-silicate glasses. The Brillouin scattering results of the first family of Eu-doped glasses are shown in a series of tables and discussed. The nanosecond Intensity-scans of the same set of glasses are then described and interpreted in terms of the hyperpolarizability of ions. The results and discussion chapter concludes with the millisecond Intensity-scans of the second family of Eu-doped alkali silicate glasses where we try to assess the contribution of laser-induced stress to the conventional value of the thermo-optic coefficient.

In Chapter V, we summarize the main conclusions and findings of the dissertation and offer some ideas and recommendations for future work.

There are three appendices. The first appendix contains the discussion of the effects of beam ellipticity to the Z-scan signature. The second appendix investigates the propagation of elliptic Gaussian beams in a Kerr medium. The third appendix contains a brief discussion of the Sandercock Fabry-Perot system that was used in the Brillouin scattering experiments.

CHAPTER II

THEORY

1. Nonlinear Optics

The optical properties of materials are, in general, independent of the light intensity for the relatively low illuminations that occur in nature. However, this does not hold true when the illumination is high and the properties become dependent on the intensity and other characteristics of the light. Typically, only lasers can provide sufficient intensity to affect the optical properties of materials. The material response to an applied optical field will then depend on the strength of the optical field in a nonlinear manner. Nonlinear Optics is the study of such light-matter interaction.

To clarify what we mean by optical nonlinearity, let us consider the material system to be composed of many charged particles: negatively charged electrons bound harmonically to positively charged ion cores. This treatment of the atom as a harmonic oscillator is known as the Lorentz model. A static electric field applied to the material will cause the charged particles to separate forming dipoles, i.e., it will polarize the material. When an optical electric field with frequencies of 10^{13} to 10^{17} Hz is incident on the material, it will induce many oscillating dipoles. Since the ratio of the electric force over the magnetic force exerted on the particles goes as v/c , the effect of the optical magnetic field is much

weaker and is neglected. The mass of the positively charged nucleus is much heavier than the electrons, and it is the motion of the electrons that is significant. If the electron displacement is x , then its motion will be governed by

$$\ddot{x} + 2\Omega\dot{x} + \omega_0^2 x + \left\{ ax^2 - bx^3 + \dots \right\} = -eE(t)/m \quad (\text{II.1})$$

where Ω is a damping constant, $-e$ is the charge of the electron, m is its mass, and $E(t)$ is the applied optical electric field. The dots above the x represent time derivatives. The terms in brackets are higher order corrections to the restoring force or equivalently to the potential energy function. It is these terms that are responsible for nonlinear optical phenomenon.

Another way of expressing the optical nonlinearity is through the macroscopic polarization or dipole moment per unit volume P . This is done through a Taylor series expansion of the polarization in terms of the electric field as

$$P = \epsilon_0 \left\{ \chi^{(1)} E + \chi^{(2)} E^2 + \chi^{(3)} E^3 + \dots \right\} \quad (\text{II.2})$$

where we have neglected the tensorial nature of the relationship as well as the explicit frequency dependence. Here, $\chi^{(n)}$ is the n th-order susceptibility, and $\chi^{(1)}$ is the familiar linear susceptibility. The effects caused by $\chi^{(n)}$ are known as n th order nonlinearities. We will be concerned only with the third order. By simply substituting $E(t) = E_0 \cos(\omega t)$ into Eq. II.2, we find the third-order polarization $P^{(3)}(t) = \epsilon_0 \chi^{(3)} E^3(t)$ to be:

$$P^{(3)}(t) = \frac{1}{4} \epsilon_0 \chi^{(3)} E_0^3 \cos 3\omega t + \frac{3}{4} \epsilon_0 \chi^{(3)} E_0^3 \cos \omega t. \quad (\text{II.3})$$

The first term produces a polarization that oscillates at three times the incident frequency and thus gives rise to third-harmonic generation. The second term is the nonlinear contribution to the polarization at the incident frequency and therefore acts to change the refractive index of the material at the applied optical

field. A consequence of the second term is the well-known phenomenon of self-focusing or defocusing which is one of the main focuses of this dissertation.

The intensity dependence of the refractive index n and the absorption coefficient α , which are related to the real and imaginary parts of $\chi^{(1)}$, becomes apparent in the presence of a strong optical field. They change according to the following formula: $n(I) = n_0 + \gamma I$ and $\alpha(I) = \alpha_0 + \beta I$, where n_0 and α_0 are the linear refractive index and linear absorption coefficients, respectively, and γ and β are the nonlinear refraction and nonlinear absorption coefficients, respectively. The nonlinear parameters γ and β are, in turn, related to the real and imaginary parts of $\chi^{(3)}$ by $\chi_R^{(3)} = 2n_0^2 \epsilon_0 c \gamma$, and $\chi_I^{(3)} = n_0^2 \epsilon_0 c^2 \beta / \omega$ where c is the speed of light, ω is the frequency, and ϵ_0 is the permittivity, all in free space. It is apparent that a parallel beam traversing a medium will focus if $\gamma > 0$ and will defocus if $\gamma < 0$. The first case is known as self-focusing and the second case as self-defocusing. It will also experience a reduction in transmitted power if $\beta > 0$ and an increase if $\beta < 0$ when compared to its linear transmission. There are many physical mechanisms that give rise to this phenomenon, but they depend on what time scale is being investigated.

The best method of experimentally determining the nonlinear parameters γ and β is by directly measuring the changes in n and α . The Z-scan and related Intensity-scan techniques are highly sensitive methods of obtaining nonlinear parameters. Both techniques will be presented in the next section along with their theory. Another important issue is that the initial spatial beam profile greatly influences self-focusing and defocusing. We also present the effects of beam ellipticity on these experiments.

(a) Z-scan

(i) Introduction

The Z-scan method^{1,2} has become a standard tool in determining nonlinear parameters of various materials. It is a single-beam technique that is based on the phenomenon of self-focusing and defocusing and has been described in detail in Ref. [1,2]. Briefly, the Z-scan setup consists of a sample, a collimated beam which is focused by a lens, and a far-field aperture set to collect a fraction of the incident light, as shown in Fig. II.1. The sample is translated through the focus in the direction of beam propagation (z -direction), and the far-field aperture transmission ($D2/D1$) after normalization (dividing by the first data point) is monitored keeping the input beam energy constant. When the sample is far from the focus, the intensity is low and does not induce nonlinear refraction in the sample. Consequently, the beam passes through the sample linearly and the normalized transmission in this region is one. As the sample is brought closer to the focus, the intensity increases, and the sample behaves as a lens with an intensity-dependent focal length. For example, if the sample acts as a converging lens (positive nonlinearity), then as it is brought near the focus of the beam the sample will focus the light closer to the lens, and the normalized transmission will decrease. This is schematically shown in Fig. II.2. When the sample is at the focus of the beam, the nonlinearity induced is a maximum, but the normalized transmission is one. This is due to the fact that the beam is being focused through the center of a converging lens. When the sample has passed through the focus, the same nonlinearity will cause the beam to collimate, and the normalized transmission will increase. Finally, when the sample is far from focus, the nor-

malized transmission will reach one again. An opposite behavior occurs for samples with negative nonlinearity.

A dispersion shaped curve, as shown in Fig. II.3, is obtained in the presence of nonlinear refraction from which the sign as well as the magnitude of the nonlinear refraction coefficient can be quickly estimated. Experimentally, we need only to know the difference in the peak and valley transmission $\Delta T_{p-v} = T_p - T_v$ since it has been shown¹ that this difference is directly proportional to the nonlinear refraction coefficient. This type of scan which allows a small fraction of the light through is known as a closed aperture Z-scan.

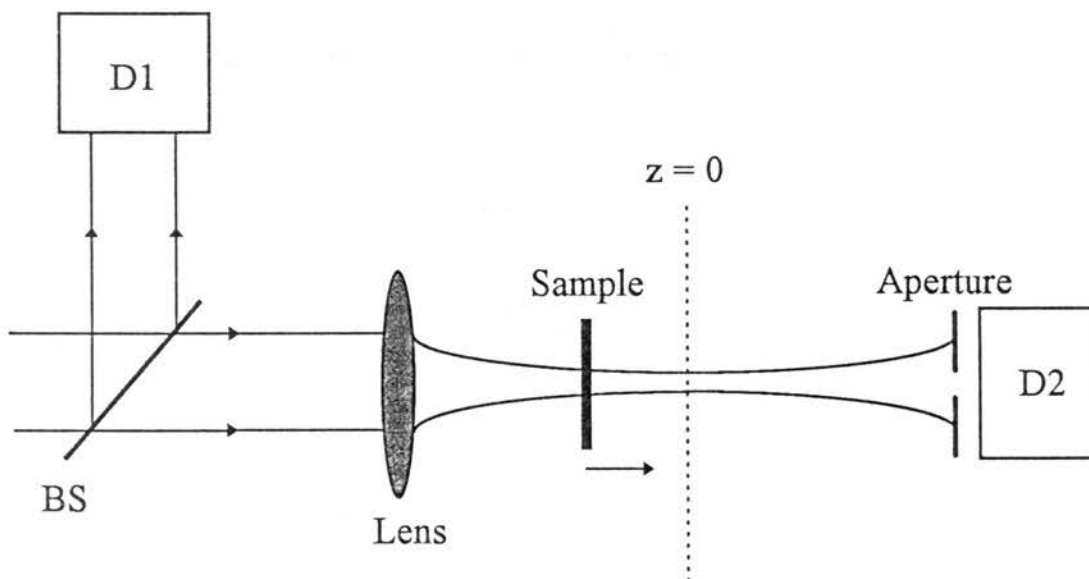


Figure II.1 Setup for Z-scan experiment. D1 and D2 are energy detectors. The sample is translated from negative z to positive z (direction of arrow) while the ratio $D2/D1$ is monitored.

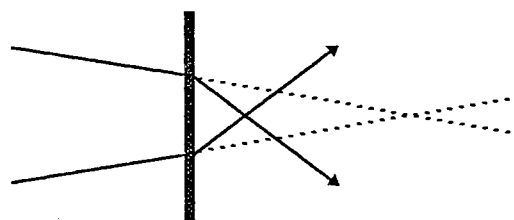
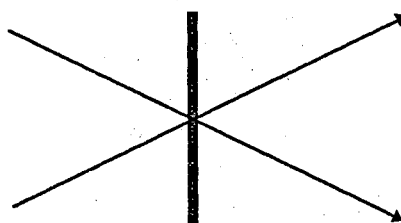
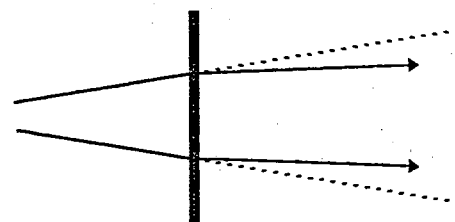
(a) $z < 0$ (b) $z = 0$ (a) $z > 0$

Figure II.2 A positive nonlinearity is used to demonstrate the Z-scan technique. Solid lines are the actual beam paths and dashed lines are the beam paths without any nonlinearity. (a) The sample is positioned before the focus. The beam focuses closer to the lens. (b) The sample is at the focus of the incoming beam which passes through undeviated. (c) The sample is now after the focus and the beam tends to collimate.

It should be pointed out that the rise and fall in a Z-scan is solely an aperture effect. If the aperture is removed and all the light is collected, then the Z-scan will only be sensitive to nonlinear absorption and is called an open aperture Z-scan. Again, experimentally, we need only to know the valley or peak transmission T_0 in an open aperture Z-scan since T_0 is directly proportional to the nonlinear absorption coefficient. The Z-scan technique has been used to study semiconductors,²⁻⁵ glasses,^{6,7} semiconductor doped glasses,⁸ liquid crystals,⁹ nonlinear liquids such as tea,¹⁰ and even biological materials.¹¹

New extensions have recently been added to this method in order to enhance its sensitivity and applicability. It is possible to unambiguously deduce the effects of nonlinear absorption and refraction simply by taking scans with an open and closed aperture.² The effects of bound-electronic and free-carrier refraction in the presence of two photon absorption has also been derived.³ A two color Z-scan was introduced to study nondegenerate optical nonlinearities^{4,12} and can also be used to do time-resolved measurements.⁶ In fact, using such a pump-probe technique it is possible to isolate the effects that are of thermal origin.¹³ A much more sensitive technique than the standard Z-scan known as the EZ-scan has been developed. It utilizes the fact that the wings of a circular Gaussian beam are more sensitive to far-field beam distortion.^{14,15} Recently, a RZ-scan was introduced to study optical nonlinearities of surfaces via reflection.¹⁶ Also, the effects of multiple reflections on the Z-scan and EZ-scan signatures have been presented.¹⁷

The standard Z-scan is analyzed using a wave optics approach and assuming a thin sample, i.e., the sample thickness is smaller than the Rayleigh range. The technique has been extended to thick samples by using ray matrices and employing the constant shape approximation¹⁸ (aberrationless). A more rigorous

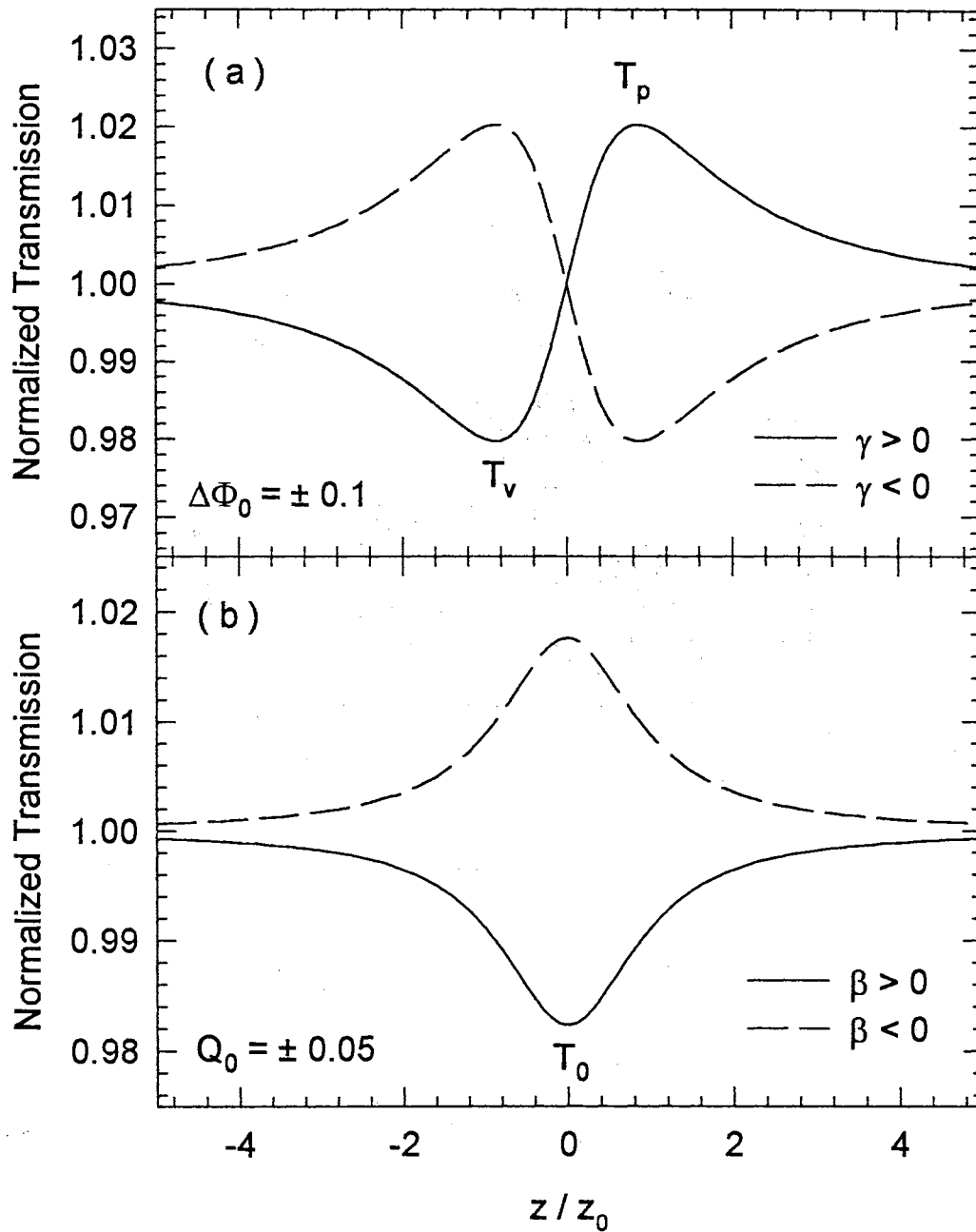


Figure II.3 Typical Z-scan signature for a (a) closed and (b) open aperture. In (a), a small on-axis phase-shift of $\Delta\Phi_0 = \pm 0.1$ was used with no nonlinear absorption, and in (b) a dimensionless irradiance $Q_0 = \pm 0.05$ was used. Here, γ is the nonlinear refraction and β is the nonlinear absorption coefficient, respectively. The sample position z is normalized to the Rayleigh range z_0 .

method that does not involve the use of this aberrationless theory has been carried out that holds for both thick and thin samples and in the limit of a thin sample gives the same on-axis peak-valley transmission difference as the wave optics approach. Since the method accounts for aberration, it is also possible to analyze a Z-scan in the near field.¹⁹ Recently, excellent agreement between theory and experiment was obtained using both this analytical theory, which is correct to the first order of irradiance, and a numerical calculation method based on Gaussian-Laguerre decomposition which is correct to all orders of irradiance.²⁰

The above analyses require that the beam be a circular Gaussian. Since there are laser sources such as some dye lasers that produce beams that are irregularly shaped, the Z-scan method needs to be extended to incorporate such beams. As such, a top-hat Z-scan analysis has been presented that uses a thin sample wave optics approach and includes both linear and nonlinear absorption.^{9,21} However, there is a class of beams that has not been previously analyzed which possesses a degree of symmetry but is not circular. They are elliptic Gaussian in spatial profile. There are some dye lasers and OPOs that produce these elliptic type beams.

We have recently encountered such a beam from our dye laser while investigating the nonlinear properties of some lead glasses. Due to the mixed thick and thin nature of our samples in the geometry used, we developed a model in the constant-shape approximation using ray matrices suitable for thick samples that includes *both* nonlinear refraction and absorption. We found good agreement between theory and experiment.²² However, in this thick sample regime the effects of beam ellipticity on the Z-scan signature were studied numerically. In order to better understand the role of beam ellipticity we also developed a wave optics model in the thin sample regime (where experiments are usually done)

from which we were able to derive analytical expressions for the transmission.²³ This wave-optics theory will form part of the Intensity-scan section due to the similarity of the two techniques. The Z-scan results predicted by the wave-optics theory and its discussion are relegated to Appendix A.

In the following section, we present the thick sample Z-scan theory for elliptic beams. The model was successfully applied to our nanosecond Z-scan work. Also, an extension of this model is presented in Appendix B where we studied the propagation of elliptic beams in a Kerr medium. It is important to emphasize that a circular beam is just a special case of an elliptic beam and the *thick* and *thin* Z-scan theory that we developed is a general theory.

(ii) Theory

When an intense laser beam is incident on a material, its refractive index as well as its absorption coefficient become, in general, functions of intensity. Assuming a cubic nonlinearity, they are given by the following equations,

$$n = n(I) = n_0 + \gamma I , \quad (\text{II.4a})$$

$$\text{and } \alpha = \alpha(I) = \alpha_0 + \beta I , \quad (\text{II.4b})$$

where n_0 is the linear refractive index, α_0 is the linear absorption coefficient, γ and β are the nonlinear refraction and absorption coefficients respectively, and I is the intensity. The contributions to γ come from phenomena such as the optical Kerr effect, electrostriction and thermal effects while β comes from mechanisms such as two-photon absorption. We consider an intensity distribution $I(x,y,t)$ that is elliptic Gaussian in spatial profile and is given in the TEM₀₀ mode by,

$$I(x, y, t) = \frac{2P(t)}{\pi w_x w_y} \exp \left\{ -\frac{2x^2}{w_x^2} - \frac{2y^2}{w_y^2} \right\} , \quad (\text{II.5})$$

where w_x and w_y are the radii, x and y are the transverse coordinates all along the semi-minor and semi-major axes respectively, and $P(t)$ is the instantaneous power. The z -dependence of the intensity is implicitly contained in the radii. The form of Eq. II.5 suggests that we can break the beam up into two one-dimensional Gaussian “beams”. Indeed, an elliptic Gaussian beam can be represented by two complex beam parameters (q -parameters) that contain all the information needed to specify its characteristics. They are defined along the semi-major and semi-minor axes of the beam. Their form can be derived by solving the paraxial wave equation and are found to be,

$$\frac{1}{q_{x,y}(z)} = \frac{1}{R_{x,y}(z)} - i \frac{\lambda}{\pi n_0 w_{x,y}^2(z)} , \quad (\text{II.6})$$

where $q_{x,y}$ are the q -parameters, $R_{x,y}$ are the radii of curvature of the two one-dimensional Gaussian beams, and λ is the wavelength in vacuum.²⁶ The formulation of the q -parameters allows the use of ray matrices to propagate the beams through the system which consists of a focusing lens, sample and far-field aperture. It is this type of geometric optics model we employ.

We model the self-action in our sample by considering it to be a quadratic index medium. In the aberration-free approximation, a Gaussian type beam is assumed to preserve its shape as it propagates through a nonlinear medium. This in turn requires that the refractive index vary quadratically in the transverse coordinates, r for circular and x and y for elliptic type beams. We expand the exponential in the intensity and keep only the quadratic terms in which case the refractive index becomes,

$$n(x, y, t) = n_1(t) - \frac{1}{2} n_{2x}(t) x^2 - \frac{1}{2} n_{2y}(t) y^2 , \quad (\text{II.7a})$$

$$\text{where,} \quad n_1(t) = n_0 + 2P(t)\gamma/\pi w_x w_y , \quad (\text{II.7b})$$

$$n_{2x}(t) = 8P(t)\gamma/\pi w_x^3 w_y, \quad (\text{II.7c})$$

$$\text{and,} \quad n_{2y}(t) = 8P(t)\gamma/\pi w_x w_y^3. \quad (\text{II.7d})$$

For simplicity of discussion, we consider here a temporally square pulse of width τ and incident power P_0 . A temporal Gaussian pulse can be easily incorporated by performing a separate time integral during the propagation. The ABCD optical transfer matrices that change the q -parameters within the sample can now be derived from the above expression.

It has been shown that a correction factor, a , should be included in the parabolic expansion of the refractive index induced by a circular Gaussian beam if one is to achieve a better agreement between theory and experiment.¹⁸ For our elliptic Gaussian beam two such factors a_x and a_y would be required. The range of values that a_x and a_y have can only be found after comparing this model with the corresponding wave-optics theory of elliptic beams and also numerical calculations of self-focusing of such beams which at the present, to our knowledge, is unavailable. Inclusion of the correction factors will enhance the accuracy of the nonlinear parameters found by this method but will not alter the qualitative predictions of the theory. Since our initial study was to investigate the relative thermo-optic properties of several lead silicate glasses, these correction factors were not considered.

The propagation of the elliptic beam through the media can be followed by studying the transformation of the q -parameters. The q -parameters are propagated separately through the system. The scheme used is that of a "distributed lens model". The sample is theoretically sliced many times, and each section is represented by two matrices, one to change q_x and the other to change q_y . By knowing the q -parameter at the beginning of each section, we can calculate the

radii and hence know the input intensity. The beams are then propagated to the end of the section using these matrices, and new radii and intensities are calculated prior to the propagation through the next one. In each section, the beam radii change very little, and we take the area of the elliptic beam to be constant. The power can then be attenuated by Eq. II.4b, thus including nonlinear absorption. This process is continued throughout all the sections of the sample.

In general, if we know the input q -parameter $q_{x,y}(0)$ at some position in a quadratic index media, then we can find the q -parameter $q_{x,y}(z)$ at any position z within the media as:

$$q_{x,y}(z) = \frac{q_{x,y}(0) \cos \varphi_{x,y} z + (1/\varphi_{x,y}) \sin \varphi_{x,y} z}{-\varphi_{x,y} q_{x,y}(0) \sin \varphi_{x,y} z + \cos \varphi_{x,y} z}, \quad (\text{II.8})$$

where $\varphi_{x,y}^2 = n_{2x,2y} / n_1$. Since the second term in Eq. II.7b is much smaller than n_0 , we let $n_1 \cong n_0$. The positions 0 and z should more accurately be replaced by z and $z + \Delta z$, i.e., these expressions hold for incremental distances. In a linear medium ($\varphi_{x,y} = 0$), the q -parameters can be propagated separately. However, in a nonlinear medium $\varphi_{x,y}$ is continuously changing, and it is the term that couples the q -parameters for the x and y beams during the propagation.

At the back face of the sample, the beams are propagated to the aperture, where the final radii w_{fx} and w_{fy} are calculated. The aperture, being circular, requires a simple numerical integration of the following expression,

$$P_{trans} = P_{exit} \int_0^{2\pi} \frac{uv [1 - \exp\{a^2 U^2 / 2\}]}{\pi V^2} d\theta, \quad (\text{II.9a})$$

$$\text{where, } U^2 = -u^2 - v^2 - u^2 \cos 2\theta + v^2 \cos 2\theta \quad (\text{II.9b})$$

$$\text{and, } V^2 = u^2 + v^2 + u^2 \cos 2\theta - v^2 \cos 2\theta \quad (\text{II.9c})$$

to calculate the transmitted power. Here, $u = \sqrt{2}/w_{fx}$, $v = \sqrt{2}/w_{fy}$, P_{exit} is the power at the exit plane of the sample, and a is the aperture radius. This reduces to the well known value of $P_{exit} \left\{ 1 - \exp(-2a^2/w^2) \right\}$ in the case of cylindrical symmetry of the beam. The above model allows for the beam radii to change in the sample due to self-action when the Rayleigh ranges are smaller than or comparable to the sample thickness. The effects of such a *thick* sample have been analyzed for similar experiments using a geometric optics model without nonlinear absorption for circular Gaussian beams.¹⁸ The model presented here reduces to a circular Gaussian *thin* lens approach⁷ where nonlinear absorption was included, and can be easily extended to a time-dependent domain.⁶

(iii) Theoretical Results

We present a brief numerical study of elliptical Gaussian beam Z-scans for thick samples. As shown in Appendix A, the waist separation and initial beam ellipticity greatly effects the Z-scan signature. If the beam is tightly focused so that the waist separation is small, then the Z-scan signature will be similar to that of a circular Gaussian beam. In Figs. II.4a and II.4b, the Z-scan plot of a beam with ellipticity e , defined as the ratio of the semi-major to semi-minor axes, of two is shown. In both figures, the sample thickness is 1 mm, and the beam having $w_y = 1$ mm and $w_x = 0.5$ mm is focused by a 5 cm lens. The aperture was set to collect 88% in the far-field. This means that most of the light from the x dimension is not blocked by the aperture. In Fig. II.4a, the nonlinear absorption coefficient β is changed while keeping the nonlinear refraction coefficient γ constant. In Fig. II.4b β is set to zero, and γ is varied. The model correctly predicts the behavior of the Z-scan signature as these parameters are varied. As β is increased (Fig.

II.4a), the effect is to suppress the peak, and the signature resembles that of an open aperture Z-scan. Other interesting features of the elliptic beam Z-scan such as the appearance of an additional peak and valley is discussed in Appendix A.

Some theoretical plots of Z-scan and optical limiting are shown in Figs. II.5a and II.5b to demonstrate the role of beam ellipticity assuming only a refractive nonlinearity. In an optical limiting experiment, the sample position is fixed, and the transmission is monitored as a function of input intensity. The solid line is that of a circular Gaussian beam of radius of 1 mm, and the dotted and dashed lines are for elliptic beams with ellipticity of two and four, respectively. The beams have the same prefocusing area and also the same on-axis on-focus intensity of 1 GW/cm^2 , producing an on-axis on-focus average index change of $\langle \Delta n_0 \rangle \cong 1.3 \times 10^{-6}$. The sample thickness is 1 mm, and the beam is focused by a 20 cm focal length lens. The aperture has a radius of 0.589 mm which amounts to 50% transmission for the circular beam. Upon careful examination of Fig. II.5a, the peak and valley of the Z-scan is found to be asymmetric about the transmission equals unity line. This is caused by the astigmatic nature of the focused beam. The optical limiting input is normalized to the critical power for catastrophic self-focusing for the circular beam. As the plots show, the characteristic signatures are the same, but the amount of nonlinearity manifested is different thus giving rise to the varied outputs.^{6,7} Thus, if an experiment is performed where the actual beam profile is elliptic but a circular one is used for the model, the theoretical fits will deviate from experimental data. The amount of deviation will of course depend on the asymmetry of the actual beam and on how tightly focused it is.

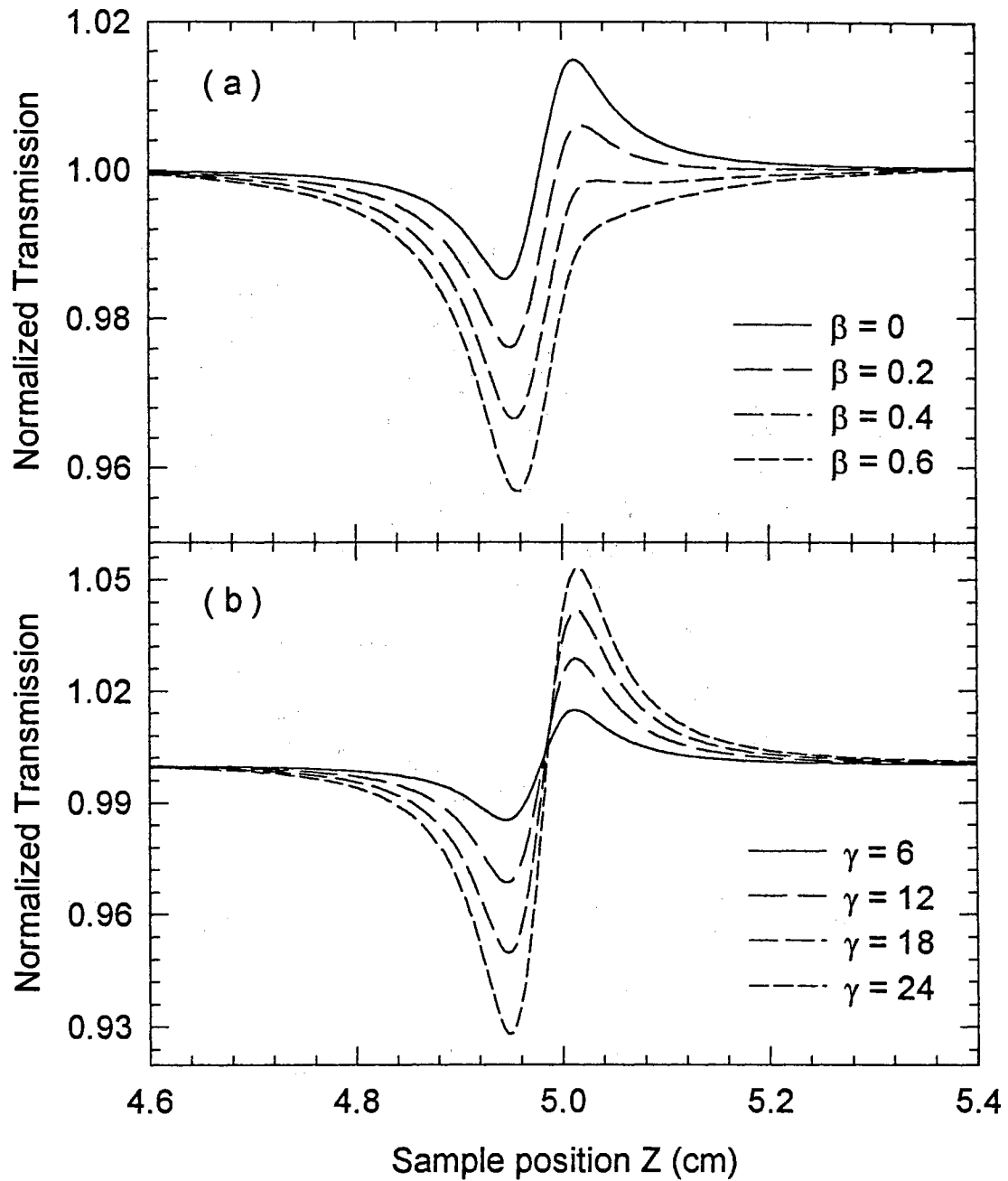


Figure II.4 Theoretical plots of Z-scan showing the effects of (a) the nonlinear absorption coefficient β (in cm/GW) with $\gamma = 6 \times 10^{-19} \text{ m}^2/\text{W}$, and (b) the nonlinear refraction coefficient γ (in $10^{-19} \text{ m}^2/\text{W}$) with $\beta = 0 \text{ cm/GW}$.

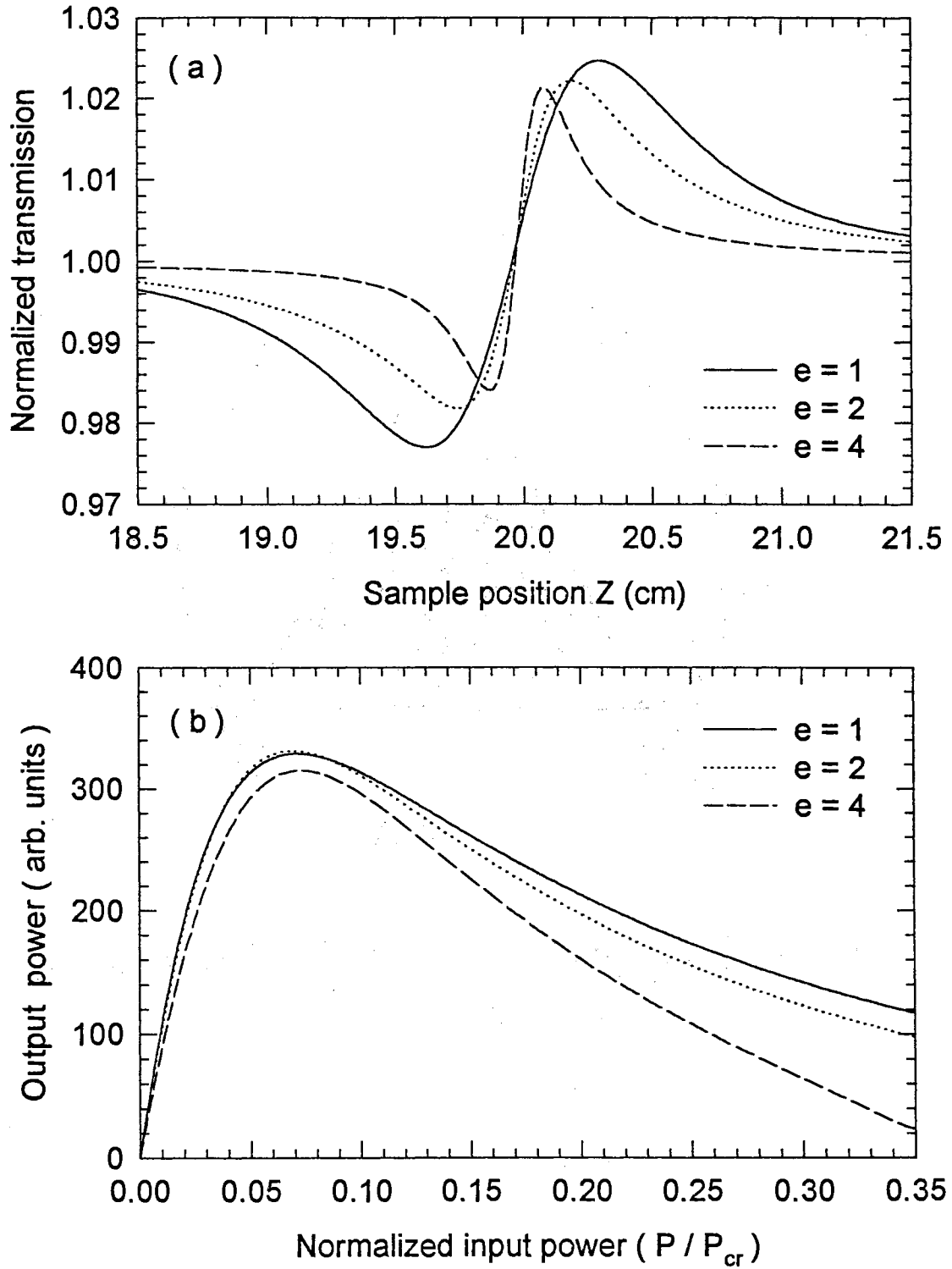


Figure II.5 Theoretical plots of (a) Z-scan and (b) optical limiting of beams with ellipticity $e = 1, 2,$ and 4 . The beams have the same prefocusing area and also the same on-axis on-focus intensity of 1 GW/cm^2 .

(b) Intensity-scan

(i) Introduction

The Intensity-scan method of determining optical nonlinearities of materials is complimentary to the conventional Z-scan technique. It is based on the phenomenon of self-focusing or defocusing, and both methods share the same theoretical formalism. Instead of translating the sample through the focus of the beam, as is done with the Z-scan technique, we place the sample at approximately a Rayleigh range distance from the focus. This is done in order to maximize the far-field effect. More precisely, the distance is $0.858z_0$ which corresponds to the peak or valley of a Z-scan. The intensity is gradually increased while the transmission is monitored. If there is an aperture in the far-field, then the transmission will either increase or decrease depending on the sign of the nonlinearity and also whether the sample is placed before or after the focus. In the absence of an aperture, the transmission will only be affected by nonlinear absorption. The Z-scan technique is also an Intensity-scan method, even though the beam energy is held constant, in that the sample encounters different intensities as it is translated.

Researchers have been conducting transmission measurements similar to the Z-scan and Intensity-scans for over 20 years.^{24,25} In fact, the traditional thermal lensing techniques²⁴ have been used to study the transmission both as a function of sample position and intensity. These transmission-type measurements were refined and enhanced into the Z-scan technique by Sheik-Bahae *et al.*¹ The Z-scan combined both high-sensitivity and simplicity, something previous techniques could not achieve. Also, an elegant theory was developed that allowed the

unambiguous interpretation of experimental results and easy extraction of relevant nonlinear material parameters from the data.

There are several practical difficulties that may be encountered in performing Z-scan measurements. It is essential to have very good pulse to pulse laser stability since the beam energy must be held constant. The linearity of the translation stage is also an important factor for a Z-scan because beam walk-off may occur. If the samples are wedged, then one must subtract a low intensity Z-scan from a high intensity one in order to cancel out the systematic transmission variation, i.e., take two Z-scans for a sample. In addition, the samples might damage at the focus of the beam. Some of these difficulties were experienced by us and another research group at the Center for Laser Research at OSU, Stillwater. Taheri *et al.*²⁷ realized that an Intensity-scan method could be used instead of the Z-scan that would avoid all the above mentioned problems but would reveal the same information as the Z-scan technique. More importantly, the Z-scan theoretical formalism could be applied yielding a simple extraction of nonlinear material parameters.

In what follows, we present a wave-optics theory for the Intensity-scan using an elliptical Gaussian beam. It was initially developed to study the effects of beam ellipticity on the Z-scan signature but is equally applicable to Intensity-scans. The circular limit of this theory was used to fit our Intensity-scan data.

1. Theory

The electric field of an elliptic Gaussian beam can be derived by solving the paraxial wave equation and is outlined in Ref. [26]. The form of the electric field is such that for the sake of theoretical analysis the beam can be broken up into two

separate one-dimensional beams, the *x-beam* and the *y-beam*. In the TEM₀₀ mode an elliptic beam has the following form:

$$E(x, y, z, t) = E_0(t) \sqrt{\frac{w_{0x}}{w_x(z)} \frac{w_{0y}}{w_y(z)}} \exp\{-i[kz - \eta(z)]\} \\ \times \exp\left\{-x^2 \left[\frac{1}{w_x^2(z)} + \frac{ik}{2R_x(z)} \right] - y^2 \left[\frac{1}{w_y^2(z)} + \frac{ik}{2R_y(z)} \right]\right\}, \quad (\text{II.10})$$

$$\text{where} \quad w_{x,y}^2(z) = w_{0x,0y}^2 \left\{ 1 + \frac{(z - z_{x,y})^2}{z_{0x,0y}^2} \right\}, \quad (\text{II.11})$$

$$R_{x,y}(z) = (z - z_{x,y}) \left\{ 1 + \frac{z_{0x,0y}^2}{(z - z_{x,y})^2} \right\}, \quad (\text{II.12})$$

$$\text{and} \quad \eta(z) = \frac{1}{2} \tan^{-1} \left(\frac{z - z_x}{z_{0x}} \right) + \frac{1}{2} \tan^{-1} \left(\frac{z - z_y}{z_{0y}} \right). \quad (\text{II.13})$$

Here, $w_{x,y}(z)$ and $R_{x,y}(z)$ are the beam radius and radius of curvature for the *x-beam* and *y-beam*, respectively, and $\eta(z)$ is the phase of the elliptic beam. The minimum beam waists are denoted by $w_{0x,0y}$ and are located at $z_{x,y}$. The Rayleigh ranges are given by $z_{0x,0y} = kw_{0x,0y}^2/2$, where $k = 2\pi/\lambda$ is the wavevector, and λ is the wavelength in free space. The temporal behavior of the electric field is contained in the term $E_0(t)$. The beam is traveling in the direction of increasing z and we take z to be zero at the focusing lens.

When an intense electric field of this nature is incident on a material, the resulting nonlinear paraxial wave equation can be solved analytically for a thin sample, i.e., the sample length is much smaller than that of the Rayleigh ranges. In this thin lens approximation the beam widths do not change as the beam traverses the sample, and the electric field only encounters a nonlinear phase shift

which leads to external self-focusing or defocusing. In the slowly varying envelope approximation (SVEA), Maxwell's equations can be written as

$$\frac{d\Delta\phi}{dz'} = \Delta n(I)k, \quad (\text{II.14})$$

$$\text{and} \quad \frac{dI}{dz'} = -\alpha(I)I \quad (\text{II.15})$$

where $\Delta n(I)$ is the change in the refractive index, $\alpha(I)$ is the absorption coefficient, z' is the penetration depth in the sample, $\Delta\phi$ is the phase shift, and I is the intensity of the elliptic beam incident on the material (front face, ignoring Fresnel reflection losses). The change in refractive index may be brought about by effects of various orders, but we will concentrate on a cubic nonlinearity $\Delta n(I) = \gamma I$ where γ is the nonlinear refraction coefficient. The absorption coefficient will, in general, contain both linear and nonlinear terms $\alpha(I) = \alpha + \beta I$, where α is the linear absorption coefficient, and β is the two-photon absorption coefficient, respectively. If we do not consider any nonlinear absorption, then Eq. II.14 and Eq. II.15 can be solved to give the on-axis phase shift at the exit plane $\Delta\phi_e(z, t)$ as

$$\Delta\phi_e(z, t) = \Delta\phi_0(z, t) \exp\left\{-\frac{2x^2}{w_x^2(z)} - \frac{2y^2}{w_y^2(z)}\right\}, \quad (\text{II.16})$$

$$\text{where} \quad \Delta\phi_0(z, t) = \frac{\Delta\Phi_0(t)}{\sqrt{\left(1 + (z - z_x)^2/z_{0x}^2\right)\left(1 + (z - z_y)^2/z_{0y}^2\right)}}, \quad (\text{II.17})$$

$$\text{and} \quad \Delta\Phi_0(t) = \gamma k L_{eff} 2P(t) / \pi w_{0x} w_{0y}. \quad (\text{II.18})$$

Here, $L_{eff} = (1 - e^{-\alpha L})/\alpha$, and $P(t)$ is the input beam power. It is important to note that $\Delta\Phi_0(t)$ should not be considered the "on-focus" phase shift literally

since the two “beams” focus at different z positions. We will, however, use this as a working definition since it will allow us later to derive a geometry-independent normalized Z-scan/Intensity-scan transmission. Another way of writing the phase shift at the exit plane is $\Delta\phi_e(z, t) = \gamma k I L_{eff}$ where I is

$$I(x, y, z, t) = \frac{2P(t)}{\pi w_x(z)w_y(z)} \exp\left\{-\frac{2x^2}{w_x^2(z)} - \frac{2y^2}{w_y^2(z)}\right\}. \quad (\text{II.19})$$

The electric field at the exit face E_e of the sample can be found in a manner similar to that of a circular Gaussian beam as

$$\begin{aligned} E_e(x, y, z, t) &= E(x, y, z, t) e^{-\alpha L/2} e^{i\Delta\phi_e(x, y, z, t)} \\ &= E(0, 0, z, t) e^{-\alpha L/2} \sum_{m=0}^{\infty} \frac{[i\Delta\phi_0(z, t)]^m}{m!} \exp\left\{-\frac{ikx^2}{2q_{m0x}(z)} - \frac{iky^2}{2q_{m0y}(z)}\right\}, \end{aligned} \quad (\text{II.20})$$

where q_{m0x} and q_{m0y} are the q -parameters defined by,

$$\frac{1}{q_{m0x, m0y}(z)} = \frac{1}{R_{x, y}(z)} - \frac{i\lambda}{\pi w_{m0x, m0y}^2(z)}, \quad (\text{II.21})$$

$$\text{and} \quad w_{m0x, m0y}^2(z) = w_{x, y}^2(z)/(2m + 1). \quad (\text{II.22})$$

This method of writing the electric field at the exit face in terms of an infinite sum of Gaussian beams, with each beam having the same initial radius of curvature, is known as Gaussian decomposition. The Gaussian decomposition method, as applicable to circular beams, is generalized to elliptic beams and is used to propagate each of the decomposed x - and y -beams to an aperture plane a distance d away. In terms of a few definitions that naturally arise from the propagation,

$$g_{x, y}(z) = 1 + d/R_{x, y}(z), \quad (\text{II.23})$$

$$R_{mx,my}(z) = d \left\{ 1 - \frac{g_{x,y}(z)}{g_{x,y}^2(z) + d^2/d_{m0x,m0y}^2(z)} \right\}^{-1}, \quad (\text{II.24})$$

$$w_{mx,my}^2(z) = w_{m0x,m0y}^2(z) \left\{ g_{x,y}^2(z) + \frac{d^2}{d_{m0x,m0y}^2(z)} \right\}, \quad (\text{II.25})$$

$$\text{and} \quad d_{m0x,m0y}(z) = kw_{m0x,m0y}^2(z)/2 \quad (\text{II.26})$$

and by considering the following relation

$$\sqrt{\frac{w_{m0x}(z) w_{m0y}(z)}{w_{mx}(z) w_{my}(z)}} e^{i\eta_m(z)} = \left(g_x(z) + \frac{id}{d_{m0x}(z)} \right)^{-\frac{1}{2}} \left(g_y(z) + \frac{id}{d_{m0y}(z)} \right)^{-\frac{1}{2}}, \quad (\text{II.27})$$

the electric field at the aperture plane E_a can be written as

$$E_a(x, y, z, t) = E(0,0, z, t) e^{-\alpha L/2} \sum_{m=0}^{\infty} \sqrt{\frac{w_{m0x}(z) w_{m0y}(z)}{w_{mx}(z) w_{my}(z)}} e^{i\eta_m(z)} \\ \times \exp \left\{ -\frac{ikx^2}{2q_{mx}(z)} - \fraciky^2}{2q_{my}(z)} \right\} \frac{[i\Delta\phi_0(z, t)]^m}{m!}. \quad (\text{II.28})$$

The q -parameters are defined to be

$$\frac{1}{q_{mx,my}(z)} = \frac{1}{R_{mx,my}(z)} - \frac{i\lambda}{\pi w_{mx,my}^2(z)}. \quad (\text{II.29})$$

When nonlinear absorption is included in Eq. II.15, the intensity at the exit face I_e is given by

$$I_e(x, y, z, t) = \frac{I(x, y, z, t) e^{-\alpha L}}{1 + \beta I(x, y, z, t) L_{eff}}, \quad (\text{II.30})$$

and the phase shift at the exit plane is

$$\Delta\phi_e(x, y, z, t) = \frac{k\gamma}{\beta} \ln[1 + \beta I(x, y, z, t) L_{eff}]. \quad (\text{II.31})$$

Note that when two-photon absorption is not present, Eq. II.31 reduces to Eq. II.16. Combining Eq. II.30 and Eq. II.31, the electric field at the exit plane can be written as

$$E_e(x, y, z, t) = E(x, y, z, t) e^{-\alpha L/2} [1 + \beta L_{eff} I(x, y, z, t)]^{\frac{ik\gamma - 1}{\beta - 2}}. \quad (\text{II.32})$$

The electric field at the aperture plane can be found in the same way and is identical to Eq. II.28 except that an additional term of the form

$$\prod_{n=0}^m \left[1 + (2n-1) \frac{i\beta}{k\gamma} \right] \quad (\text{II.33})$$

must be included in the sum over m . To find the normalized transmission, it is convenient to convert from Cartesian to polar coordinates since most apertures are circular. The normalized transmission is

$$T(z) = \frac{\frac{c\epsilon_0 n_0}{2} \int_{-\infty}^{\infty} \int_0^{r_a} \int_0^{2\pi} |E_a(r, \theta, z, t)|^2 r dr d\theta dt}{S \int_{-\infty}^{\infty} P(t) dt}, \quad (\text{II.34})$$

where, S is the transmission in the linear regime, r_a is the aperture radius, c is the speed of light in free space, ϵ_0 is the permittivity, and n_0 is the linear refractive index.

(*iii*) Closed aperture ($S \cong 0$)

We now calculate the on-axis transmission in the presence of a small “on-focus” nonlinearity assuming a steady state cw situation or, equivalently, a square pulse with instantaneous nonlinearity. That is, we take $|\Delta\Phi_0| \ll 1$, and impose a far-field condition $d \gg z_{0x}, z_{0y}$. By keeping only the first two terms

in the expansion in Eq. II.28, the transmission as given by Eq. II.34 can be written as

$$T(z) = \frac{|E_a(0,0,z,\Delta\Phi_0)|^2}{|E_a(0,0,z,\Delta\Phi_0=0)|^2} = \left| 1 + i\Delta\Phi_0 \left(g_x + \frac{id}{d_{00x}} \right)^{\frac{1}{2}} \left(g_y + \frac{id}{d_{00y}} \right)^{\frac{1}{2}} \left(g_x + \frac{id}{d_{10x}} \right)^{-\frac{1}{2}} \left(g_y + \frac{id}{d_{10y}} \right)^{-\frac{1}{2}} \right|^2, \quad (\text{II.35})$$

where the z dependence of $g_{x,y}$, $d_{00x,00y}$, and $d_{10x,10y}$ are to be understood.

We take $g_x \cong d/R_x$ and $g_y \cong d/R_y$ and rewrite Eq. II.35 as

$$T(z) = \left| 1 + i\Delta\Phi_0 \frac{\sqrt{a-ib}}{h} \right|^2, \quad (\text{II.36})$$

$$\text{where } h^2 = (d_{00x}^2 + 9R_x^2)(d_{00y}^2 + 9R_y^2), \quad (\text{II.37})$$

$$a = (d_{00x}^2 + 3R_x^2)(d_{00y}^2 + 3R_y^2) - 4R_x R_y d_{00x} d_{00y}, \quad (\text{II.38})$$

$$\text{and } b = 2\{R_x d_{00x}(d_{00x}^2 + 3R_x^2) + R_y d_{00y}(d_{00y}^2 + 3R_y^2)\}. \quad (\text{II.39})$$

By defining $A - iB = \sqrt{a-ib}$, the transmission becomes

$$T(z) = 1 + 2\Delta\Phi_0 B/h = 1 + 2\Delta\Phi_0 p \left\{ \frac{\sqrt{a^2 - b^2} - a}{2h^2} \right\}^{\frac{1}{2}}, \quad (\text{II.40})$$

where $p = \pm 1$ comes from the square root. We define the following terms:

$$x(z) = (z - z_x)/z_{0x}, \quad (\text{II.41})$$

$$\text{and } y(z) = (z - z_y)/z_{0y}, \quad (\text{II.42})$$

to derive a geometry-independent expression for the transmission. It simplifies to

$$T(z) = 1 + 2\Delta\Phi_0 p \left\{ \frac{\sqrt{(x^2 + 9)(x^2 + 1)(y^2 + 9)(y^2 + 1) - (x^2 + 3)(y^2 + 3) + 4xy}}{2(x^2 + 9)(x^2 + 1)(y^2 + 9)(y^2 + 1)} \right\}^{\frac{1}{2}} \quad (\text{II.43})$$

This is the Z-scan/Intensity-scan geometry-independent transmission expression for elliptic Gaussian beams. The theoretical results of the effects of beam ellipticity on the Z-scan signature will be presented in Appendix A.

The circular limit of the above expression was used in our Intensity-scan measurements. The case for circular symmetry can be checked by letting $x = y = u = (z - z_{min})/z_0$, i.e., u is an algebraic quantity that can be either positive or negative. Then the above expression reduces to

$$T(u) = 1 + \frac{4\Delta\Phi_0 u}{(u^2 + 9)(u^2 + 1)} \quad (\text{II.44})$$

which is the well-known circular Gaussian on-axis transmission. Experimentally, the far-field condition ($d \gg z_{0x}, z_{0y}$) is not always rigorously met, and, to incorporate the aperture distance d , we derive the following expression for the on-axis transmission for a circular Gaussian beam:

$$T(z) = 1 + \frac{4gd\Delta\Phi_0}{z_0(g^2 + d^2/d_1^2)(1 + z^2/z_0^2)^2} \quad (\text{II.45})$$

Here, $d_m = kw_m^2/2$, and w_m is defined by Eq. II.25. This is the transmission formula that was used to fit our data. For pulsed work, the on-axis phase shift $\Delta\Phi_0$ should be replaced by a time-averaged phase shift $\langle\Delta\Phi_0\rangle$. For a Gaussian laser pulse with instantaneous nonlinearity (e.g. electronic effect) $\langle\Delta\Phi_0\rangle = \Delta\Phi_0/\sqrt{2}$, and for a cumulative nonlinearity with a decay time much longer than the pulse duration (e.g. thermal effect) $\langle\Delta\Phi_0\rangle = \Delta\Phi_0/2$. Recall that $\Delta\Phi_0 = \gamma k L_{eff} I_0$

where I_0 is the peak intensity at the sample (front face). The front and back face reflections are canceled by the normalization procedure, but the nonlinear refraction is caused by an intensity within the sample. Thus, reflection losses can be included by replacing I_0 by $I_0(1-R)$ where R is the reflectivity.

(*ib*) Open aperture ($S = 1$)

The basic results needed to calculate the open aperture transmission are now presented. Since the final expression is very similar to that of a circular Gaussian beam and is straight forward to obtain, we will only highlight the derivation. Starting with Eq. II.30, we change to polar coordinates and write

$$q(r, \theta, z, t) \equiv \beta L_{eff} I(r, \theta, z, t) = q_0(z, t) \exp\{-2r^2 f(\theta, z)\}, \quad (\text{II.46})$$

$$\text{where} \quad q_0(z, t) = \beta L_{eff} 2P(t) / \pi w_x(z) w_y(z), \quad (\text{II.47})$$

$$\text{and} \quad f(\theta, z) = \frac{\cos^2 \theta}{w_x^2(z)} + \frac{\sin^2 \theta}{w_y^2(z)}. \quad (\text{II.48})$$

The power at the exit plane is then found to be

$$\begin{aligned} P_e(z, t) &= \int_0^\infty \int_0^{2\pi} \frac{q_0(z, t) \exp\{-2r^2 f(\theta, z)\} e^{-\alpha L} r dr d\theta}{\beta L_{eff} [1 + q_0(z, t) \exp\{-2r^2 f(\theta, z)\}]} \\ &= \frac{\pi w_x(z) w_y(z)}{2 \beta L_{eff}} \ln [1 + q_0(z, t)] e^{-\alpha L} \end{aligned} \quad (\text{II.49})$$

Since the numerator in Eq. II.34 is just the time-integral of the transmitted power, we can substitute Eq. II.49 in it to get the normalized transmission for any $q_0(z, t)$. For a Gaussian temporal pulse with peak power P_0 and for $|q_0(z, 0)| < 1$, the normalized transmission can be written as a simple series

$$T(z) = \sum_{k=0}^{\infty} \frac{[-q_0(z,0)]^k}{(k+1)^{3/2}} \quad (\text{II.50})$$

$$\text{where } q_0(z,0) = 2P_0 \beta L_{eff} / \pi w_x(z) w_y(z). \quad (\text{II.51})$$

Here, $P_0 = E/(\tau\sqrt{\pi})$, where E is the energy of the beam and τ is the e^{-1} pulse width. Only a few terms are required in the sum to fit the data. In order to consider front and back face reflection losses, we include a $(1-R)$ factor in the numerator of the definition of $q_0(z,0)$ for the open aperture transmission.

3. Theoretical Results

A brief discussion of the theoretical results for the Intensity-scan is presented, but only for a circular beam. The effects of beam ellipticity on Intensity-scans for both thick and thin samples will be considered for future studies. In Fig. II.6a, a closed aperture Intensity-scan is shown with a positive nonlinearity and sample placed before and after the focus. The opposite behavior is exhibited with a negative nonlinearity. The slope of the graph is directly related to the nonlinear refraction coefficient by Eq. II.18. Since most commercial graphics programs are capable of doing linear regressions, the slope can be easily found.

When there is nonlinear absorption present in the sample, the slope will either be enhanced or diminished depending on the sign of β and γ and the sample position. For example, with positive β , positive γ , and sample placed before the focus, the slope will be reduced (be more negative). If the aperture is removed and β is positive, the normalized transmission will drop with increasing intensity. This is schematically represented in Fig. II.6b.

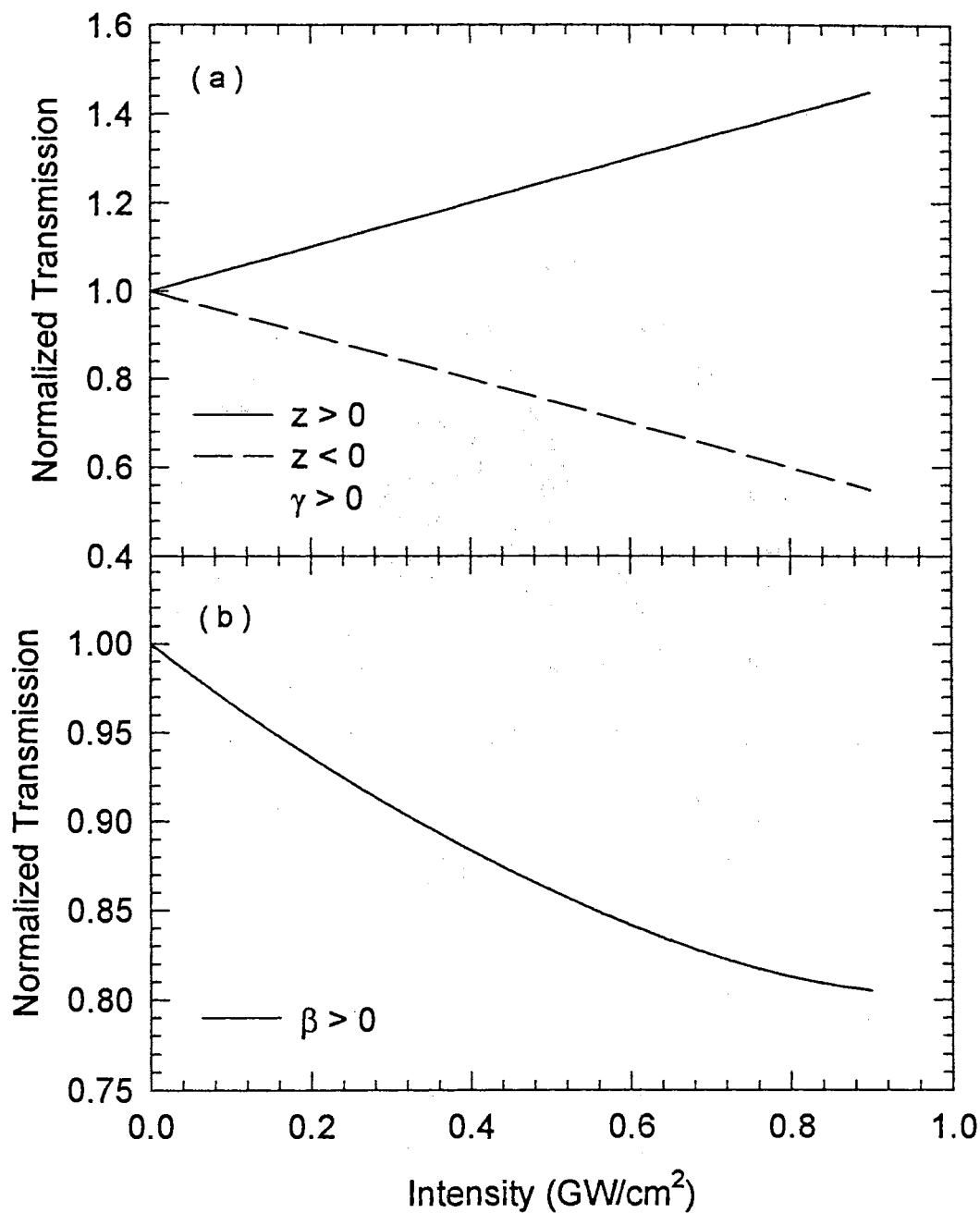


Figure. II.6 (a) Theoretical plot of closed aperture Intensity-scan with positive nonlinearity, and sample positions before and after the focus. A negative nonlinearity exhibits the opposite behavior. (b) Theoretical plot of open aperture Intensity-scan with positive nonlinear absorption.

2. Brillouin Scattering

Light scattering is a very important tool for studying the fundamental excitations of materials. The inelastic scattering of light from thermally excited acoustic phonons gives rise to the phenomenon known as Brillouin scattering. The origin of the Brillouin scattered light can be traced back to inhomogeneities in the dielectric constant that are caused by thermal fluctuations. The acoustic excitations responsible for Brillouin scattering are very weak ($\sim 1-5 \text{ cm}^{-1}$), and thus a high resolution instrument such as a Fabry-Perot interferometer must be used to detect the signal. In addition, the light source must also be a laser operating in a single longitudinal mode for the unambiguous interpretation of the signal. The Brillouin scattering theory presented in the next section is applicable to transparent isotropic materials and is, therefore, relevant to glasses.

Brillouin scattering theory can be approached from either a classical or a quantum mechanical point of view. In quantum mechanical terms, a photon of wavevector k_0 and frequency ω_0 is scattered into a wavevector k_s and frequency ω_s after interacting with a phonon of wavevector q and frequency ω_q . The conservation of momentum and energy require the following relation:

$$\omega_s = \omega_0 \pm \omega_q \quad (\text{II.52})$$

$$\text{and } k_s = k_0 \pm q. \quad (\text{II.53})$$

The plus sign physically means that a phonon was absorbed or annihilated in the scattering event causing the scattered photon to be of higher energy. This is called an Anti-Stokes event. The minus sign refers to the fact that a phonon was created during the interaction causing the scattered photon to have lower energy. Such a process is called a Stokes event. Both processes are known as first-order

scattering since there is only one interaction between the photon and phonon. They are schematically shown in Figure II.7.

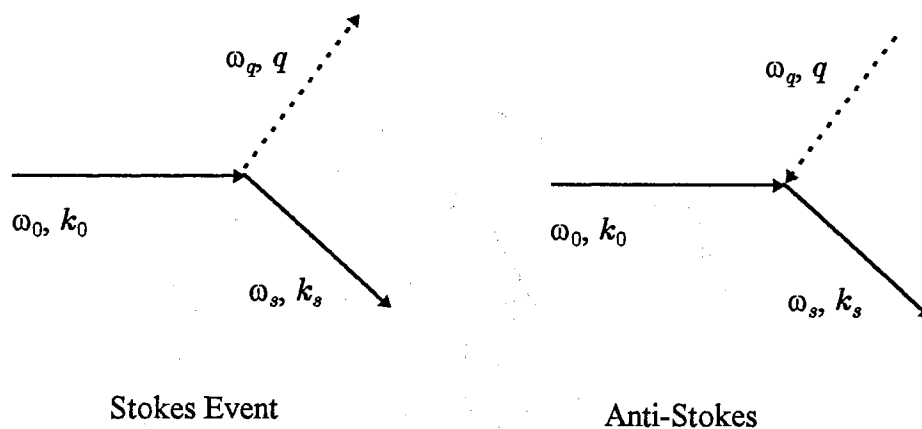


Figure II.7 Diagram for first-order photon-phonon scattering

For a crystal with a lattice parameter of a , the range of q that spans the first Brillouin zone is $0 \leq |q| \leq \pi/a$. Thus, $|q|$ ranges from zero to 10^8 cm^{-1} . Since first-order light scattering only involves phonon modes whose wavelength is comparable to that of light, it is easy to see that $|q| \leq 10^5 \text{ cm}^{-1}$. In other words, we can only study the phonon modes that lie very close to the Brillouin zone center. There are three acoustic modes. Along principal directions two are transverse or shear waves, and one is a longitudinal or a compressional wave. In a glassy system, two of the transverse modes are degenerate due to the isotropic nature of glass. The frequency of the three acoustic modes ω_B near the zone center in-

creases linearly with the wavevector and slopes are simply the sound velocity v_B of the modes, i.e., $\omega_B = v_B q$. Typically, $v_B \sim 10^5$ cm/s.

Since the velocity of light c is much greater than that of sound, it is a very good approximation to take $|k_s| = |k_0|$ and therefore

$$|q| = 2|k_s| \sin \theta/2 \quad (\text{II.54})$$

where θ is the scattering angle between k_0 and k_s . From the above equation, it is a simple matter to derive the Brillouin shift $\Delta\omega_B$ in cm^{-1} as

$$\Delta\omega_B = \frac{2nv_B \sin \theta/2}{c\lambda_0} \quad (\text{II.55})$$

where n is the refractive index and all the units are in cgs. The Brillouin shift is the frequency difference between the Brillouin scattered light and the incident laser. It thus corresponds to the frequency of the acoustic modes. These modes appear as Stokes and Anti-Stokes side peaks to the predominantly elastically scattered light or Rayleigh line in the observed spectrum.

The long wavelength nature of the acoustic phonons involves in-phase motion of many units cells, and we may treat the medium as an elastic continuum or Debye model. In that case, the above equation can also be derived by considering the sound wave as a moving grating and the incident light being Bragg reflected from it. Thus, the frequency of the scattered light experiences a Doppler shift from which the Brillouin shift can be found. The maximum shift will occur during back-scattering ($\theta = 180^\circ$) and minimum during forward-scattering ($\theta = 0^\circ$).

The polarization and frequency of each acoustic mode can be found for a particular q through the elastic constants C_{iklm} assuming a continuum model. In the harmonic approximation, the equation of motion is:

$$\rho \frac{\partial^2 u_i}{\partial t^2} = \sum_{klm} C_{iklm} \frac{\partial^2 u_m}{\partial \eta_k \partial \eta_l} \quad (\text{II.56})$$

Here, ρ is the density, \mathbf{u} is the displacement vector, and \mathbf{r} is the location of the equilibrium point that is being displaced.²⁸ Plane-wave solutions to this equation can be found for a given direction of \mathbf{q} of the form $u_i = u_{0i} \exp(\mathbf{q} \cdot \mathbf{r} - \omega t)$. Substituting this solution into Eq. II.56 results in the following matrix equation:

$$\sum_{kl} \left[C_{iklm} \hat{q}_k \hat{q}_l - \rho v^2 \delta_{im} \right] u_{0m} = 0 \quad (\text{II.57})$$

where \hat{q}_k is the k th component of the unit vector $\hat{\mathbf{q}}$. Nontrivial solutions of the above can be found by setting the determinant of the coefficient of u_{0m} to zero. There are three roots corresponding to the three acoustic modes each with its own velocity. In general, the three modes may be of mixed polarization. However, if \mathbf{q} is chosen to be in a high symmetry direction, then the displacement eigenvectors \mathbf{u} will be either perpendicular or parallel to \mathbf{q} . The perpendicular displacement is a transverse acoustic mode (TA phonon), and the parallel one is a longitudinal acoustic mode (LA phonon). That is, only in particular directions of \mathbf{q} do there exist two pure transverse modes and one pure longitudinal mode.

For example, if \mathbf{q} is propagating in an arbitrary $[1,0,0]$ direction of an isotropic system, then in six-component notation, Eq. II.57 yields two degenerate transverse phonons with eigenvectors $[0,1,0]$ and $[0,0,1]$, each phonon having the same velocity $v_{TA} = \sqrt{C_{44}/\rho}$. There is also a longitudinal phonon represented by an eigenvector $[1,0,0]$ and velocity $v_{LA} = \sqrt{C_{11}/\rho}$. Note that the displacement eigenvectors are perpendicular to \mathbf{q} for the TA phonons and parallel to \mathbf{q} for the LA phonon. The contracted notation used follows the convention that 11 \rightarrow 1; 22 \rightarrow 2; 33 \rightarrow 3; 23,32 \rightarrow 4; 13,31 \rightarrow 5; 12,21 \rightarrow 6. In a glass there are only two inde-

pendent elastic constants C_{11} and C_{44} and the third elastic constant is related to the first two through the Cauchy relation, $C_{12} = C_{11} - 2C_{44}$. Thus, experimentally we can calculate the phonon velocities from the measured Brillouin shifts and then determine the elastic constants.

We have seen that glasses have two pairs of Brillouin peaks on either side of the Rayleigh line. However, to determine which peak corresponds to a transverse phonon and which to a longitudinal phonon, we need to understand the polarization selection rules of the Brillouin scattered light. Therefore, we must study the effect of the sound waves on the optical properties of the material.

As a sound wave propagates, it produces a local strain in the material which in turn perturbs the local dielectric constant ϵ by an amount $\delta\epsilon$. When a plane monochromatic light wave traverses the material, there will be an additional polarization due to this perturbation $\delta P = E_0\delta\epsilon/4\pi$ that will scatter light at shifted frequencies corresponding to the acoustic modes. Here, E_0 is the amplitude of the incident light. For an incident light that is polarized in the j th direction and scattered light that is polarized in the i th direction, the Rayleigh ratio or differential scattering cross-section per unit volume R_{ij} is defined as

$$R_{ij} = r^2 I_s^i / V I_0^j \quad (\text{II.58})$$

where r^2 is the distance from the scattering volume to the detector, V is the scattering volume, and I_s and I_0 are the scattered and incident intensity, respectively. R_{ij} can be completely specified in terms of macroscopic parameters.²⁸ The local strain tensor x_{kl} and the change in reciprocal of the local dielectric constant $\Delta(\epsilon^{-1})_{ij}$ are physically related through the photoelastic effect by

$$\Delta(\epsilon^{-1})_{ij} = \sum_{kl} p_{ijkl} x_{kl} \quad (\text{II.59})$$

where p_{ijkl} are Pockel's coefficients. Eq. II.59 can be rewritten as

$$\delta\varepsilon_{ij} = -\sum_{kl} \varepsilon_{0ii} \varepsilon_{0jj} p_{ijkl} x_{kl} \quad (\text{II.60})$$

where $\varepsilon_{0ii} = \varepsilon_{0jj} = \varepsilon_0$ for a glass. If we assume that each acoustic excitation is on average at thermal equilibrium at temperature T , then the Rayleigh ratio of the j th mode with velocity v_j is found to be

$$R_j = \frac{\omega_s^4 k_B T}{32\pi^2 c^4 \rho v_j^2} [\hat{e}_s \cdot T_j \cdot \hat{e}_0]^2 (n_s/n_0) \quad (\text{II.61})$$

where T_j is the Brillouin tensor for the j th mode, ω_s is the scattered angular frequency, k_B is Boltzman's constant, and \hat{e}_s and \hat{e}_0 are the unit vectors showing the polarization directions of the scattered and incident electric fields.²⁸ Here, n_s and n_0 are the refractive indices of the scattered and incident light, respectively, and are equivalent in glasses. The Brillouin scattering tensors are listed below for the [1,0,0] or x phonon in contracted notation for an isotropic medium:

$$\begin{array}{ccc} \text{LA phonon [1,0,0]} & \text{TA phonon [0,1,0]} & \text{TA phonon [0,0,1]} \\ T = \varepsilon_0^2 \begin{pmatrix} p_{11} & 0 & 0 \\ 0 & p_{12} & 0 \\ 0 & 0 & p_{12} \end{pmatrix} ; & T = \varepsilon_0^2 \begin{pmatrix} 0 & p_{44} & 0 \\ p_{44} & 0 & 0 \\ 0 & 0 & 0 \end{pmatrix} ; & T = \varepsilon_0^2 \begin{pmatrix} 0 & 0 & p_{44} \\ 0 & 0 & 0 \\ p_{44} & 0 & 0 \end{pmatrix}. \end{array} \quad (\text{II.62})$$

There are only two independent Pockel's coefficient in glasses, p_{11} and p_{44} and the third $p_{12} = p_{11} - 2p_{44}$ is related to the first two by the Cauchy relation.

For a right-angle scattering geometry with q along [1,0,0] direction, k_0 along [-1,0,1] and k_s along [1,0,1] the Brillouin scattered intensities are

$$I_{VV} = \left(I_0 \varepsilon_0^4 / r^2 \right) (\omega_0 / c)^4 \left(V k_B T / 32\pi^2 \right) \left(p_{12}^2 / C_{11} \right) \quad (\text{II.63a})$$

$$I_{HH} = (I_0 \epsilon_0^4 / r^2) (\omega_0 / c)^4 (V k_B T / 32 \pi^2) (p_{44}^2 / C_{11}) \quad (\text{II.63b})$$

$$I_{VH} = I_{HV} = (I_0 \epsilon_0^4 / r^2) (\omega_0 / c)^4 (V k_B T / 32 \pi^2) (p_{44}^2 / 2C_{44}). \quad (\text{II.63c})$$

Here, ω_0 refers to the frequency of the incident light. The first and second subscripts in the scattered intensity refers to the polarization of the incident and scattered light, respectively. The VV and HH components are scattering from LA phonons and depend on normal strains that are parallel to the scattering plane. The VH and HV intensities originate exclusively from TA phonons and are caused by shearing strains acting perpendicular to the scattering plane. Thus, by selecting relative polarization for the incident and scattered light, we may select specific acoustic modes. Alternatively, we may perform measurements in a back-scattering geometry in which case there is no scattering from the TA phonons. This can be verified by calculating the Rayleigh ratio for such a geometry using the TA Brillouin tensors.

Finally, we give the formulae that were used to calculate the photoelastic constants from our experiments. The Brillouin intensities of our samples were measured relative to a fused quartz standard with known photoelastic constants.

$$p_{12} = p_{12}^0 (V^0 / V)^{\frac{1}{2}} (C_{11} / C_{11}^0)^{\frac{1}{2}} [(n + 1) / (n^0 + 1)]^2 (n^0 / n)^5 \xi^{\frac{1}{2}} \quad (\text{II.64})$$

$$p_{44} = p_{12} (v_{TA} / v_{LA}) (2I_{TA} / I_{LA})^{\frac{1}{2}} \quad (\text{II.65})$$

Here, the superscript 0 refers to the standard, ξ is the ratio of the integrated intensity of the sample to that of fused quartz for the LA phonon, and I_{TA} and I_{LA} refer to the integrated intensities of the appropriate modes.

CHAPTER III

EXPERIMENT

1. Z-scan and Optical Limiting

We performed Z-scan and Optical Limiting on several binary lead silicate glasses in order to study their nonlinear optical properties in the nanosecond regime. At the time of the experiments, it was believed that the thermal nonlinearity was the dominant mechanism in these high absorbing glasses on this time scale.^{6,7} To further our understanding of the mechanism behind the nonlinearity, we studied the glasses close to their UV absorption edge.

The lead glasses had the following compositions: $[\text{PbO}]_x [\text{SiO}_2]_{1-x}$, where $x = 32\%$, 42% , 52% and 62% all in mole percent. The samples were cut into parallelepipeds of two thicknesses, 1.0 mm and 1.5 mm and polished to optical quality using cerium oxide (CeO) as a water-based polishing agent. We found the CeO suspensions to be much better than the traditional diamond paste due to their simplicity of use and variable granularity. The samples were also brittle and much care was exercised in their handling. It is noteworthy that during the heating of the samples onto the polishing stubs and their subsequent removal, the polished side that was last in contact with the glue (or wax) on the stub had developed a thin film. The amount of film increased with lead concentration.

Table III.1 Sample designation and relevant parameters for lead silicate glasses

Sample	PbO (% mole)	SiO ₂ (% mole)	Thickness (mm)	n (460 nm)	α (cm ⁻¹) (460 nm)
L32	32	68	1.00, 1.50	1.726	0.758
L42	42	58	1.00, 1.50	1.847	0.783
L52	52	48	1.00, 1.56	1.947	0.902
L62	62	38	1.00, 1.50	2.117	2.47

Therefore, we used a soft adhesive tape to stick the side that had no film onto the stub and repolished the filmed side for about 30 to 60 seconds. This eliminated the films but reduced the optical quality of the surface somewhat. Further repolishing of the filmed side may have resulted in a sacrifice of parallelism and was thus avoided. Table III.1 has the nomenclature and other relevant parameters we will use to describe the glasses.

For the experiment, we used an injection-seeded Nd:YAG laser (Spectra Physics GCR-4) operating at 1064 nm. The beam was passed through a KDP crystal to get the third harmonic at 355 nm. This served as a pump beam for our dye laser (Spectra Physics PDL-3) which had Coumarine 460 as the active medium. Coumarine 460 is a low gain dye with a half-life of 3 hours at 10 Hz and tuning range of 446 nm to 478 nm centered around 460 nm. The low gain nature of the dye forced us to use a side-pumping scheme which had some interesting consequences. The beam that emerged from the dye laser had an elliptical Gaussian shape in its transverse spatial profile. The beam output was checked using a laser beam profiler (Spiricon LBA 100) which had software capable of curve fit-

ting Gaussian functions to each transverse dimension of the intensity profile. A correlation value of 0.85-0.90 was reported demonstrating that the beam was approximately 85%-90% elliptical Gaussian. The semi-major, w_y , and semi-minor, w_x , axes were measured to be 2.0 mm and 0.35 mm, respectively, for the collimated output beam. The pulse duration of the Nd:YAG laser was 10 ns (FWHM) and that of the dye laser was 7 ns.

The Z-scan/Optical Limiting setup is shown in Fig. III.1. Our setup is an example of a “tight-focusing” geometry that is commonly used to study optical limiting of materials. The beam was passed through a variable attenuator (Newport 935-10), that allowed us to control the input energy, followed by a vertical polarizer. A small portion (about 10%) of the beam was split off to monitor how much energy was incident on the samples. The beam was then focused by a 5 cm focal length lens. A far-field circular aperture of radius 1.64 mm was placed a distance of 10 cm from the lens. This gave a transmission of about 90% with no sample present. The minimum radii w_{0y} and w_{0x} could not be accurately measured but were calculated by a Gaussian beam-optics method²⁶ to be 3.7 μm and 21 μm , respectively, with a corresponding Rayleigh range of $z_{0y} = 0.20$ mm and $z_{0x} = 6.4$ mm. The sample thicknesses were 1.00 and 1.50 mm, indicating a mixed thick and thin sample, i.e., it is thin for the *x-beam* but thick for the *y-beam*. Since the *x* and *y* beams do not focus at the same *z* position, we choose $z = 0$ at the focusing lens. The calculated waist separation is $\Delta z_{xy} = z_y - z_x$ is 200 μm , where z_y and z_x are the positions where the *y* and *x* beam focus, respectively. The energy was detected by pyroelectric energy probes (Molelectron J4-09) connected to a dual energy meter (Molelectron JD2000). The sample was placed on an adjustable sample holder which in turn was placed on a micrometer

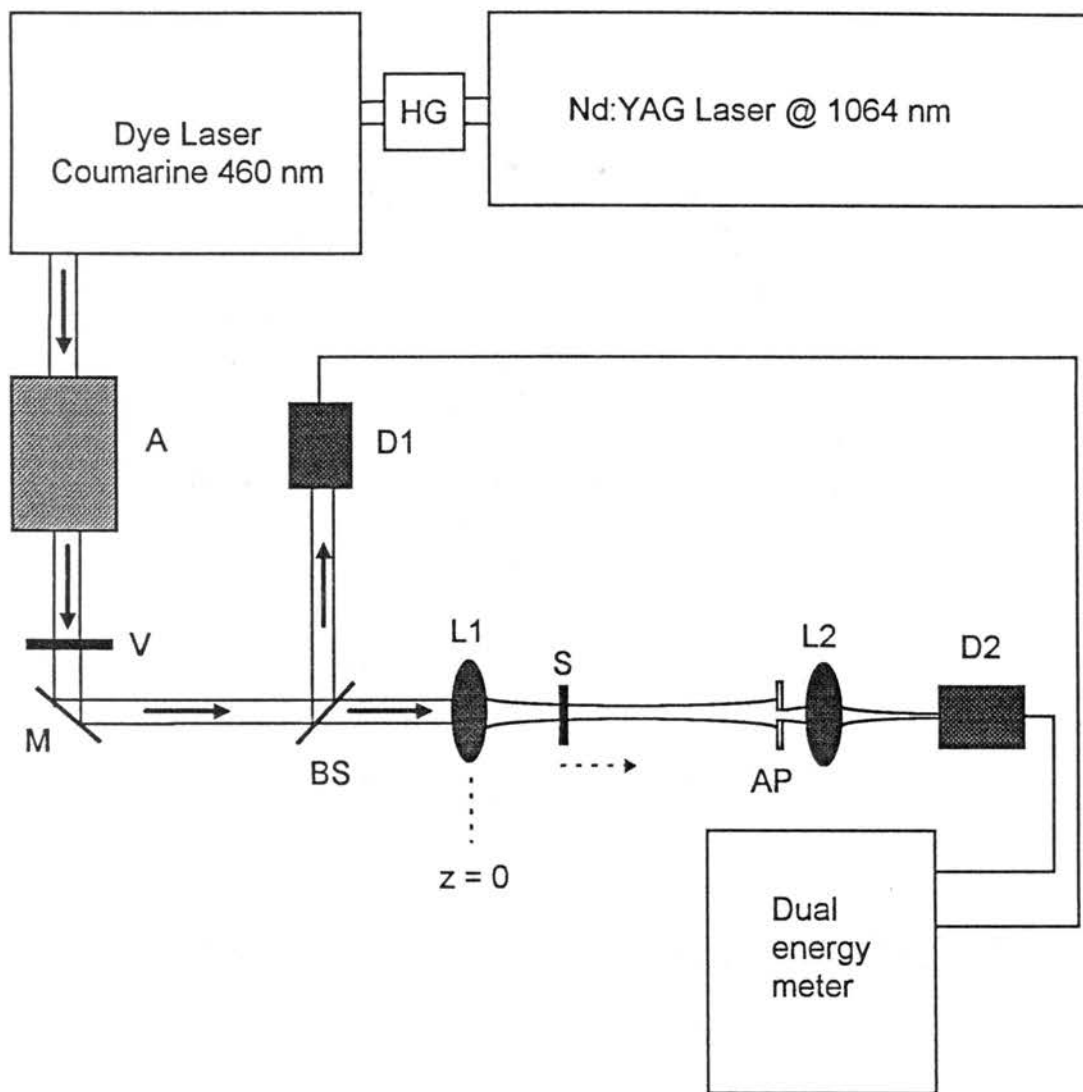


Figure III.1 Setup for Z-scan/Optical Limiting. HG - harmonic generator; A - attenuator; V - vertical polarizer; M - mirror; AP - aperture; S - sample; BS - beam splitter; L1, L2 - lens and D1, D2 - energy probes. The sample is moved in the direction of the dashed arrow for the Z-scan measurements.

translation stage that allowed translation in the direction of beam propagation (z -direction).

The Z-scans were done at a fixed energy input ranging from 10 μJ for L62 to 35 μJ for L32 within an uncertainty of about 10%. The experiments were done in single-shot mode, and each data point was recorded manually. Both energy probe readings were recorded as a function of z position. Since we had accurately calibrated the beam splitter and knew how much energy was lost through the focusing and collecting lenses (L1 and L2), we could easily find the incident and aperture transmitted energies. The ratio of the aperture transmitted energy to the incident energy was calculated for each z position. The normalized transmission was derived from the Z-scan data by dividing the scan by the first data point where no nonlinear refraction or nonlinear absorption took place.

At input energies lower than the ones used in the Z-scan measurements, the statistical laser fluctuations became a problem. At times, laser pulses with energies producing intensities exceeding the damage threshold would strike the sample. This would occur particularly near the focus of the lens. Therefore, in the focal region the sample was translated in the x and y directions such that each laser pulse would be incident upon a new region. It also enabled us to unmask the effects of accidental damage.

The sample was then fixed at the valley of the Z-scan and an Optical Limiting experiment was performed by gradually increasing the input energy while monitoring the transmission. Again, we recorded both energy probe readings. The sample was translated in the x and y direction after each laser shot which was done in order to minimize surface damage resulting from multiple laser shots.

2. Intensity-scan (nanosecond)

We performed Intensity-scan measurements on two sets of the Eu-doped alkali-silicate glasses to study their nonlinear optical properties. Specifically, we were interested in seeing how the Eu^{3+} concentration affected the nonlinearity of alkali-silicate glasses on a nanosecond time scale. The sample thicknesses varied from 2 to 5 mm. A long focusing lens was used in order to make the samples optically thin so that the thin sample approximation could be employed. The conventional Z-scan technique, for such long focusing geometry, would require a long range translation stage which we did not have. Thus, the Intensity-scan technique was used instead. The Intensity-scan technique is also insensitive to laser fluctuations which can make Z-scan measurements difficult to perform.

The first set of glasses had a systematic variation of Eu^{3+} in the following manner: $(\text{Eu}_2\text{O}_3)_x(\text{Base})_{1-x}$, where $x = 0\%$, 0.1% , 0.5% , 1% , 2.5% , and 5% , and the base consists of 70% SiO_2 , 15% Na_2O , 12% MgO , and 3% Al_2O_3 , all in mole percent. The specific compositions are shown in Table III.2. The second set had the Eu concentration at 2.5% but split the alkali concentration equally first between Na and Li and second between Na and K as shown in Table III.3. Other relevant sample parameters are listed Table III.4. These samples formed part of a group of samples that had been also been investigated via four-wave mixing, thermal diffusivity, ionic conductivity, and Raman scattering.

The Intensity-scans were performed at 532 nm, the second harmonic of the Nd:YAG laser. The laser was injection-seeded to give Gaussian temporal pulses of 10 ns FWHM. The experimental setup is the same as the one shown in Fig. III.1 but with some differences. The dye laser was bypassed by using a dichroic mirror to filter out the residual 1064 nm radiation and redirect the 532 nm

laser. The beam emerging from the laser was not circular Gaussian but quasi-top-hat in spatial profile with a radius of 4 mm. It was focused by a lens of focal length 52.5 cm. The minimum beam radius or spot size was measured to be about 50 μm giving a Rayleigh range of 14.8 mm. Our samples had thicknesses that varied from 2 to 5 mm which is smaller than the Rayleigh range; therefore, we could use the thin sample approximation. The samples were placed 15 mm after the focus. The beam radius at the sample position was measured to be approximately 70 μm . The aperture had a radius of 0.5 mm and was placed about 44 cm after the focus in a holder with x and y translation capability. Some of the samples did not have adequate parallelism and would shift the beam slightly. We had to adjust the aperture position so as to center it on the beam. If we were to perform a Z-scan, then we would encounter a systematic transmission variation due to the beam walk-off that would mask the nonlinear effects. The transmission with no sample was about 2% which means we were detecting the on-axis transmission.

The energy probe was placed immediately after the aperture and no collecting lens (L2) was required. The calibration of the probes was checked with an oscilloscope and found to be in good agreement. The reading of the dual energy meter was downloaded to a personal computer via an RS 232 connection. Each scan lasted less than a minute. Thus, many scans per sample could be obtained in a short period of time.

The beam splitter and focusing lens were accurately calibrated so that we could determine how much energy was incident on the sample. The damage threshold of the samples were determined by taking a scan in which the input energy was increased until the sample damaged. This resulted in a sudden drop in transmission, and visually the sample would scatter a tremendous amount of

light. We always worked well below the damage threshold. Since these glasses had positive nonlinearity, the samples would collimate the beam in the far-field thus raising the transmission.

Table III.2 Nomenclature and composition for Eu-doped alkali-silicate glasses with systematic Eu variation.

Samples	Eu ₂ O ₃ (% mole)	SiO ₂ (% mole)	Na ₂ O (% mole)	MgO (% mole)	Al ₂ O ₃ (% mole)
B5	0	70	15	12	3
B6	0.1	69.93	14.985	11.988	2.997
B7	0.5	69.65	14.925	11.94	2.985
B8	1.0	69.3	14.85	11.88	2.97
B9	2.5	68.25	14.625	11.7	2.925
B10	5.0	66.5	14.25	11.4	2.85

Table III.3 Nomenclature and composition for Eu-doped alkali-silicate glasses with dual alkali ions.

Samples	Eu ₂ O ₃ (% mole)	SiO ₂ (% mole)	Na ₂ O (% mole)	Li ₂ O (% mole)	K ₂ O (% mole)	MgO (% mole)	Al ₂ O ₃ (% mole)
B12	2.5	68.25	7.31	7.31	—	11.7	2.925
B14	2.5	68.25	7.31	—	7.31	11.7	2.925

Table III.4 Refractive index, absorption coefficient, density and sample thickness values of all Eu^{3+} -doped alkali-silicate glasses.

Samples	n (532 nm)	α (cm^{-1}) (532 nm)	Thickness (mm)	Density (g/cm^3)
B5	1.525	0.553	2.05	2.72
B6	1.525	0.528	2.38	2.41
B7	1.535	0.562	3.05	2.49
B8	1.535	0.597	4.30	2.51
B9	1.540	0.797	4.45	2.58
B10	1.565	1.39	4.50	2.82
B12	1.565	1.16	2.00	2.64
B14	1.555	0.870	2.80	2.57
SiO_2	1.462	0.040	3.12	2.207

Due to the very poor quality of the beam profile, we performed Intensity-scans on our samples using a fused quartz sample as a standard. Since the slope of an Intensity scan is proportional to the nonlinear refraction coefficient in the absence of nonlinear absorption, we compared the slopes of the samples to that of fused quartz. From the ratio of the slopes we calculated the nonlinear refraction coefficient for our samples. This procedure of comparing slopes has not been done before, but we justify it on the basis that for Z-scans one can compare the peak to valley transmission differences of a standard to that of a sample to get the nonlinear refraction coefficient.¹⁰

3. Intensity-scan (millisecond)

Optical nonlinearities have been studied previously on the cw and millisecond time scales for a wide variety of materials.²⁹⁻³² The dominant mechanism in these time scales for glasses has been established to be of thermal origin and is thus also known as “thermal lensing”. In order to observe thermal lensing the medium must necessarily be absorbing since it is the heat that is generated within the sample that causes the local change in the index of refraction. We have previously studied thermal nonlinearity in glasses in the millisecond regime by the Z-scan technique and also by monitoring transmitted laser pulse distortions.⁶

In this section, we present an extension of the Intensity-scan technique suitable for measuring thermal nonlinearities. The main difference between this technique and the one used in the nanosecond regime is the manner in which we monitor the transmitted beam. In the nanosecond scale, we detected the energy of the beam via calibrated energy probes. However, in the millisecond regime we use a photodiode to monitor laser pulse distortions.

We have studied thermal nonlinearity with this technique in two sets of glasses. The first set studied were the lead silicates whose composition is given in Table III.1. The second set were Eu-doped alkali-silicates that had the alkali ion vary according to the following formula: Base-M₂O, where M = Li, Na, K, Rb, and Cs. Table III.5 has the nomenclature and composition for the second set of glasses. These Eu-doped glasses have been previously investigated via four-wave mixing, Raman (both resonant and nonresonant), Brillouin, and thermal diffusivity.³³⁻³⁶ Other relevant parameters such as refractive index and absorption coefficients of all the samples used in this study are listed in Table III.6.

Table III.5. Nomenclature and composition for Eu-doped alkali silicate glasses where M = Li, Na, K, Rb, and Cs.

Samples	M ₂ O (% mole)	SiO ₂ (% mole)	Eu ₂ O ₃ (% mole)	ZnO (% mole)	BaO (% mole)
LS, M=Li	15	70	5	5	5
NS, M=Na	15	70	5	5	5
KS, M=K	15	70	5	5	5
RS, M=Rb	15	70	5	5	5
CS, M=Cs	15	70	5	5	5

Table III.6. The linear index of refraction, absorption coefficient, and sample thickness values of lead silicate glasses and Eu-doped alkali-silicate glasses.

Samples	n (514.5 nm)	α (cm ⁻¹) (514.5 nm)	Thickness (mm)
L32	1.715	0.439	1.50
L42	1.829	0.539	1.50
L52	1.922	0.556	1.56
L62	2.080	1.15	1.50
LS	1.604	0.6	2.75
NS	1.583	1.49	3.19
KS	1.584	1.98	4.01
RS	1.573	0.24	4.02
CS	1.591	0.43	4.37

Let us consider what happens to a square laser pulse as it transmits through an absorbing sample. To make the analysis easier we section the pulse into thin strips. When the first strip enters the sample it encounters a room-temperature refractive index and thus passes through linearly. The material will absorb some of the strip's energy. This will raise the temperature of the sample, and the local heating will give rise to a change in the index of refraction. The second strip now enters the sample and experiences this index change and will take up a nonlinear phase shift that will cause the beam to either focus or defocus in the far-field thus increasing or decreasing the transmission. This second strip also deposits energy raising the local temperature even more. The third strip will see an even bigger index change than the second strip and will propagate accordingly. The subsequent strips deposit energy and continue to change the index of refraction. However, heat diffusion is taking place as well. Thus, the change in the refractive index will not grow indefinitely but will reach a steady state value in which the rates of heat generation and heat diffusion are equal. This will occur provided that the pulse duration is much larger than the characteristic time for thermal diffusion $t_c = w^2/4D$, where w is the beam radius and D is the diffusivity. This time is 2-5 ms in glasses for typical thermal lensing measurements. It is easy to see that the last strip will carry information to the detector that has both linear and steady state nonlinear contributions. The first strip just contains only linear information. If we divide the transmissions of end of the pulse (T_2) by its beginning (T_1), then we have eliminated any linear contribution from the resultant normalized transmission $T = T_2 / T_1$. This method of normalization is due to Oliveira *et al.*, which they used for the Z-scan technique.³⁷ We have found that it works equally well for the Intensity-scan technique.

The experimental setup is shown in Fig. III.2. An argon-ion laser (Spectra Physics 2020) with an air-spaced etalon operating at 514.5 nm was used as the excitation source. The beam was passed through a vertical polarizer. A shutter (Uniblitz) was connected to a shutter driver (Uniblitz D122) which in turn was connected to a pulse generator (Hewlett Packard 8013B). The pulse duration was set for 50 ms with 200 ms between pulses. This was done in order to assure that the sample had sufficient time to reach steady state during the pulse and also that it had ample time to return to room temperature between pulses. The rise-time and fall-time of the pulse was about 2.5 ms.

The output of the laser was a TEM₀₀ circular Gaussian beam and was focused using a 20.4 cm lens. A 25 μm radius pinhole was placed about 40.2 cm from the lens which gave an aperture transmission of $S = 2.74 \times 10^{-3}$. Since this transmission is very small, we can conclude that we are detecting effectively the on-axis transmission. A fast photodiode (Electro-Optics Technology ET 2010) with rise time less than a nanosecond was placed immediately after the pinhole and connected to a digital storage oscilloscope (Tektronix 2440) with 500 MegaSamples/s sampling rate. The pinhole and photodiode assembly was put on an x and y translation stage. The samples were placed on an adjustable sample holder which was in turn fixed to a digital micrometer translation stage.

The focused beam radius was accurately measured to be $48 \pm 1 \mu\text{m}$ and was done in the following manner. The L62 sample which has a high absorption and is also thin was placed near the focus. The sample was then moved along the z -direction while monitoring the pulse distortion. When the sample was at the focus no pulse distortion was detected, and this position was recorded as $z = 0$. However, when the sample was placed before the focus the pulse height quickly decayed to a steady state value. The sample was moved such that the difference

between the beginning and end of the pulse was maximized while keeping the input constant. The sample position was then recorded. This position corresponds to the Z-scan valley and is $0.858z_0$, where $z_0 = \pi w_0^2/\lambda$ is the Rayleigh range. We could thus find the minimum beam radius w_0 . This method of utilizing the non-linear effects of materials to find the minimum beam radius is very reliable.

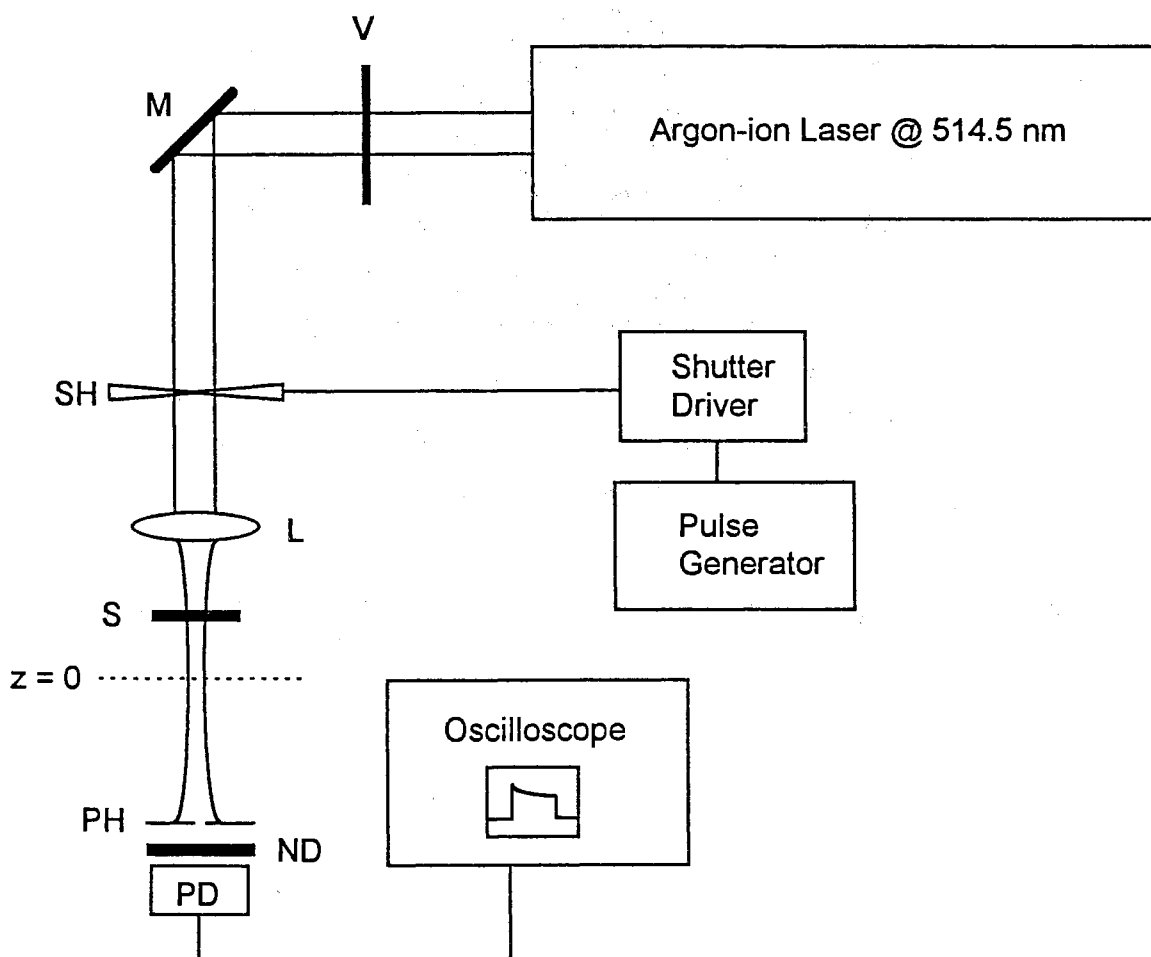


Figure III.2. Setup for Intensity-scan. V - vertical polarizer, M - mirror, SH - shutter, L - lens (20.4 cm), S - sample, ND - neutral density filters, PH - pinhole (50 μm diameter), and PD - photodiode.

We cross-checked our results with a simplified version of the scanning knife-edge technique. In this method a sharp knife-edge such as a razor blade is moved transversely across the beam along various z positions while the far-field beam pattern is monitored by eye. When the blade is moved across the focus, the beam uniformly disappears. Far from focus, the blade cuts across the beam area. The beam radius is measured at different z positions and extrapolated to find w_0 . The value obtained was $w_0 = 50 \pm 10 \mu\text{m}$. We also used the laser beam profiler to measure w_0 and found it to be $50 \pm 5 \mu\text{m}$. Both methods gave reasonably good agreement with the pulse distortion technique.

Intensity-scans were taken on the lead silicates with the sample fixed at $z = -12.1 \text{ mm}$ (before the focus) where the beam radius was $63 \mu\text{m}$. The distance from the samples to the aperture was 210 mm . The pinhole was centered on the transmitted beam very accurately by maximizing the signal with the sample in place. The Eu-doped alkali silicates were placed at a distance $z = -19.1 \text{ mm}$ where the beam radius was $81 \mu\text{m}$. The distance from these samples to the aperture was 217 mm . The Rayleigh range was 14.1 mm , and all the samples varied in thickness from 1.5 mm to 4.37 mm which is still smaller than the Rayleigh range. Therefore, we could safely use the thin sample approximation. There was a further complication in the Eu-doped glasses due to the strong fluorescence in the orange part of the spectrum when excited by 514.5 nm light. We used a 514.5 nm interference filter with a 0.8 nm bandwidth to negate the effects of fluorescence in the detected signal for the Eu-doped glasses. No fluorescence was observed for the lead silicate glasses.

Some plots of the pulse distortion from L62 are shown in Fig. III.3 at a fixed position but with different powers. How fast the pulse height decayed de-

pended on the incident power. We took an average of 32 shots for each scan to smooth out any noise. Fig. III.4 shows a typical Intensity-scan where we plot the normalized transmission versus input intensity. The slope of the line is directly proportional to the thermal nonlinear refraction coefficient. Each data point is an average of 32 shots.

What is remarkable about the technique is that we can measure extremely small nonlinear phase-shifts, much less than 0.1 rad, that the beam incurs after traversing the sample. This allows us to detect very small thermal nonlinearities. The temporal detection method has the advantage that it is minimally affected by parasitic scattering. However, the samples should not have bulk inhomogeneities or striations that would alter the path of the beam. This was not the case in some of the alkali-silicate glasses, and we had to find regions in them that were clear of striations. The KS sample was by far the worst in terms of bulk inhomogeneities. The LS sample had regions that were light blue superimposed on a yellow background. By comparison, the lead silicate samples were much better in optical quality. Great care was taken to assure the beam went through the samples undistorted.

Another important issue discovered during the experiments was the effect neutral density filters had on the experimental results when placed prior to focus. This was initially done in order to attenuate the beam beyond the point where the argon laser becomes unstable (about 20 mW). The ND filters would absorb some of the light and would thermally lens and impart a positive nonlinear phase shift to the beam. Consequently, during the 50 ms pulse the focal position of the beam would move closer to the lens (towards negative z), and as a result, the transmission would be smaller at the end of the pulse than at the beginning.

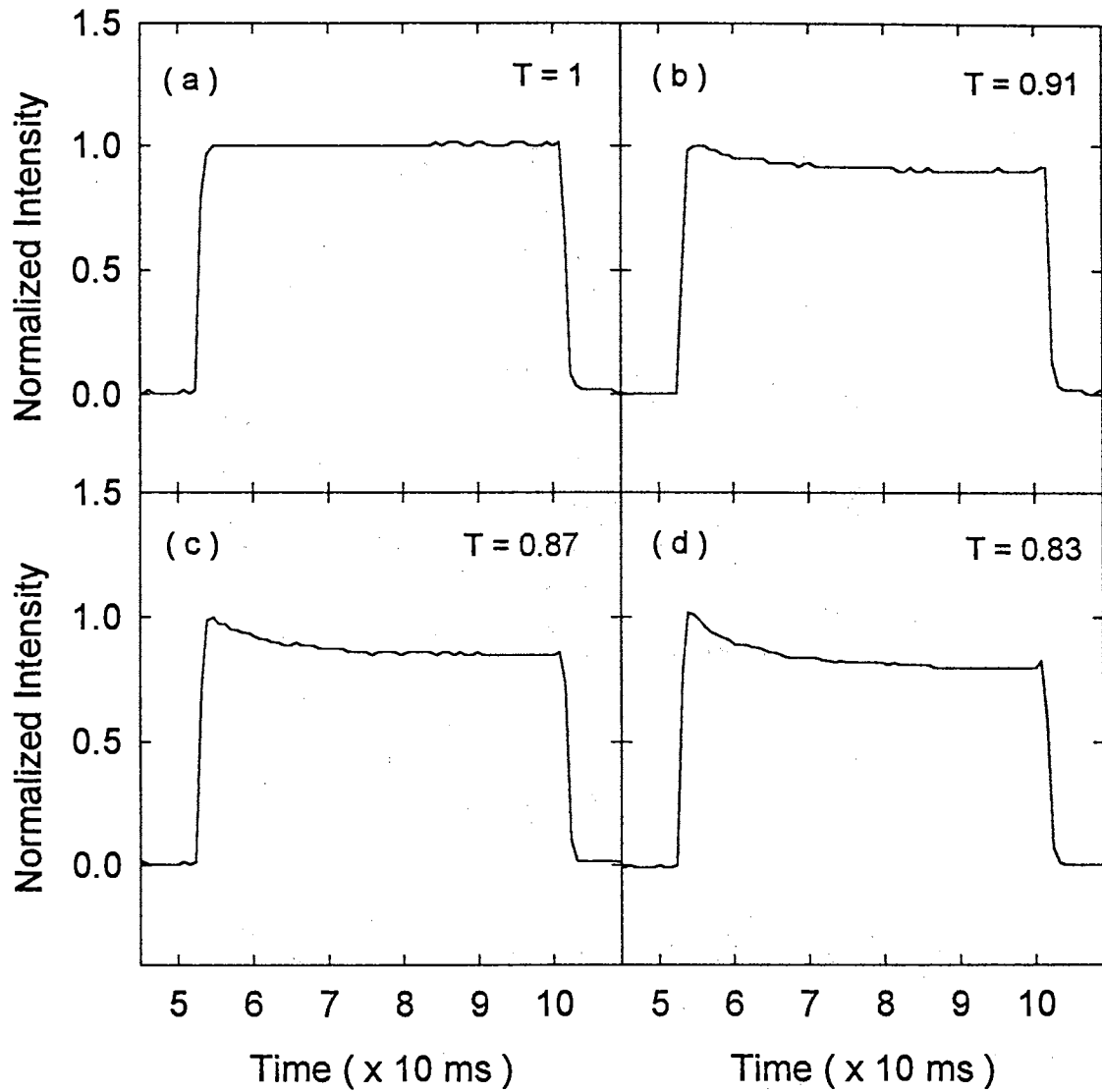


Figure III.3. Pulse distortions for L62 at different input powers. The sample is placed at $z = -12.1$ mm. T is the transmission. The power for: (a) $P = 30$ mW, with no sample; (b) $P = 30$ mW, (c) $P = 40$ mW, and (d) $P = 50$ mW.

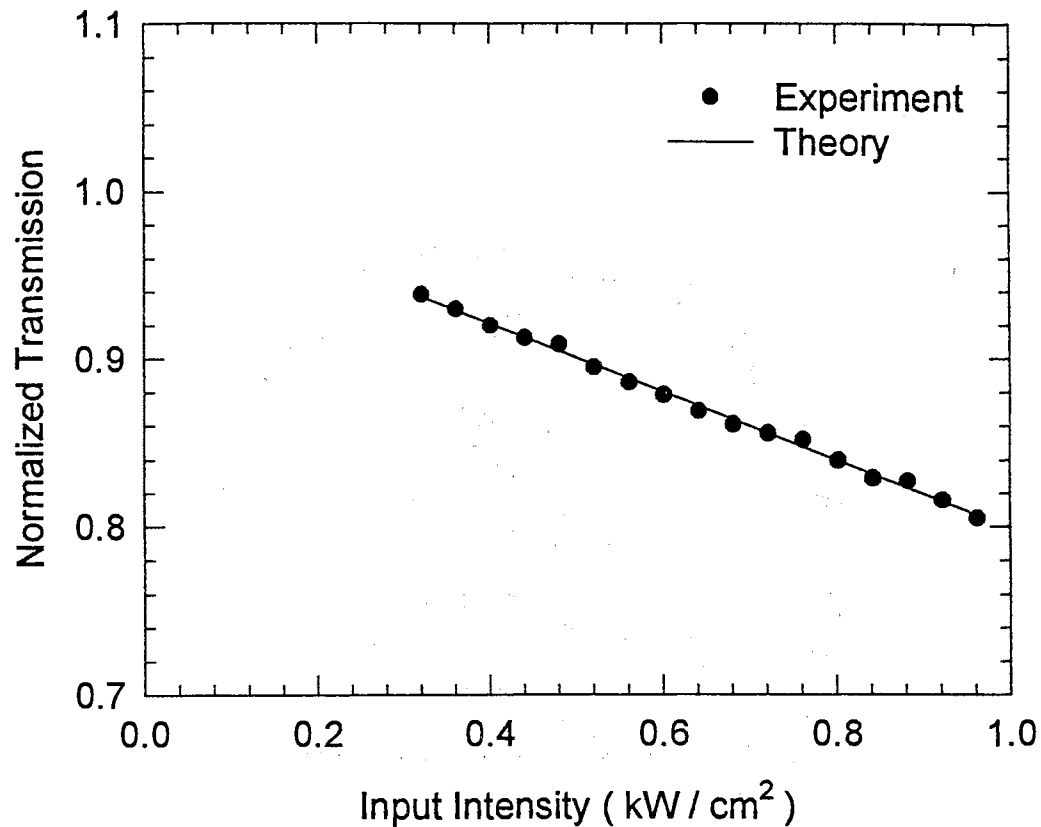


Figure III.4. Intensity-scan for L62. The sample is placed at $z = -12.1$ mm. The nonlinear refraction coefficient is $13.5 \times 10^{-8} \text{ cm}^2/\text{W}$.

The strength of the ND filter and beam power determined how large the effect was. In our experiments, we did not use ND filters prior to focus in order to avoid this complication. However, the fact that the ND filters thermally lens makes them a good choice for determining the minimum beam waist using the pulse distortion technique. A thin ND filter with high absorbance would be an ideal candidate.

4. Brillouin Scattering

We performed Brillouin scattering experiments on the lead silicate glasses and Eu-doped alkali silicate glasses with systematic Eu variation in order to study their elastic and photoelastic properties. More importantly, they provided information about the contributions of laser beam induced stress to our nonlinear optical measurements. Using the Pockel's coefficients, we can derive the electrostrictive contribution to the nonlinear refraction coefficient as well as the stress part of the thermo-optic coefficient, dn/dT .

The FP interferometer is the single most important instrument in Brillouin scattering. We review some of the fundamentals of a Fabry-Perot (FP) interferometer without going into much detail in Appendix C. This will enable us to better understand the tandem FP interferometer used in our experiments and its basic alignment.

The experimental setup is shown in Fig. III.5. An argon ion laser (Spectra Physics 2020) operating at 514.5 nm was the excitation source. An air-space etalon was inserted into the laser cavity to produce a single longitudinal mode and thus increase the coherence length of the laser. The transverse profile of the laser beam was a very clean TEM_{00} mode and had a correlation value very close to one when checked by our laser beam profiler. The beam passed through a vertical polarizer, and a small part of it was split off to act as a reference signal for the Fabry-Perot interferometer. The reference signal was further attenuated by neutral density filters. The remaining part of the beam was focused by a 20.4 cm lens onto the sample, and the transmitted beam was captured by a beam dump.

Since it is not always practical or possible to measure the absolute Brillouin scattering intensities, we measured the Brillouin intensities of our sample to

that of a fused quartz standard. This procedure of relative intensity measurements is common in Brillouin scattering experiments. The samples were mounted on an a dual sample holder which allowed us to hold the standard sample as well as the sample under investigation. The sample holder was placed in a vertical stage and could be raised or lowered. This enabled us to switch from the standard sample to our glass samples easily reproducing the same experimental conditions for each run. The vertical stage in turn was mounted on two micrometer translation stages which allowed precision motion in two dimensions. The full range of three-dimensional motion was necessary since the samples had absorption. Thus, we needed to know the exact location of the scattering volume.

The scattered light was collected by a compound lens (Olympus) of focal length 5 cm and a diameter of 4.5 mm. The lens was placed about 10 cm from the scattering volume and provided a large solid angle of collection. The image plane was located 10 cm behind the lens where a pinhole of diameter 100 μm was placed to spatially filter the signal. Another compound lens (Olympus) of focal length 5.5 cm and diameter 4.5 mm was used to collimate the beam. By using a telescope after the collimating lens, we made sure that the image of the pinhole was at the sharpest focus of the lens. The collimated beam had to be focused onto the pinhole of the Fabry-Perot (FP) interferometer entrance. Therefore, an achromatic lens of focal length 50 cm was used for proper F-matching with the FP optics and two mirrors to guide the focused beam onto the pinhole.

A photomultiplier tube (PMT, ITT FW130) was used for detecting the signal which had a circular detection area of diameter 2.5 mm. It was placed in a photomultiplier tube housing and cooled to $-25\text{ }^{\circ}\text{C}$ by a thermoelectric cooler (Products for Research). There was a continuous flow of filtered water 24 hours a day going through the system. The dark count was typically 1-2 cts/sec and had

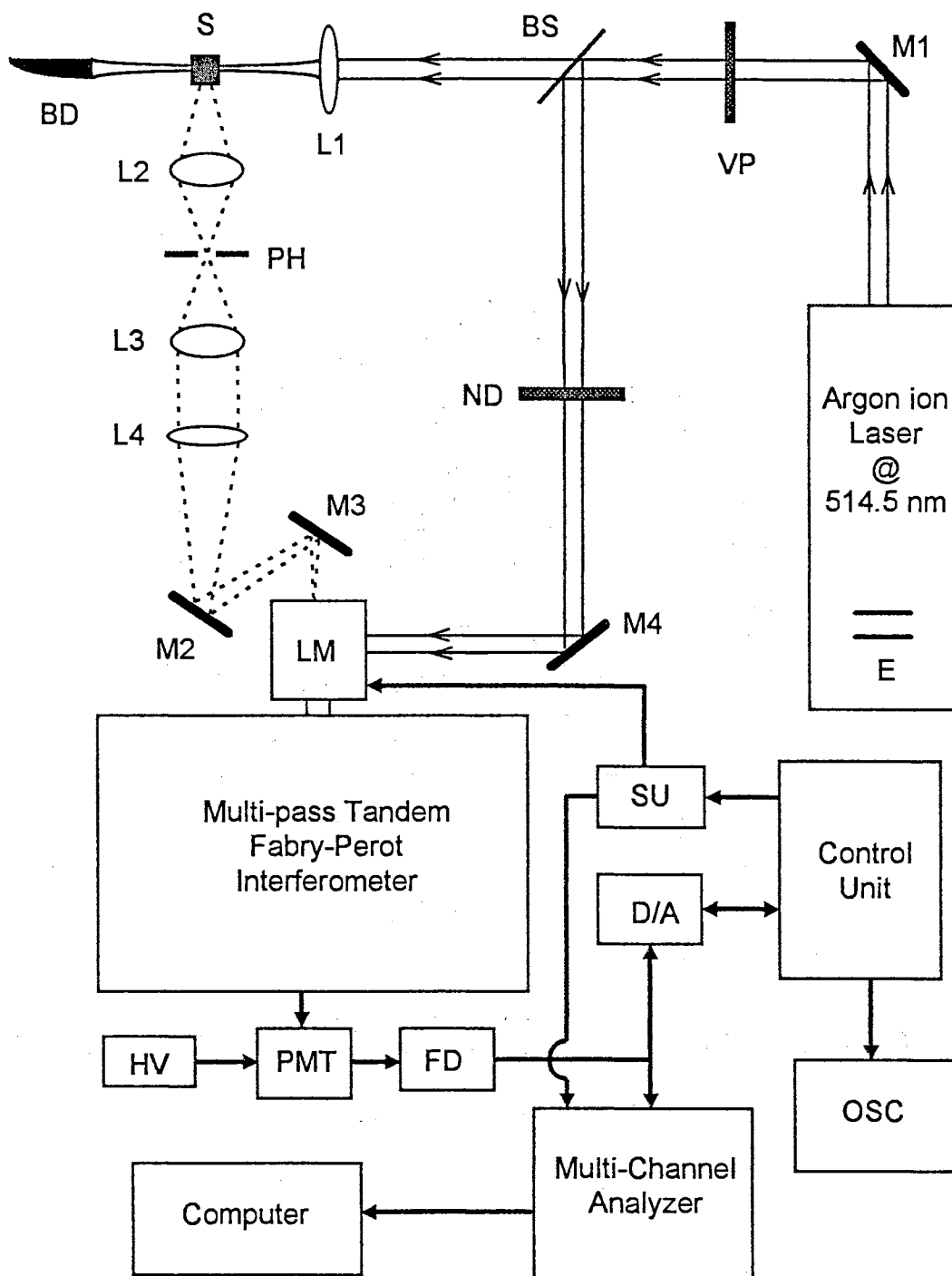


Figure III.5 Experimental setup for right-angle Brillouin Scattering. E-etalon, VP-vertical polarizer, BS-beam splitter, L's-lenses, M's-mirrors, PH-pinhole, S-sample, BD-beam dump, D/A-spectrum digital to analog converter, HV-high voltage, PMT-photomultiplier tube, FD-fast discriminator, LM-light modulator, SU-shutter unit, ND-neutral density filters.

about 10% quantum efficiency at 514.5 nm. A -2200 V voltage was supplied to the cathode of the PMT by a high voltage source (Tennelec). The output of the PMT was connected to a fast discriminator (EG&G PARC 1182) that was set to produce 50 ns TTL pulses. The output from the discriminator was then split for monitoring and stabilizing the FP, and also data acquisition. The data was collected in a multichannel analyzer (MCA, Canberra 35 plus) and then downloaded to a personal computer (IBM XT).

The signal that was split for stabilization and monitoring first went through a spectrum digital to analog converter and then on to the interferometer control unit. The output spectrum from the control unit was monitored on an oscilloscope (Soltec 520) in real time. The control unit also provided the trigger for the multichannel analyzer and also provided the signal to the shutter unit which controlled the light modulator.

The details of the complete FP alignment is quite complex and will not be discussed. Assuming that there is no gross misalignment problems, we outline the everyday alignment procedure of our overall system that is required before taking data. The alignment of the external optics was carefully checked with light scattered from a Teflon or metal block. The interferometer box cover was slid open, and a card was placed before the beam went into the FP1 mirrors (first FP). By going to the smallest possible pinhole size (150 μm diameter), we verified that the input beam was correctly focused through the pinhole by adjusting the mirrors M2 and M3 that are placed before FP1. The card was then removed, and a glass slide was placed before the light modulator to verify that the back-reflection from FP1 was cleanly coming through the pinhole. The FP system was then switched to reflection mode, and the scan amplitude on the inter-

ferometer control unit was set to one order. Such a setting allowed us to see clearly two orders from both FP interferometers. An example of that is shown in Fig. C.3. The background level was increased by tweaking the alignment mode optics.

After this point, the FP alignment was done electronically, and we were ready to take data. We generally scanned only one order so that the observed spectra would have a central Rayleigh peak and side Brillouin peaks. The input and output pinhole of the FP interferometer were set at 450 μm and 700 μm , respectively. The mirror spacing was set at 2.5 or 2.75 mm giving a free spectral range (FSR) of 2 or 1.818 cm^{-1} . The contrast was about 10^9 , and the overall finesse, approximately 120. The dwell time on the MCA was set for 0.5 ms/ch, and each FP scan lasted 0.5 seconds. Each data file contained 1024 channels (histogram) and took anywhere from 30 to 60 minutes to collect. The reflection spectra were inverted and fitted along with the corresponding data files with the commercial software Peakfit. The integrated area and peak position were accurately reported for each Brillouin component, and an entire spectrum took about 5 minutes to fit.

5. Temperature-dependent Absorption Measurements

We performed temperature-dependent absorption measurements on the lead silicate glasses to further our understanding of their thermal nonlinear optical properties. It is well-known that the changes in the absorption coefficient and index of refraction are related to one another by a Kramers-Kronig transformation. Our aim was to study the change in the absorption spectra with temperature and

then derive the corresponding change in the index of refraction. This would allow us to calculate the thermo-optic coefficient dn/dT that is due to homogeneous heating. In what follows, we describe the samples, instrumentation and procedure of temperature-dependent absorption measurements.

The samples were all cut and polished to optical quality into dimensions of $1 \times 1 \times 0.1$ cm³. This was done to match the dimensions of the sample holder cavity and ensure good thermal contact. The spring loaded sample holder not only let us secure the sample but also enabled us to minimize the applied external stress. This was very crucial to our experiment since we were interested in the change in the index of refractive due to thermal heating with no stress applied to the sample.

The experimental setup is shown in Fig. III.6. The absorption measurements were done in a Cary 05 spectrometer. The samples were housed in a dewar with quartz windows (Janis CCS 400). The dewar in turn was attached to a cryopump with a cold head (Leybold RGD 210). The cryopump was connected to a water cooled He compressor or refrigerator (Leybold RW 3) with a pair of flexible steel He gas lines (Leybold FL2). The compressor provided the necessary pressurized He gas to the cold head as well as its electrical power. The cold head then used this compressed He gas to produce the very low temperatures needed for cryopumping the dewar. The dewar and cryopump were evacuated with the help of a vacuum controller (Balzers TCP 121) connected to a roughing pump (Balzers DUO 1.5A) which in turn was connected to a turbomolecular pump (Balzers TPH 060). The pressure inside the dewar was monitored by a pressure controller (Balzers TPG 300). The temperature was varied in the dewar by an autotuning temperature controller (Lakeshore 320) with stability better than 0.1K. A temperature monitor (Omega 6102) was also used for safety reasons to

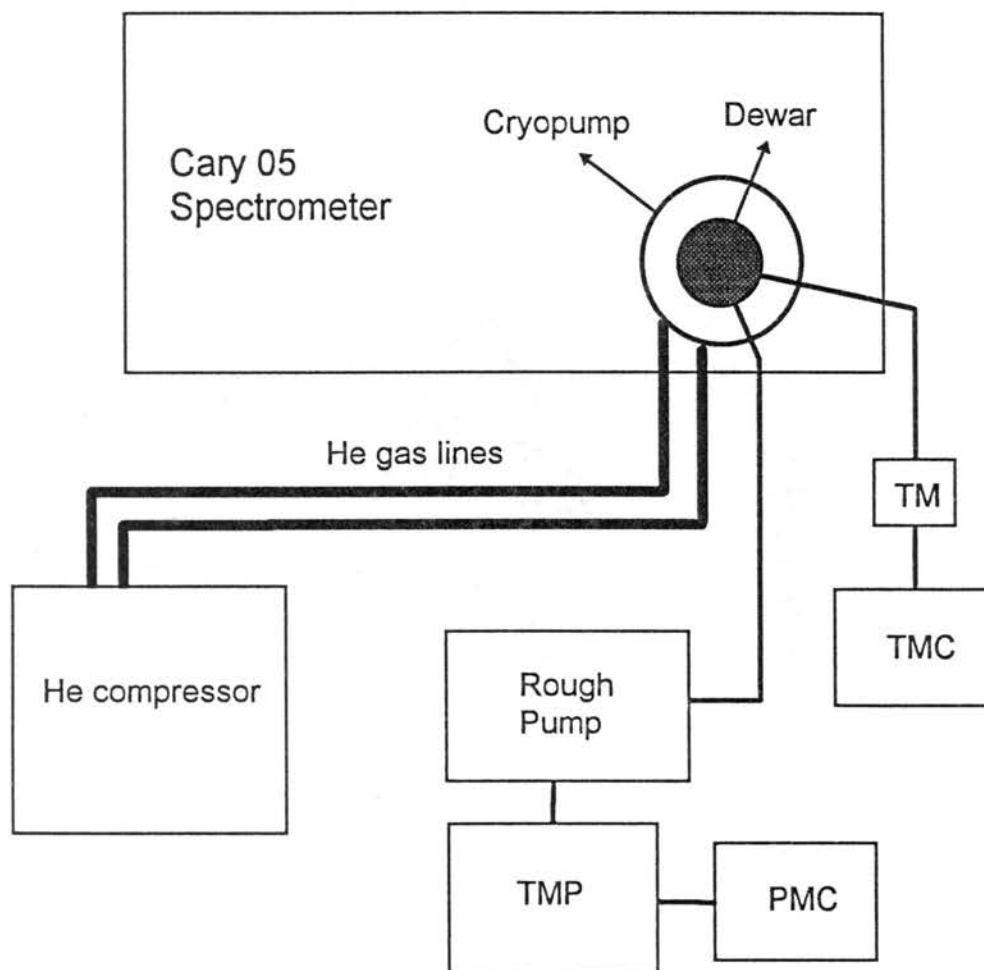


Figure III.6. Experimental setup for temperature-dependent absorption measurements. TM - safety temperature monitor, TMC - temperature monitor and controller, TMP - turbo-molecular pump, PMC - pressure monitor and controller.

shut off the heater if the temperature became dangerously high.

The samples were carefully mounted in the dewar and the dewar was then placed in the spectrometer. We pre-evacuated the cryopump down to its starting pressure of about 1 mTorr by turning on the roughing pump and then slowly

opened the dewar valve. When the combined dewar and cryopump pressure was about 10 μTorr , the He compressor was activated, and the final dewar chamber pressure was held at 1 μTorr for the experiments. The heater was turned on, and the temperature was increased in 40 K intervals starting from 290 K to 450 K. Each scan lasted about an hour and was always reproducible.

We also performed room-temperature absorption measurements on the Eu-doped alkali-silicate glasses that had the systematic variation in Eu. The rich spectrum of the Eu^{3+} ion was clearly observed and were found to be in good agreement with known Eu^{3+} transitions.

6. Refractive index and density measurements

In this section, we present an enhanced version of the Brewster's angle experiment to measure the refractive index of materials.³⁸ The Brewster's angle experiment is usually performed to get a quick estimate of the refractive index to about one or two decimal places. The technique requires one polished surface and can be done on both transparent and opaque materials. At the Brewster's angle, only *s*-polarized light is reflected.³⁹ That is, if our incident light is *p*-polarized, then ideally we should not detect any reflected light. In practice, however, the reflected intensity reaches a minimum. The reflected intensity for *p*-polarized light at an angle θ is:⁴⁰

$$R_p(\theta) = \frac{(a - \cos \theta)^2 + b^2}{(a + \cos \theta)^2 + b^2} \times \frac{(a - \sin \theta \tan \theta)^2 + b^2}{(a + \sin \theta \tan \theta)^2 + b^2} \quad (\text{III.1})$$

$$\text{where, } a^2 = \frac{1}{2} \left\{ \sqrt{(n^2 - k^2 - \sin^2 \theta)^2 + 4n^2 k^2} + (n^2 - k^2 - \sin^2 \theta) \right\} \quad (\text{III.2})$$

$$b^2 = \frac{1}{2} \left\{ \sqrt{(n^2 - k^2 - \sin^2 \theta)^2 + 4n^2 k^2} - (n^2 - k^2 - \sin^2 \theta) \right\} \quad (\text{III.3})$$

Here, $k = \alpha\lambda / 4\pi$ is the extinction coefficient, α is the absorption coefficient, and λ is the wavelength. It is important to point out that the reflectivity will be slightly altered in the presence of absorption. This will lead to a small increase in the Brewster's angle. However, for the small absorption coefficients ($\sim 1 \text{ cm}^{-1}$ or less) in our glasses $k \ll n$, and this does not pose a problem.

The intensity change, as one rotates through the Brewster's angle, can be monitored by eye. We have found that by introducing a CCD camera with a laser beam profiler to monitor the intensity change, we can isolate the angle close to the resolution of the sample rotation stage. By using the relation $n = \tan \theta_B$, the refractive index is easily found. The uncertainty in the refractive index measurement is typically in the third decimal place.

The experimental setup is very simple and can be quickly assembled, as shown in Fig. III.7. Apart from the sample and laser source, the experiment requires a sample holder, rotation stage, CCD camera connected to a laser beam profiler, and neutral density filters to attenuate the beam going into the camera. It is very important to make sure the incident laser beam is perpendicular to the sample surface since the Brewster's angle is measured with respect to this normal. This can be easily accomplished by aligning the back-reflected beam with the incident one. However, to be more accurate, we place a pinhole concentric with the incident laser beam and close to the laser source. We align the back-reflected diffraction rings so that they are properly centered on the pinhole. The

greater the distance between the sample and the pinhole the greater the assurance the beam is normal to the sample. We can therefore eliminate (or minimize) the uncertainty in our Brewster's angle measurements that comes from initially non-normal beams. The pinhole can subsequently be removed or a variable aperture can be used in its place.

We now carefully rotate the sample and place a card about 10 to 20 cm from it and monitor the change in the reflected intensity by eye. Once we approximately find this angle from the surface normal, we move the CCD camera in place. By making small rotational increments, we can see the intensity dip through a minimum on the monitor of the laser beam profiler as we rotate through the Brewster's angle. This reflected intensity change can be observed on the monitor of the laser beam profiler as a change in the color of cross section of the beam and also the peak intensity of the beam profile. We can adjust the gain

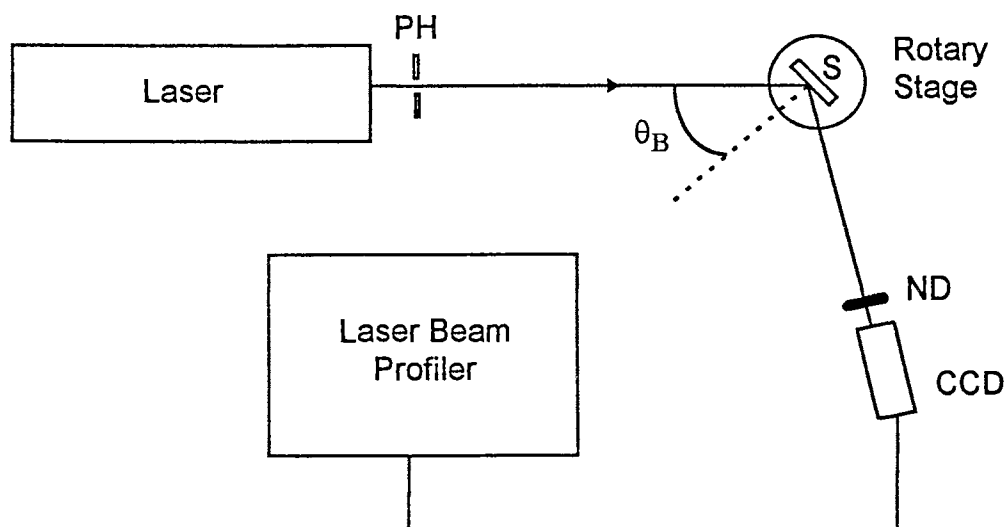


Figure III.7 Setup for measuring the refractive index using a CCD camera and laser beam profiler. ND - neutral density filters; PH - pinhole; S - sample; θ_B - Brewster's angle.

and background level on the camera and accurately find the angle close to the resolution of our rotation stage which is 0.01° .

The introduction of the CCD camera along with the laser beam profiler makes the detection of the Brewster's angle simple to do. The fact that the CCD camera has a larger effective detection area than most photodiodes and PMT's, and the fact that the reflected beam does not have to be centered on this area makes the CCD camera a better choice for this experiment. We can easily scan through the Brewster's angle without having to adjust the camera position. This is particularly advantageous since the reflectivity near the vicinity of the Brewster's angle is a very shallow function. In addition, we can adjust the gain and background level on the camera to better isolate the angle.

We have used this technique to measure the refractive indices of *some* of the glass samples used in this study. Actually, it was the need to quickly and accurately measure the refractive indices of glass samples that were provided to us by a collaborator and to whom the samples had to be returned to intact, that lead to the development of this refined Brewster's angle technique.

To demonstrate the usefulness of the technique, we found the refractive index of a fused quartz sample with this method that had previously been measured with the minimum-deviation technique.³⁶ At 514.5 nm, the Brewster's angle was found to be $55.63^\circ \pm 0.05^\circ$ giving a refractive index of $n = 1.462 \pm 0.003$. This compares quite well with the previously measured $n = 1.462 \pm 0.001$. The uncertainty reported is larger than that of the minimum-deviation technique because we found it hard to accurately isolate the Brewster's angle any better than $\pm 0.05^\circ$ as a result of laser fluctuations. The reason for this is that the monitored

reflected intensity change is the determining criteria for the Brewster's angle. With better laser stability, it should be possible to push the uncertainty to ± 0.001 .

Although we found a slightly larger uncertainty in our refractive index measurements than the standard minimum-deviation technique, we can perform the experiments relatively quickly. We also avoid the time-consuming sample preparation that is needed with the minimum-deviation technique since only one polished surface is required with the Brewster's angle method. Furthermore, if a sample has striations as was the case with some of the glasses, then a laser beam passing through it may become distorted which would lead to large errors in the refractive index measurements.

We could further enhance the technique by measuring the reflected intensity at various angles near the Brewster's angle.⁴¹ The data could be fitted using a cubic equation which is the lowest-order polynomial that accounts for the asymmetry in the reflectivity. We could then accurately find the Brewster's angle by using the standard method of calculating roots of an equation. The resultant uncertainty in the index of refraction from this more involved measurement has been demonstrated to be ± 0.0001 .⁴¹ However, in its present form, the ease, quickness and accuracy with which our experiment can be performed makes it an attractive method for measuring the refractive index of materials.

We also measured the density of the glass samples. Since they were parallelepipeds of sides that varied from 1 to 2 cm and thicknesses that ranged from 2 to 5 mm, we accurately measured the dimensions using a micrometer and separately weight them on a digital balance. This gave us the density to three significant figures.

CHAPTER IV

RESULTS AND DISCUSSION

1. Lead Silicate Glasses

(a) Structural Properties

The emphasis of this dissertation concerns the nonlinear optical properties of lead silicate and Eu-doped alkali silicate glasses. A discussion of the structural properties of these glasses will undoubtedly shed light on our experimental results. In this section, we will discuss some of the basic structural properties of lead silicate glasses. In particular, we will review some of the available vibrational spectroscopy and x-ray diffraction data. A thorough review of lead in glasses is beyond the scope of this work but can be found in the article by E. Rabinovich⁴² and references therein. At the outset, we stress that the structural properties of glasses have not been fully established and there are many aspects of glasses that are not well understood. This fact will be made evident by the existence of different structural models of lead silicate glasses.

The first x-ray study of binary lead silicate glasses was done by Bair⁴³ in 1936 who looked at PbO mole concentrations of 9.5, 19.9, 31.2, 39.9, 49.8 and 60%. The results were interpreted by a trial and error method. He made the following bond length assignments: Pb-O (2.5 Å), Si-O (1.6 Å), Si-O (4.0 Å, next nearest neighbor), Si-Si (3.2 Å), Si-Si (5.2 Å, next nearest neighbor), and Pb-Si

(3.8 Å). The calculations based on density measurements showed that the Pb-Pb distance varied between 4.0 Å to 6.5 Å depending on the lead concentration. He suggested that these glasses contained a continuous, randomly oriented silicon-oxygen tetrahedra with a lead atoms distributed in the network like a gas.

Bair's conclusions were strongly contested by Krogh-Moe⁴⁴ since Bair did not allow for the strong Pb-Pb interaction in his calculations. This interaction can be understood as the ability of the lead ion to form a dipole due to its strong polarizability. From x-ray diffraction studies of a lead silicate glass with 58.8 mole % of PbO, Krogh-Moe found the bond lengths to be 1.6 Å for Si-O, 2.5 Å for O-O and Pb-O, and 3.9 Å for Pb-Pb, Pb-Si, and Pb-O. The Pb-O distance leads to a lead-oxygen coordination number between 6 and 10. The density was found to be 6.75 g/cm³ from which the average volume occupied by a lead atom was 65.3 Å³. From these measurements, he found that a Pb-Pb distance of 4.03 Å, corresponding to a lead-lead coordination number of 6, was closest to the observed value of 3.9 Å. Krogh-Moe stressed that high lead concentration glasses can not be described by the random-network theory.

Bagdyk'yants *et al.*⁴⁵ studied five lead silicate glasses with concentrations of 20, 33, 40, 50, and 60 mole % of PbO by electron diffraction. They found the Pb-Pb distance to be 4.2 Å and therefore had a lead-lead coordination number of 9. They concluded that in high-silica glasses, the Pb atoms are randomly distributed in the gaps of the three-dimensional SiO₄ tetrahedral network with each lead atom being linked to two oxygen. The lead-oxygen coordination number increases to 6 as the PbO concentration is increased and the three-dimensional Si-O network gradually breaks down into two and one-dimensional clusters.

Brosset⁴⁶ studied the PbO-*x*SiO₂ systems with *x*=0.56, 0.92, and 1.53 using x-ray diffraction. He observed that the peak position at 3.9 Å due to Pb-Pb

did not change with lead concentration implying that there is a well-defined lead-oxygen grouping with primarily covalent bonds. NMR investigations of lead silicate glasses by Bray *et al.*⁴⁷ revealed the presence of PbO_4 pyramidal structures. They also found pyramidal structures in crystalline lead silicate.

Mydlar *et al.*⁴⁸ studied the structure of 2PbO-SiO_2 , PbO-SiO_2 , and PbO-2SiO_2 glasses using x-ray diffraction and calculating radial distribution functions (RDF). They found that the peak at 3.8 Å in PbO-SiO_2 and in 2PbO-SiO_2 is made up of several Pb-Pb distances. The peak is very sharp and almost disappears when there is less PbO which suggests that lead is not randomly distributed in these glasses. For the Pb-Pb distances, they calculated the first nearest Pb to be at 3.6 Å, two more at 4.15 Å, and another at 4.8 Å. Furthermore, they agreed with Brosset's conclusion that the lead atoms are distributed in the glasses in a systematic manner. The RDF's of crystalline PbSiO_3 and PbO (red-tetragonal and yellow-orthorhombic) were also compared with the lead silicate glasses. They found that the Pb-Pb distances in the glasses are only slightly larger than those found in the crystals. They concluded that the lead in these glasses forms Pb-O-Pb chains similar to those found in PbO around which the SiO_4 tetrahedrals wind. This is thought possible because the Pb^{2+} is nearly as large as the O^{2-} and a little smaller than the SiO_4 tetrahedral edge. In the PbO-2SiO_2 system, the chains seem to be almost straight. In the PbO-SiO_2 system, the chains show a twisting effect and the twists are more pronounced in 2PbO-SiO_2 . A diagram of possible Pb-O-Pb chains are shown in Fig. IV.1.

Gotz *et al.*⁴⁹ used chemical methods to determine the type and percentage of silicate groups in binary lead silicate glasses ranging in composition from 4PbO-SiO_2 to PbO-SiO_2 . The results indicated that the relative amounts of

tribution of silicate anions, they postulated the existence of Pb-O-Pb groups which forms the basic structure of PbO. This is in agreement with Mydlar *et al.*

Morikawa *et al.*⁵⁰ studied the structure of 2PbO-SiO₂ by x-ray diffraction and concluded that most of the lead atoms form covalent PbO₄ pyramids and these pyramids form zigzag chains. The chains are bridged and modified by the monosilicates, disilicates, trisilicates, tetrameric rings, chain-forming polysilicates, and ionic PbO₆ octahedron. Morikawa *et al.* suggested that this is the manner in which lead plays the role of a network former in high lead silicate glasses. Their structural model is a further developed version of the original zigzag chain proposed by Mydlar *et al.* Leventhal *et al.*⁵¹ observed chemical shifts of ²⁰⁷Pb in PbO-SiO₂ glass as a function of PbO concentration which suggest that there is also some ionic character to these glasses. In that sense, the lead also acts as a network modifier. Due to the existence of both ionic and covalent Pb in the silicate glasses, Morikawa suggested that the PbO₄ zigzag chains exist over a wide range of composition. Finally, we note that Imaoka *et al.*⁵² performed x-ray diffraction measurements on PbO-SiO₂ and 2PbO-SiO₂. For the PbO-SiO₂ system, they developed a structural model consisting of chains of (PbO₃)_n pyramid that are joined into double layers by chains of SiO₄ tetrahedra. For the 2PbO-SiO₂ system, the (PbO₃)_n pyramidal chains were connected by the various silicate anion groups. Imaoka *et al.* also pointed out that the strong resemblance in the RDF's of the PbO-SiO₂ and 2PbO-SiO₂ systems suggests that they must have the lead atoms similarly arranged.

Another useful tool for probing the structure of glasses is vibrational spectroscopy, such as infra-red absorption and Raman scattering. We performed Raman scattering experiments on the lead silicate glasses and hence present a brief

report on the findings. The excitation source was an Argon-ion laser (Spectra-Physics 2020) operating at 514.5 nm with 400 mW. The incident light was vertically polarized and the scattered light was collected via a 90° geometry. The spectrum was analyzed using a double grating monochromator (Instruments SA) with a resolution of 1 cm⁻¹. The Raman spectra from the lead silicate glasses are shown in Fig. IV.2.

Shuker and Gammon⁵³ proposed that because there is a lack of long-range symmetry in a glass, all the vibration modes that do not have a center of inversion take place in first-order scattering, and so the spectra of glasses also exhibit the phonon density of states. Our results on the Raman spectra agree with those obtained previously by Worrell *et al.*⁵⁴ The first band at approximately 30 cm⁻¹ increases in relative intensity with an increase in the silica content. It has been shown by Hass by doing low temperature studies that this band is due to thermal agitation of the silica network.⁵⁵ This first band appears to be a universal feature of glasses due to its connection to the amorphous state and has been termed the boson peak. It has been experimentally shown by Dixon *et al.*⁵⁶ that the boson peak is due to phonon modes that are localized. Novikov *et al.*⁵⁷ developed a model in which the boson peak is considered to arise from first-order light scattering by quasi-localized harmonic vibrations. They further showed that the boson peak is predominantly due to transverse-type atomic motions.

The Raman band at 90 cm⁻¹ is definitely due to the presence of the lead since it is absent in the Raman spectra of fused quartz. The origin of this weak band is uncertain, but Worrell speculates that it might be due to the perturbation caused by Pb²⁺ ions in the silica lattice. The strong band that appears at 135 cm⁻¹ is due to a Pb-O stretching mode. From the spectra, we can see that

the relative intensity of this band increases with increasing PbO concentration. It is also strongly polarized which is suggestive of a totally symmetric stretching mode of an isotropic vibrating unit. This conclusion is further supported by the appearance of a similar strong and narrow band in crystalline PbO.⁵³

The shoulder effect near 450 cm^{-1} is associated with the Raman active angular bending mode of vibration of O-Si-O. The small band at 800 cm^{-1} decreases in relative intensity with increasing PbO concentration. The band centered at about 950 cm^{-1} arises from a two types Si-O stretching modes since any Pb-O stretching modes should be at a lower frequency due to the large atomic mass of lead. The band near 1000 cm^{-1} decreases in relative intensity with increasing PbO and is more polarized than the shoulder at 950 cm^{-1} . An explanation for this is that the introduction of the Pb^{2+} ions into the silica network breaks some of the Si-O bond and the resulting silicate anions have different degrees of polymerization. The lead atoms weaken the Si-O bond, and lowers its stretching mode frequency from 1065 cm^{-1} . In that sense, Pb^{2+} also acts as a glass network modifier. Thus, the Raman spectra reveals that the lead atoms are arranged in the glass with some degree of symmetry as is suggested by x-ray diffraction measurements.

In light of the x-ray diffraction and Raman scattering measurements, we may conceptualize that lead will likely form Pb-O-Pb chains or pyramidal units and act like a network modifier when the PbO concentration is small. These same pyramidal units will link up with the two or one-dimensional silicate anion groups and form a network for large PbO concentrations. In both cases, there may also be ionic Pb^{2+} present in the glass.

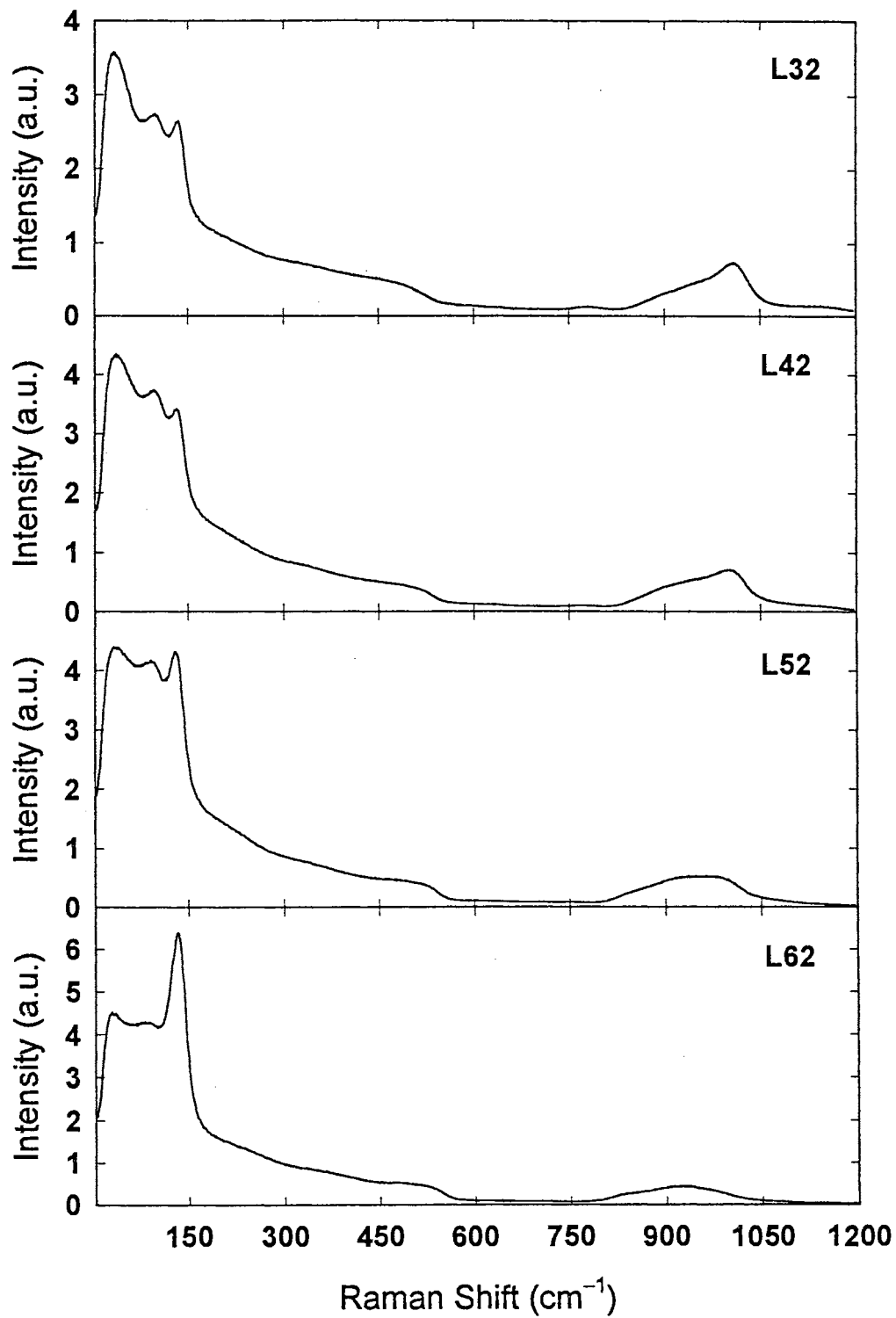


Figure IV.2 Raman scattering from binary lead silicate glasses with PbO concentrations of 32, 42, 52, 62% all in mole %.

(b) Brillouin Scattering

In a glass, vibrational modes with small wavelengths can not be represented by plane waves due to the disorder of the amorphous system. The Ioffe-Regel criterion for eigenstates with well-defined wavevectors vectors q is $q > 1/\Lambda$, where Λ is the mean free path of the phonon. This criterion does not hold for small wavelength vibrations in a glass because the plane-wave states are strongly scattered by the inhomogeneities in the density and elastic properties of the system, thus limiting Λ .⁵⁶ However, we have seen in Chapter II that the long wavelength acoustic excitations in glasses can be described successfully by plane waves with well defined q . We may thus speak of acoustic phonons in glasses just as we would in crystals.

The Brillouin scattered spectra for the lead silicate glasses are shown in Fig. IV.3 for a backscattering geometry. As mentioned in Chapter II, scattering by TA phonons in this configuration are not allowed. Thus, one can unambiguously study the LA phonons. The free spectral range (FSR) was set at 2.5 cm^{-1} . Each Fabry-Perot scan lasted about 0.5 s and a sample run consisted of 1000 scans. The incident powers at the samples were 54 mW. As can be clearly seen from the spectra, the LA Brillouin shift decreases, i.e., the LA phonons become less energetic, and the scattered intensity increases as the PbO concentration increases. The LA phonon sound velocities and corresponding elastic constants are in excellent agreement with those obtained from the right-angle scattering geometry.

Another interesting feature that appeared after carefully fitting the data with Peakfit was that there was a consistent and reproducible difference between the Stokes and Anti-Stokes shift. The Anti-Stokes shift was slightly greater than the Stokes shift. This difference was extremely small (on the order of 10^{-3} cm^{-1})

and increased from L62 to L32. Eq. II.55 neglects higher order terms in v_B/c and the exact expression for the Brillouin shift (cm^{-1}) for a backscattering geometry is

$$\Delta\omega_{B\pm} = \frac{2nv_B}{c\lambda_0} [1 \mp (nv_B/c)]^{-1} \quad (\text{IV.1})$$

where, + refers to the Anti-Stokes shift and the - refers to the Stokes shift.⁵⁸

From this expression, we can see that the Anti-Stokes shift is slightly larger than the Stokes shift as we have observed. However, the difference in Stokes and Anti-Stokes shift from Eq. IV.1 would be on the order of 10^{-5} cm^{-1} for our glasses which is smaller than the difference we detected by two orders of magnitude. Since the Rayleigh line was blanked out, the center of the scan was taken to be the peak of the reference beam. This may have contributed to the larger differences we observed. Pine had mentioned in an article on Brillouin scattering that this asymmetry between the Stokes and Anti-Stokes shift was predicted by several authors but had not been experimentally resolved.⁵⁸ Pine suggested that semiconductors would be good candidates to observe this asymmetry due to their high refractive indices and large dispersion. It seems that glasses with high refractive indices, such as lead glasses, may also be good candidates.

The Brillouin spectra for the lead silicate glasses in a right-angle scattering geometry are shown in Fig. IV.4. The spectra are scaled to show the TA phonons. The mirror spacing was set for 2.750 mm giving a FSR of 1.818 cm^{-1} so that we could clearly resolve the TA peaks. The Fabry-Perot scan time was about 0.5 s, and 6000 scans were taken for each run for L62, L52 and L42. For L32, 3000 scans were taken for each run. The incident power was varied for the samples; L62 had 100 mW; L52 and L32 had 200 mW; L42 had 300 mW. The TA phonon shift decreases as PbO concentration increases similar to the behavior of the LA phonons. We did not detect any TA phonons for L42 even for long

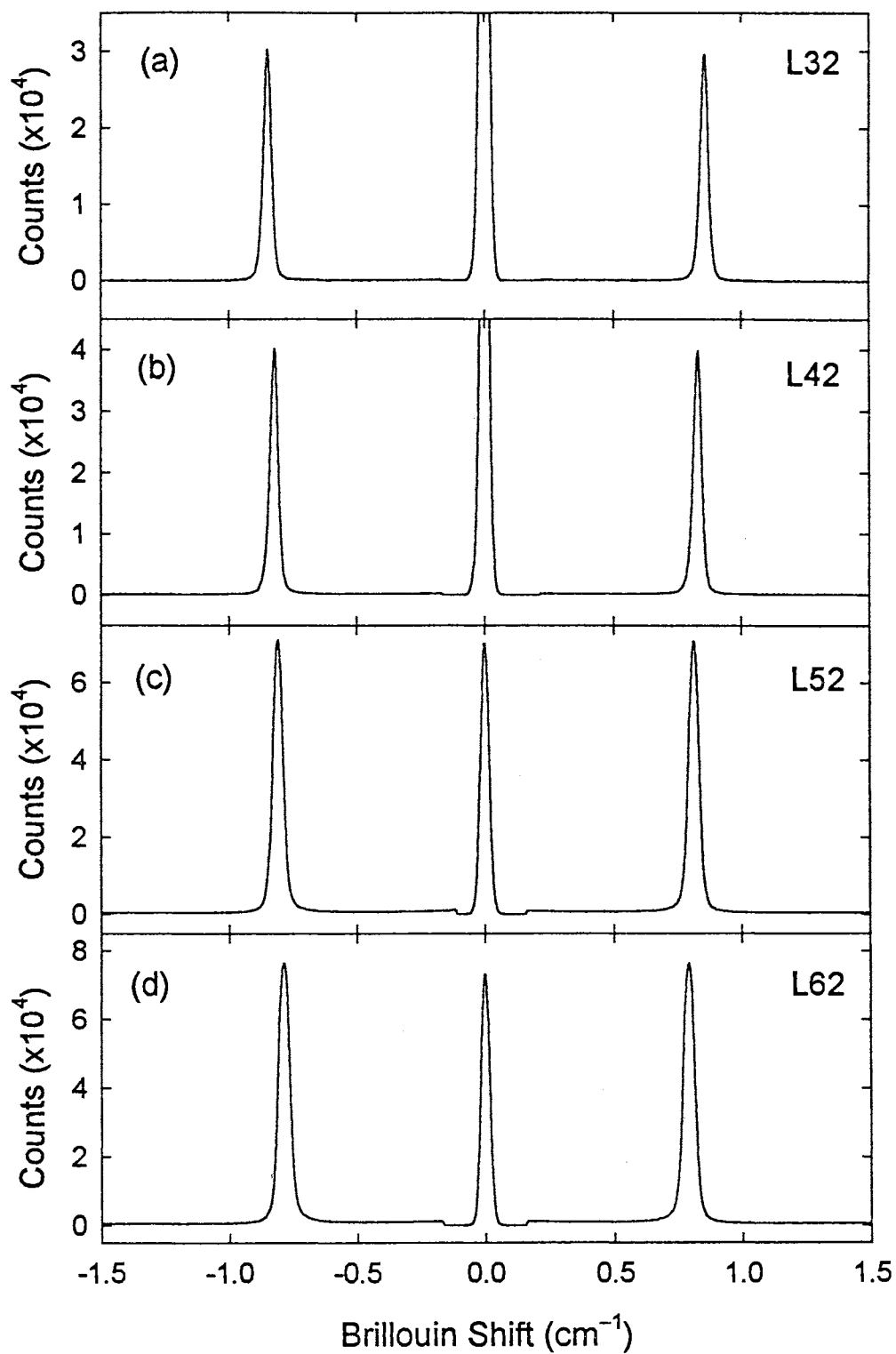


Figure IV.3 Brillouin spectra for lead silicate glasses in a back-scattering geometry. (a) L32; (b) L42; (c) L52; (d) L62. The incident power was 54 mW.

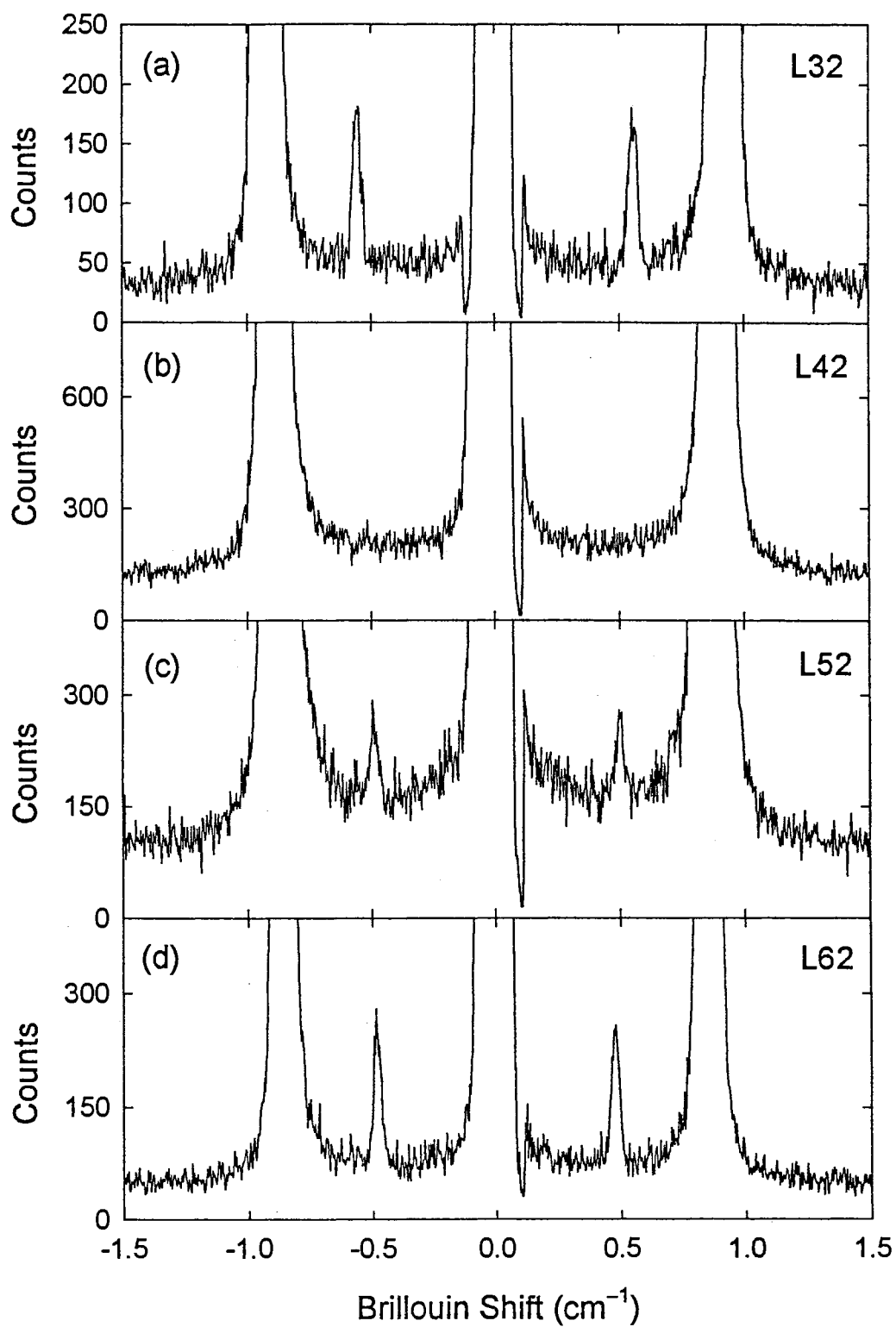


Figure IV.4 Brillouin spectra for lead silicate glasses in a right-angle scattering geometry. (a) L32; (b) L42; (c) L52; (d) L62. TA phonons were not detected for L42.

collection times and high powers. These lead silicate glasses exhibit strong thermal lensing characteristics, i.e., optical nonlinearity caused by thermal heating, and thus care was taken not to use too high an incident power.

The acoustic phonon velocities of our samples were calculated from the measured Brillouin shifts using Eq. II.55. The Brillouin shifts for a right-angle geometry are shown in Table IV.1 along with the density and refractive index. The refractive index was measured by the minimum deviation principle, and the density was calculated by a direct volume and mass measurements.

Table IV.1 The density, refractive index and Brillouin shifts for lead silicate glasses for a right-angle geometry.

Sample	Density (g/cm ³)	n (514.5 nm)	$\Delta\omega_{\text{LA}}$ (cm ⁻¹)	$\Delta\omega_{\text{TA}}$ (cm ⁻¹)
L32	4.51 ± 0.01	1.715 ± 0.001	0.6053 ± 0.0003	0.3627 ± 0.0004
L42	5.32 ± 0.01	1.829 ± 0.001	0.5844 ± 0.0004	not detected
L52	6.03 ± 0.01	1.922 ± 0.001	0.5752 ± 0.0002	0.3247 ± 0.0007
L62	6.83 ± 0.01	2.080 ± 0.001	0.5644 ± 0.0007	0.3137 ± 0.0008

The errors quoted in the Brillouin shifts are the standard errors done from many measurements. Several points are immediately obvious. Both the refractive index and density increase with PbO concentration. This is to be expected because of the large atomic weight of the Pb and also the UV absorption edge shifts towards the visible as PbO are increased. The density and refractive index measurements are in agreement with values found by other authors.^{48,59} In addition,

the Brillouin shifts decreases by 7% (about 0.4 cm^{-1}) for the LA phonons and about 14% (almost 0.5 cm^{-1}) for the TA phonons as the PbO concentration increases from 32% to 62% mole.

The sound velocities are shown in Table IV.2 with their corresponding elastic constants. The elastic constants were calculated using $c_i = \rho v_i^2$, where i represents the TA or LA phonon. The errors were calculated from standard error analysis. The uncertainties in the velocity Δv and elastic constants Δc were determined from

$$\frac{\Delta v}{v} = \frac{\Delta(\Delta\omega)}{\Delta\omega} + \frac{\Delta n}{n} + \frac{\cos \theta/2}{2 \sin \theta/2} \Delta\theta \quad (\text{IV.2})$$

$$\frac{\Delta c}{c} = \frac{\Delta\rho}{\rho} + \frac{2\Delta v}{v} \quad (\text{IV.3})$$

where $\Delta\omega$, Δn , and $\Delta\rho$ are the uncertainties in Brillouin shift, refractive index, and density, respectively. The uncertainty in the scattering angle due to refraction and collection optics is $\Delta\theta = b'/f_2 n$ where $f_2 = 55 \text{ mm}$ and $b' = 3.04 \text{ mm}$. This term dominates over the other terms in the velocity uncertainty and varies from 1.85° (0.032 rad) to 1.52° (0.026 rad). The derivation for $\Delta\theta$ can be found in Ref [36].

The Brillouin shifts of the LA phonon and the associated sound velocities and elastic constants from the back-scattering geometry are shown in Table IV.3. The observed shifts agree very well with calculated shifts assuming values from the right-angle geometry. The sound velocity and elastic constants are well within the error bars shown Table IV.2.

The LA velocity decreases by 23%, and the TA velocity decreases by 29%. From Table IV.2, we see that c_{11} decreases by 11%, and c_{44} decreases by 23% as

Table IV.2 The velocities of the LA and TA phonons and their corresponding elastic constants of the lead silicate glasses obtained from a right-angle scattering geometry.

Sample	v_{LA} (10^5 cm/s)	v_{TA} (10^5 cm/s)	c_{11} (10^{10} dynes/cm ²)	c_{44} (10^{10} dynes/cm ²)
L32	3.849 ± 0.066	2.307 ± 0.041	66.8 ± 2.4	24.0 ± 0.9
L42	3.485 ± 0.057	not detected	64.6 ± 2.2	not detected
L52	3.264 ± 0.050	1.842 ± 0.031	64.2 ± 2.1	20.5 ± 0.7
L62	2.960 ± 0.044	1.645 ± 0.027	59.8 ± 1.9	18.4 ± 0.6

Table IV.3 The Brillouin shift of the LA phonon, and its corresponding velocity and elastic constant for lead silicate glasses obtained in a back-scattering geometry.

Sample	$\Delta\omega_{LA}$, meas. (cm ⁻¹)	$\Delta\omega_{LA}$, cal. (cm ⁻¹)	v_{LA} (10^5 cm/s)	c_{11} (10^{10} dynes/cm ²)
L32	0.8523	0.8559	3.833	66.3
L42	0.8258	0.8265	3.482	64.5
L52	0.8109	0.8134	3.254	63.8
L62	0.7894	0.7983	2.927	58.5

we go from L32 to L62. Fig. IV.5 shows the dependence of the elastic constants on the PbO concentration or, equivalently, the density.

The macroscopic elastic constants reveal information about the interatomic forces of a material. Indeed, it is the microscopic bond strengths that determines the material's elastic properties, and this is reflected in the magnitude of the elastic constants. Eq. II.56 is actually the generalized Hooke's law for a continuum, and so the elastic constants are the tensorial analog of the simple one-dimensional spring constant.

Since the elastic constants decrease with increasing PbO concentration, we may conclude that the structure of the glass becomes weaker. By weak, we mean the following. The three-dimensional silicon-oxygen tetrahedral network breaks up into a two and one-dimensional silicate network and also into silicate anion groups due to the presence of lead pyramidal structures. At first glance, it appears that the break up of the silicate network alone explains the trend in data. However, some of these lead pyramidal structures are connected to one another in chains and to the broken up silicate network or some of the silicate anion groups. There may also be isolated units of both the lead and silicon type. That is, at low concentrations lead can act as a network modifier and as a network former at high concentrations. The fact that the elastic constants decrease with increasing PbO concentration suggests, apart from the weakening of the structure due to the break up of the silicate network, that the bonds connecting the lead pyramidal structures together may not be as strong as the silicon-oxygen tetrahedral connection in the silicate network. If the bonds were stronger, then we would expect an increase in the elastic constants as we go from L32 to L62. Therefore, the break up of the stronger silicate network, along with the emer-

gence of the weaker pyramidal chains, results in a decrease in the elastic stiffness of the glasses with increasing PbO concentration.

The fact that the structure of the glass weakens as PbO is increased was very apparent during the cutting and polishing of these samples. The time required to cut and polish L62 samples were considerably less than for the L32 samples. The L62 samples were also soft and damaged very easily.

We can derive other important material parameters from our measured elastic constants. These values are listed in Table IV.4. The linear elasticity or Young's modulus E is defined as the ratio of an applied stress T to the fractional change in length $\Delta l/l$ in the direction of the applied stress.⁶⁰ That is, a smaller E corresponds to an easily strained material. It can also be expressed in terms of

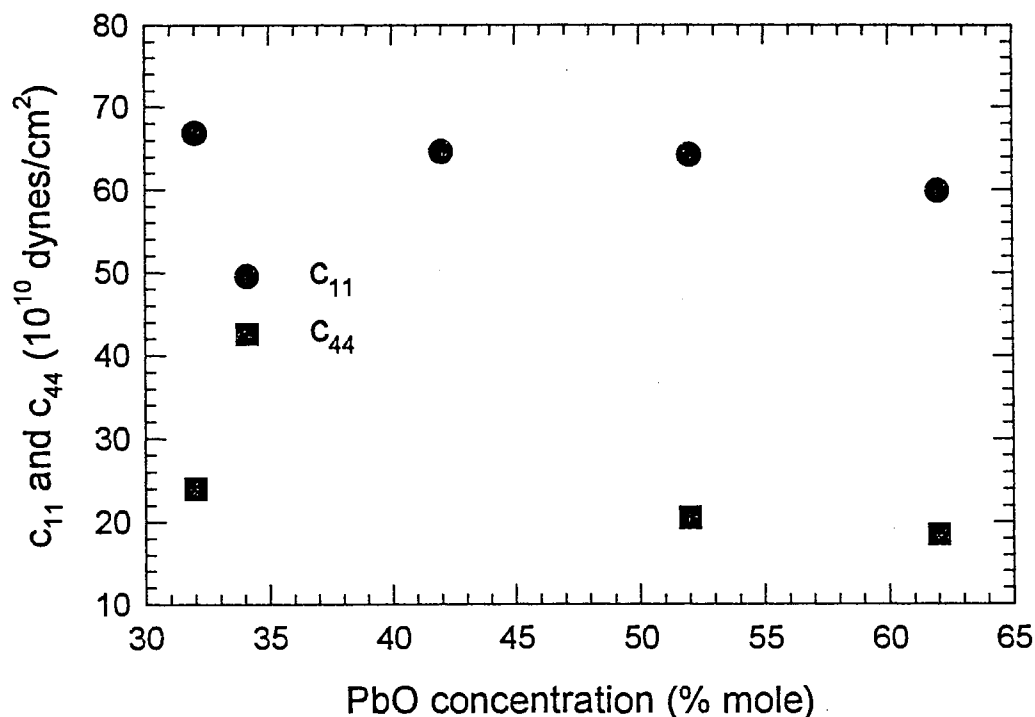


Figure IV.5 Elastic properties of the lead silicate glasses.

Table IV.4 Poisson's ratio, Young's Modulus and bulk modulus for lead silicate glasses. The values for L42 could not be calculated because no TA phonon was detected.

Sample	Poisson's ratio	Young's modulus (10^{10} dynes/cm ²)	Bulk modulus (10^{10} dynes/cm ²)
L32	0.220	29.3	34.8
L42	-	-	-
L52	0.265	25.9	36.9
L62	0.276	23.6	35.1

the elastic constants as $E = c_{44} (3c_{11} - 4c_{44}) / 2(c_{11} - c_{44})$. The Young's modulus decreases with PbO concentration indicating that the structure becomes progressively weaker.

The adiabatic compressibility κ is defined as the ratio of the fractional change in volume $\Delta V/V$ due to an applied pressure p . That is, a bigger κ corresponds to a more easily compressed material. The adiabatic bulk modulus B is the reciprocal of the compressibility and is given by $B = c_{11} - \frac{4}{3}c_{44}$.⁶¹ No meaningful trend in B can be established from the data because the TA phonon from L42 was not detected.

We can also calculate the Poisson's ratio σ which is defined as the ratio of the fractional change in length in the direction of the applied stress to the fractional change in length perpendicular to the applied stress. It is given by the formula $\nu = (c_{11} - 2c_{44}) / 2(c_{11} - c_{44})$. The Poisson's ratio for the lead silicate

glasses steadily increases from 0.220 for L32 to 0.276 for L62 demonstrating that the bond nature becomes progressively ionic.

Finally, we will discuss the photoelastic behavior of the lead silicate glasses. The expressions used to derive the photoelastic constants were given in Eq. II.64 and Eq. II.65. As mentioned in Chapter II and III, the method used to determine the photoelastic constants involved comparing the integrated intensity of the Brillouin spectrum of the sample to that of a standard with known photoelastic constants. The standard used in our measurements was fused quartz with $p_{12} = 0.279$ and $p_{44} = -0.0792$.

Since the samples absorbed some light at 514.5 nm, we had to take absorption into account in our measured ξ values. Recall, ξ is the ratio of the integrated intensities of the LA phonons of the sample to that of fused quartz. The details of accounting for absorption is given in Ref [36]. Briefly, as the incident light enters the sample and travels a distance x to the scattering volume it decreases in intensity due to absorption. The Brillouin scattered light, collected at right-angles to the incident beam, is further attenuated as it travels a distance y to the exit plane facing the collecting lens. The ξ value decreases linearly with the total distance $x+y$. To extract out the effects of absorption from ξ , $x+y$ was extrapolated to zero. The ξ value thus obtained was free of absorption and was used in our calculations. The absorption of fused quartz at 514.5 nm was found to be 0.04, and so the decrease in ξ comes predominantly from the absorption in the lead glasses.

Two other important correction factors have to be applied to ξ before it can be used in Eq. II.64; namely, the solid angle and back-reflection corrections. Details of these correction factors can be found in Ref [36]. The scattered light

collected depends on both the collection optics and the refractive index n of the sample. The solid angle correction due to refraction increases ξ by $(n/n^0)^2$. The superscripts 0 refers to the fused quartz sample. Furthermore, as the scattered light leaves the sample, refraction causes the observed size of the scattering volume to be reduced. This why there is a volume ratio $(V^0/V)^{\frac{1}{2}}$ of the sample to that of fused quartz in Eq. II.64. However, this ratio is very close to one for all the samples and can be neglected. The back-reflection correction increases ξ by $\left(1 + R^0 \exp[-2\alpha^0 L^0]\right) / \left(1 + R \exp[-2\alpha L]\right)$, where R is the percentage reflection, α is the absorption coefficient, and L is the length of the sample. The absorption-free ξ , and correction factors are shown in Table IV.5.

The measured photoelastic constants p_{12} and p_{44} along with the ratio of the integrated intensity of the TA to LA phonons are shown in Table IV.6. By increasing the PbO concentration, the Brillouin scattered intensity of the LA phonons increases as is evident from the trend in ξ values. Another important feature is that the scattering from TA phonons are much smaller than that of LA phonons. This is due to the fact that the LA phonon perturbs the dielectric constant much more than the TA phonon. The value of the photoelastic constants show an opposite trend to that of ξ . We will try to understand the mechanism behind this trend in the photoelastic constants from existing physical models. In particular, we will apply the Carleton model of photoelasticity to our glasses.⁶²

Carleton developed the strain dependence of the Fixman formulation of the dielectric constant. He expressed the photoelastic constants p_{12} , p_{11} , and p_{44} with the following formulae:

$$p_{11} = \frac{(n^2 - 1)^2}{n^4} \left(\frac{\epsilon_0}{\alpha' \rho} + \frac{4}{15} - \frac{14}{15} \Gamma \right), \quad (\text{IV.4})$$

$$p_{12} = \frac{(n^2 - 1)^2}{n^4} \left(\frac{\epsilon_0}{\alpha' \rho} - \frac{2}{15} - \frac{8}{15} \Gamma \right), \quad (\text{IV.5})$$

$$\text{and } p_{44} = \frac{(n^2 - 1)^2}{n^4} \left(\frac{1}{5} - \frac{1}{5} \Gamma \right), \quad (\text{IV.6})$$

$$\text{where } \Gamma = \frac{3\alpha'}{4\pi\epsilon_0} \int_0^\infty \frac{g_{12}(r)}{r^4} dr. \quad (\text{IV.7})$$

Here, n is the refractive index, ϵ_0 is the permittivity of free space, α' is the free particle polarizability, ρ is the density, and g_{12} is the two-particle correlation function. The first term in the brackets (after multiplying by the refractive index term) of Eq. IV.4 and Eq. IV.5 represents the change in the refractive index due to density changes produced by the strain caused by the propagation of LA phonons. Such a density term does not appear in Eq. IV.6. This can be explained as

Table IV.5 The ξ value and correction factors for the lead silicate glasses.

Sample	ξ	Volume ratio	Solid-angle correction	Back-reflection correction
L32	2.97	0.9991	1.376	0.9925
L42	4.46	0.9988	1.565	0.9864
L52	5.20	0.9985	1.728	0.9791
L62	7.89	0.9982	2.024	1.000

Table IV.6 The photoelastic constants of the lead silicate glasses and ratio of integrated intensity for the TA to LA phonon.

Sample	p_{12}	$ p_{44} $	I_{TA}/I_{LA}
L32	0.283	0.076	0.0101
L42	0.285	0.000	0.0000
L52	0.268	0.012	0.0031
L62	0.260	0.024	0.0134

follows. As an LA phonon propagates through the material, the distances between neighboring atoms vary in the direction of propagation. This is because an LA phonon is a compressional wave. However, the neighboring atomic distances do not change in the propagation direction for a TA phonon. Hence, we would expect p_{11} and p_{12} to be density-dependent but not p_{44} .

A graph of the density dependence of p_{12} and p_{44} is shown in Fig. IV.6. In accordance with the Carleton model, there is a small degree of density-dependence of p_{12} . This is similar to the behavior of c_{11} which we attributed to the weakening of the glass structure. However, there is also a density-dependence of p_{44} which seems to be quite large. Schroeder⁶³ observed a small p_{44} density-dependence for binary glasses but not for ternary systems. Our data shows that p_{44} first decreases to zero and then begins to increase. Although the density dependence of p_{44} will not be studied further, we will try to understand the behavior of p_{44} in terms of structural changes.

The second term in the brackets of Eq. IV.4 and Eq. IV.5 and the first term in brackets of Eq. IV.6 represents a change in the polarizability associated with a network distortion. The change in the atomic positions due to the strain

produced by the propagating phonons give rise to the network distortion. This displacement of the charge centers has some degree of regularity. Hence, we shall term this the lattice effect (LE) in accordance with other researchers.⁶⁴ The last terms in the brackets of Eq. IV.4, Eq. IV.5, and Eq. IV.6 represents the polarizing effects of the neighboring atoms on each other which we will term the atomic effect (AE).⁶⁴

We may write $p_{44} = LE - AE$. Since the lattice effect is only a function of the refractive index, we may use the measured values of p_{44} to determine the atomic effect. These values are shown in Table IV.7. We note that p_{44} must be negative in order to predict the correct density dependence of p_{12} . The lattice

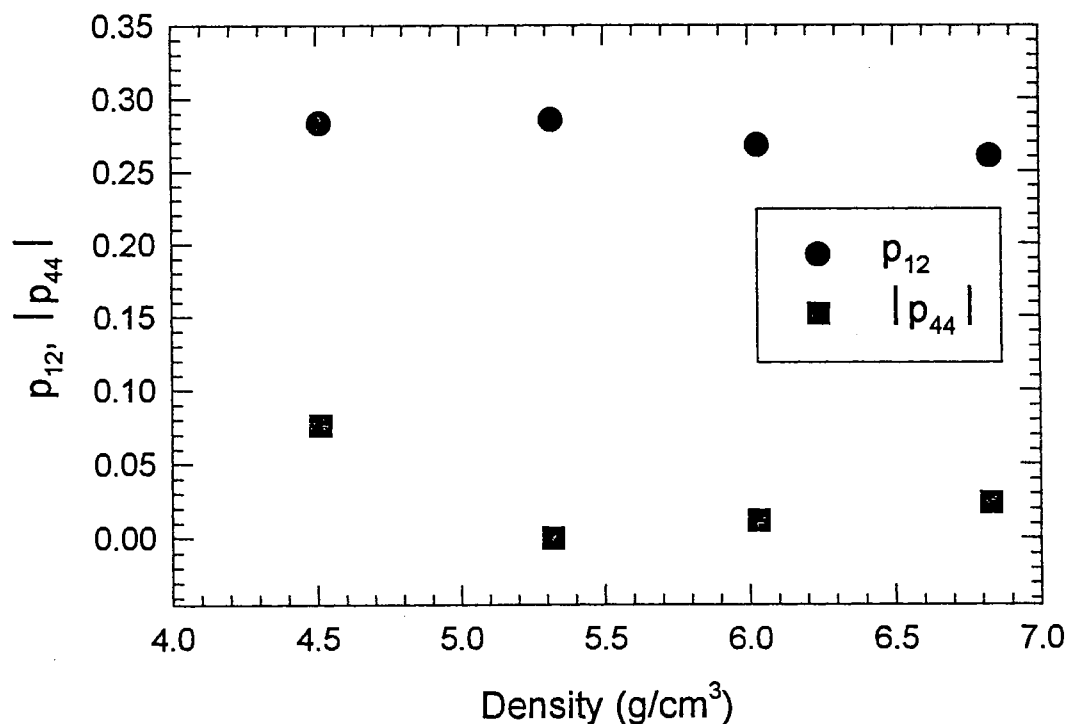


Figure IV.6. Density-dependence of the photoelastic constants for lead glasses.

effect increases with PbO concentration showing that the network distortion by the TA phonon becomes easier as we go from L32 to L62. This is understandable since we concluded earlier from our elastic constant measurements that the structure becomes weaker. The lattice effect of fused quartz is 0.057 which is smaller than the lead silicate glasses.

On the other hand, the atomic effect first decreases and then increases with PbO concentration. The Si-O bond in fused quartz is highly covalent, and the oxygen electrons are strongly bound to the bonds. When there is a strain in the material due to the propagation of the phonons, the electron cloud of the bridging oxygen will distort in the direction of the strain. The electrons of the oxygen will then respond differently to the incident light field in the direction parallel to and perpendicularly to the strain.⁶⁴ This gives rise to a large atomic effect for fused quartz (0.136). Matusita *et al.*⁶⁵ assumed that the electron clouds of the nonbridging oxygen do not to distort in the direction of the strain and hence should not contribute much to the atomic effect.

Table IV.7 The lattice and atomic effects and p_{44} of the lead silicate glasses.

Sample	p_{44}	Lattice Effect	Atomic Effect
L32	-0.076	0.087	0.163
L42	0.000	0.098	0.098
L52	-0.012	0.106	0.118
L62	-0.024	0.118	0.142

The L32 sample has an atomic effect value higher than in fused quartz. This suggests that in L32 the atoms in the Pb-O-Pb chains easily distort giving rise to an atomic effect. When this atomic effect is added to that of the partially broken up silicate network, the resulting effect is 20% larger than that of fused quartz. In L42 it appears that a structural change is taking place. The Pb-O-Pb chains are probably forming lead pyramidal structures and are not well connected to each other. The silicate network is also broken up more than it was for L32, therefore producing less of an atomic effect. The net atomic effect is about 28% smaller than that of fused quartz. The lattice and atomic effects are equal to each other in L42, and thus we could not detect any TA phonons from this sample. The atomic effect rises in L52 and is now 13% smaller than that of fused quartz demonstrating that in this system perhaps the lead pyramidal units are starting to form a better connection. The atomic effect from the silicate network is even less than that of L42. Finally in L62, the net atomic effect is 4% larger than that of fused quartz. The lead pyramidal chains probably have a better connection giving rise to a larger atomic effect.

The atomic effect results derived from Brillouin scattering show that there is probably a structural change taken place as the PbO concentration is increased. The glass appears to be changing from a silicate type network to a more looser lead-based network in accordance with structural studies.⁴⁸⁻⁵² If this is indeed taking place, then the monitoring of the TA phonons as a function of concentration seems to be a good method of detecting the structural change.

(c) Temperature-dependent Absorption

In this section, we present the results of the temperature-dependent absorption measurements on the lead silicate glasses. The initial purpose of this study was to determine the thermo-optic coefficient dn/dT that is caused by homogeneous heating of the material. This is the dn/dT that is most often reported in literature. The dn/dT that arises from inhomogeneous heating caused by a Gaussian laser beam, i.e., thermal lensing, will invariably contain stress components. We were interested in finding a stress-free dn/dT and then correlating the effects of the stress components which could be derived from Brillouin scattering.

The measurements were accomplished by monitoring the change in the absorption coefficient of the samples as a function of temperature and then using a Kramers-Kronig transformation to find the corresponding change in the index of refraction. The Kramers-Kronig transformation is given by

$$\Delta n(\lambda, \Delta T) = \frac{PV}{2\pi^2} \int_0^{\infty} \frac{\Delta \alpha(\lambda', \Delta T)}{(\lambda'/\lambda - 1)} d\lambda' \quad (\text{IV.8})$$

where Δn , $\Delta \alpha$, and ΔT are the changes in the refractive index, absorption coefficient and temperature, respectively, and λ is the wavelength. PV stands for principle value of the integral. This method had been successfully employed to study the temperature change in the band gap of ZnSe by St. John *et al.*⁶⁶ The integral extends to infinity which is, of course, impossible to accommodate experimentally and a finite range from 750 nm to 250 nm was established.

However, upon performing the Kramers-Kronig transformation we found the dn/dT values to be negative. The dn/dT of these glasses are positive which we have verified from thermal lensing measurements. The problem was traced back to the fact that the ultraviolet absorption in these glasses dominates the in-

tegral. In fact, the electronic absorption in the UV almost completely determines the refractive index in the visible. Nevertheless, the data could still be used to reveal important information about what happens to the optical properties of these glasses as the temperature is increased. This information is germane to our thermal lensing measurements.

Before proceeding to the temperature-dependent absorption measurements in these glasses, we will try to ascertain the cause of their visible absorption. The color of the glasses ranged from yellow for L32 to light-brown for L62. This coloration has been attributed to scattering due to the formation of microcrystals of SiO_2 in the glass by Cohen *et al.*⁶⁷ However, Weyl *et al.*⁶⁸ have pointed out that silicate, borate and phosphate glasses with high PbO content can be made that are transparent in the visible. The reason for this behavior, they suggested, was that Pb^{2+} formed highly symmetrical polyhedra in these glasses. The Pb^{2+} that is present in red or yellow PbO is in the form of a dipole $[\text{Pb}^{4+}(2e^-)]^{2+}$ which causes an asymmetric environment around the Pb^{2+} by the oxygen ions. This asymmetric environment is responsible for the color of PbO. When the Pb^{2+} is moved to a symmetric environment, as in a high quality glass, the color vanishes, and the glass becomes clear. However, if the glass is not of high quality, then distorted polyhedra are formed which causes visible absorption. That is, the environment around Pb^{2+} is no longer symmetric.

The room-temperature absorption coefficients α (cm^{-1}) for the glasses are shown in Fig. IV.7. Note that the absorption-edge shifts toward the visible as the PbO concentration is increased. This shift in the optical absorption has been observed by other researchers in lead silicate glasses.⁷⁰⁻⁷³ In light of the conclusions of Weyl *et al.*, it appears that the environment around the Pb^{2+} becomes more asymmetric as PbO is increased. Thus, the absorption shifts toward the visible.

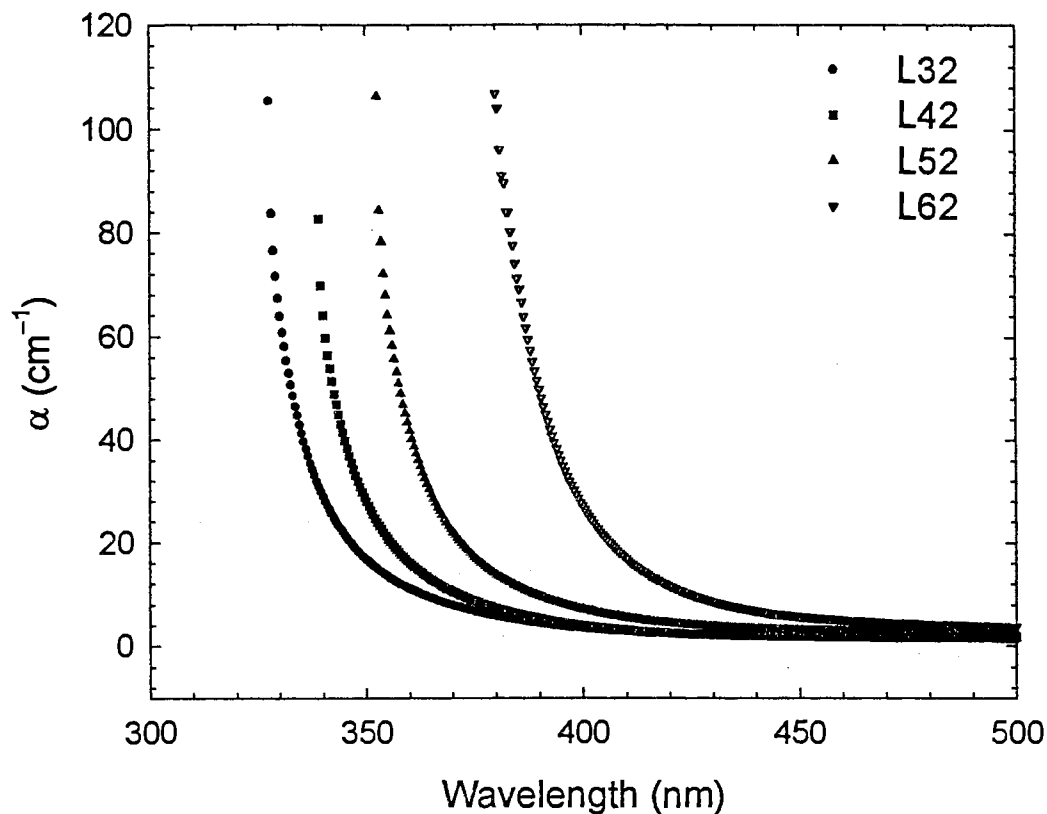


Figure IV. 7 The absorption coefficients of lead silicate glasses.

We will briefly review the findings of Ellis *et al.*⁵⁹ who performed experimental and theoretical investigations of the electronic absorption of lead silicate glasses. Fused quartz shows no absorption for energies below 9 eV (138 nm). However, when PbO is added to it, three strong new bands appear in the low-energy end of the spectrum. The intensity of these bands increase with PbO concentration and are located at 6.7 eV (185 nm), 5.3 eV (234 nm) and 4.2-4.6 eV (295-270 nm). There are other absorption bands that occur above 9 eV, but Ellis *et al.* have shown that their contribution to the visible index of refraction is far less than the bands below 9 eV.

Ellis *et al.* calculated band structures, and joint density of states for crystalline PbO and a lead silicate glass model. For the glass, they found that the top of the valence band is primarily of lead and oxygen origin, and the bottom of the conduction band is made up mostly of Pb 6*p* states. Thus, the lowest energy transitions are associated mainly with lead orbitals. Upon comparing the joint density of states for PbO and the lead silicate glass model with the observed absorption spectra, they concluded that the low-energy absorption in these glasses are mainly due to Pb 6*s* → Pb 6*p* transitions which involves two electrons. There is also some contribution from the oxygen lone pair O 2*p* → Pb 6*p*.

The observed upward curvature in our absorption spectra is likely due to tail end of the band occurring at 4.2-4.6 eV and thus originate from the transitions described in the previous paragraph. This tailing effect is observed in semiconductors and glasses and has been successfully described by Urbach's rule. The rule prescribes the absorption coefficient to follow $\alpha = \alpha_0 \exp[-\zeta(E_g - \hbar\omega)]$ near the absorption edge, where $\zeta \sim 1/k_B T$, and E_g is the optical band-gap energy.⁷¹ Although our absorption curves appear to follow an exponential trend, they do not follow the simple Urbach's rule. Apart from the fact that an optical band-gap in an amorphous system is not well-defined, the band tailing was too wide for the rule to satisfactorily fit our spectrum.

The temperature-dependent absorption spectra of the glasses are shown in Fig. IV.8. For each sample, the absorption curve clearly shifts to the visible with increasing temperature. We were able to reproduce each scan regardless of how the temperature was varied. Such reversibility and shifts in absorption have also been observed by McSwain *et al.*⁷² for alkali-silicate glasses. In order to make some quantitative statements about this temperature effect, we define a UV

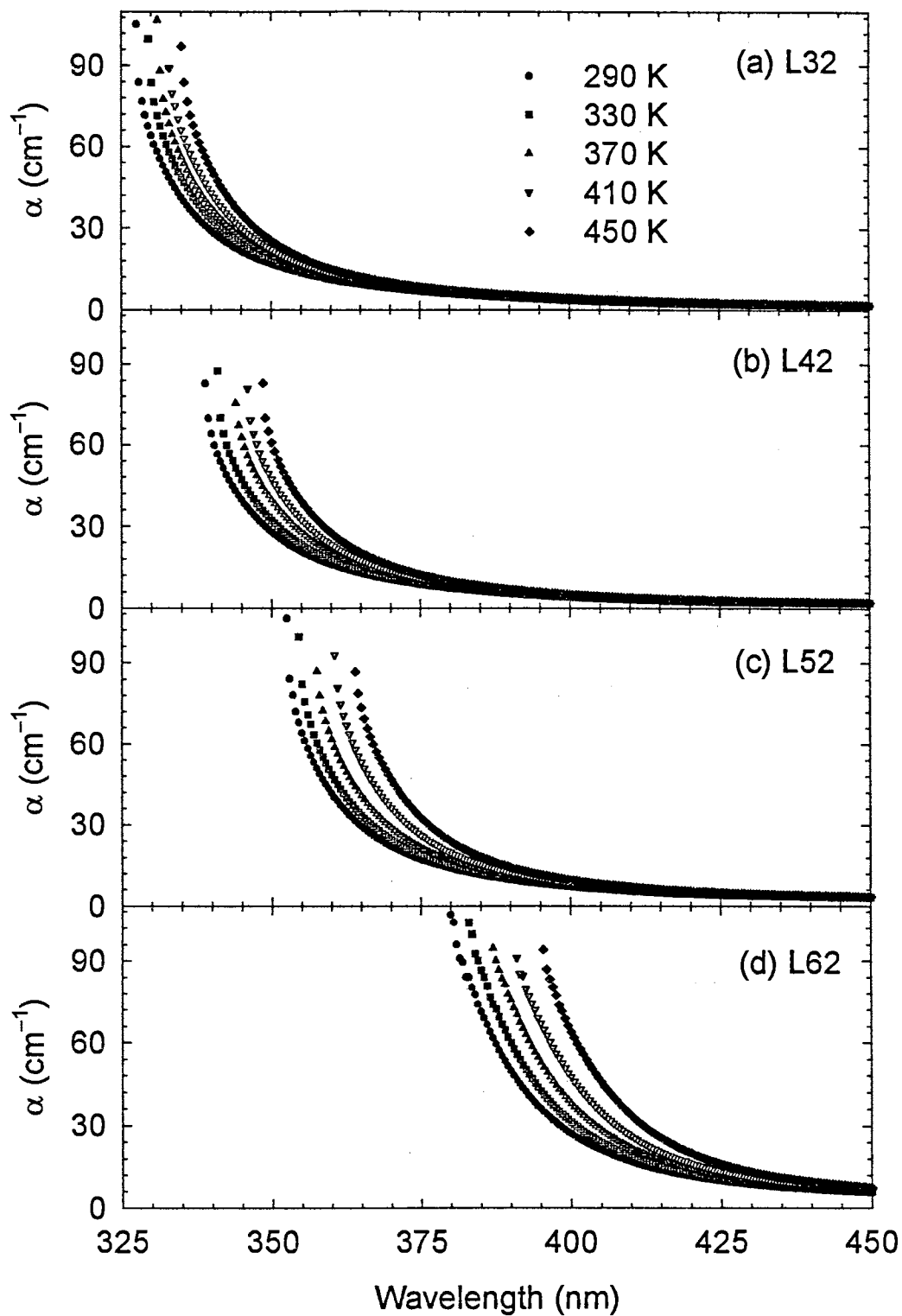


Figure IV.8 Temperature-dependent absorption measurements for L32 to L62.

cutoff wavelength λ_c as the point where the transmission of a 1 mm thick sample drops to 1%. This is an arbitrary definition, but as long as we are consistent, it provides a means for comparison among the glasses. Fig. IV.9 shows that λ_c increases with temperature linearly and also that the *slopes* of the lines increases from L32 to L62. The magnitude of the slope is a measure of how strong the temperature effect is. We will loosely interpret λ_c as the “optical band-gap” E_0 . The values of λ_c , E_0 , and the slope $d\lambda_c/dT$ are given in Table. IV.8. Thus, we may conclude that temperature affects the optical properties of the lead silicate glasses more as the PbO concentration increases.

According to Weyl *et al.*, the increase in temperature causes a fluctuation in the symmetry around the Pb^{2+} and renders the glasses less transparent. In our opinion, the thermal energy that is supplied to the samples increases the wavefunction overlap among the electronic states and thus reduces the “optical band-gap”. This does not conflict with Weyl *et al.* We will try to put this discussion on a more mathematical basis by following the method of Prod’homme.⁷³

The refractive index n is related to the polarizability ϕ of the constituent atoms and the volume V of the material through some functional form $f(n)$. For simplicity, we will assume that all the atoms have the same ϕ . The polarizability will be allowed to be temperature-dependent because the thermal energy supplied to the glass will most likely weaken the ionic or covalent bonds. The relationship can be written as $f(n) = A\phi/V$, where A is a constant. By taking the temperature differentiation of $f(n)$, we have the following expression

$$\frac{dn}{dT} = \frac{(n^2 + 2)(n^2 - 1)}{6n} [\Phi - \beta_{ex}] \quad (\text{IV.9})$$

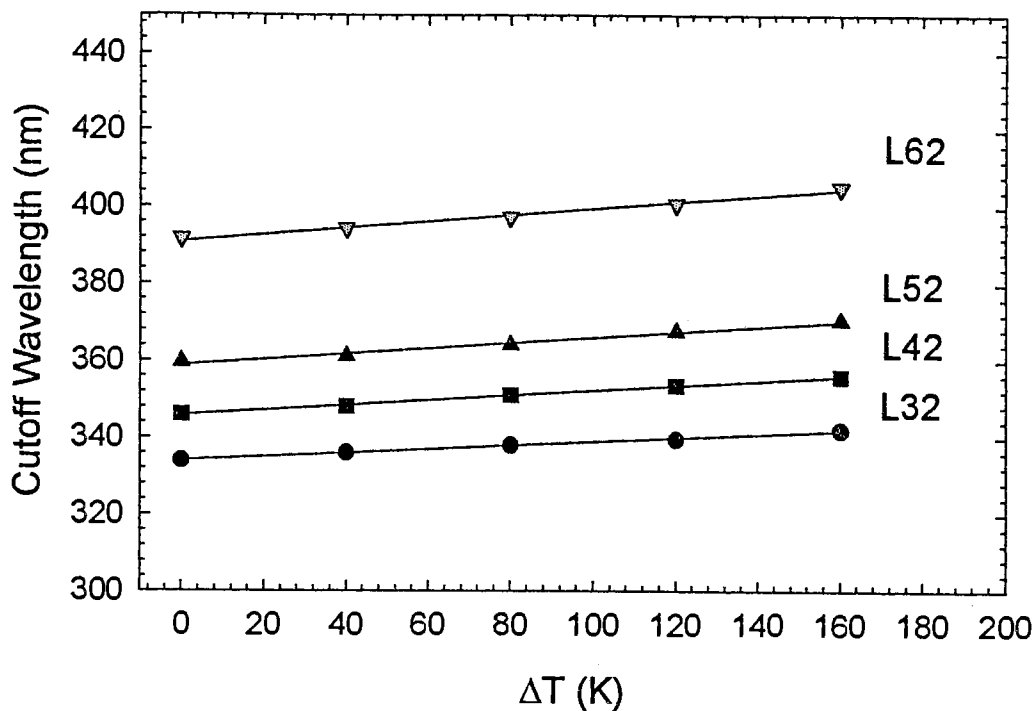


Figure IV.9. The temperature dependence of the UV cutoff wavelength for the lead silicate glasses

Table IV.8 The UV cutoff wavelength λ_c , the slope $d\lambda_c/dT$ and the corresponding "optical band-gap" E_0 for the lead silicate glasses.

Sample	λ_c (nm)	$d\lambda_c/dT$ (nm/K)	E_0 (eV)
L32	334.0	0.04875	3.712
L42	345.8	0.06375	3.585
L52	358.8	0.07125	3.455
L62	390.9	0.08375	3.171

where we have assumed a Lorentz-Lorenz type relation $f(n) = (n^2 - 1)/(n^2 + 2)$, $\Phi = (1/\phi)(d\phi/dT)$ is the fractional change in temperature derivative of the polarizability, and $\beta_{ex} = (1/V)(dV/dT)$ is the volume coefficient of expansion. Thus dn/dT depends on the relative strengths of Φ and β_{ex} . We have concluded from the thermal lensing measurements of the lead silicate glasses, that dn/dT is positive and increases with PbO concentration. This indicates that the temperature derivative of the polarizability of the glasses also increases from L32 to L62 and is greater in magnitude than the thermal expansion coefficient. This increase in the net temperature-dependent polarizability Φ is probably due to an increase in the number of lead and nonbridging oxygen ions.

If we recall that $\Delta n = (dn/dT)\Delta T$ and $\Delta\alpha = (d\alpha/dT)\Delta T$, then it is easy to see that $d\alpha/dT$ will be related to dn/dT by a Kramers-Kronig transformation given by Eq. IV.8. From Fig. IV.8, we find that $d\alpha/dT$ is positive for visible wavelengths. This is particularly obvious near the absorption-edge. Since $d\alpha/dT$ is positive, it follows that dn/dT should also be positive in agreement with our thermal lensing measurements.

(d) Intensity-scan (millisecond)

A laser beam traveling through an absorbing medium will have some of its electromagnetic energy converted into thermal energy and will, thus, increase the temperature of the medium. The heat that is generated will give rise to a temperature gradient that will follow the intensity profile of the incident beam. As we have seen in the last section, the change in the index of refraction Δn is related to the change in the temperature ΔT by $\Delta n = (dn/dT)\Delta T$, where dn/dT is the thermo-optic coefficient. Since the intensity profile of many laser beams is circular Gaussian, it follows that ΔT and, therefore, Δn will also have a circular Gaussian variation. It is easy to see that a positive dn/dT will cause a parallel incident beam to focus while a negative dn/dT will make it defocus. This kind of optical nonlinearity that results from the inhomogeneous heating of a medium by a laser beam is known as thermal lensing. The strength of thermal lensing in materials will depend mostly on the absorption coefficient since it determines the amount of energy that is absorbed.

The millisecond version of the Intensity-scan technique we have developed has proven to be a highly sensitive method for investigating thermal lensing. The data for the lead silicate glasses are shown in Fig. IV.10 where we have plotted the normalized transmission versus the input beam power at the sample. The samples were optically *thin* and imparted a positive nonlinear phase-shift to the beam. Since the samples were placed before the focus of the incoming beam ($z < 0$), the phase-shift caused the emerging beam to focus before prior to the $z = 0$ position. The $z = 0$ location is where the beam would have focused in the absence of the samples. This resulted in the observed decrease in transmission in the far-field.

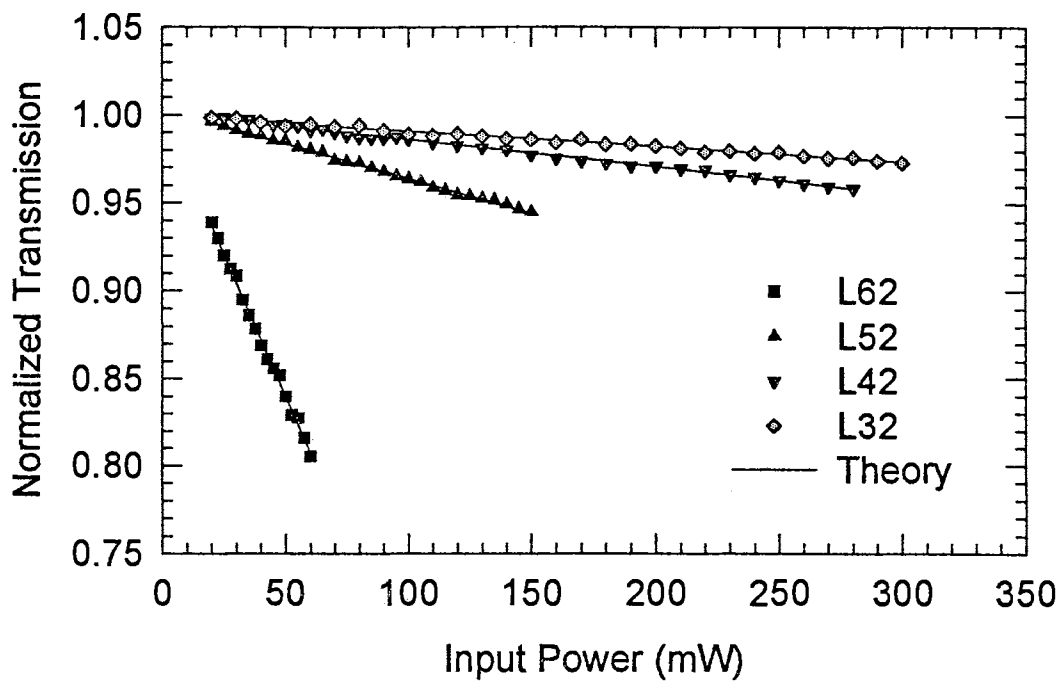


Fig. IV.10 Intensity-scan data for the lead silicate glasses.

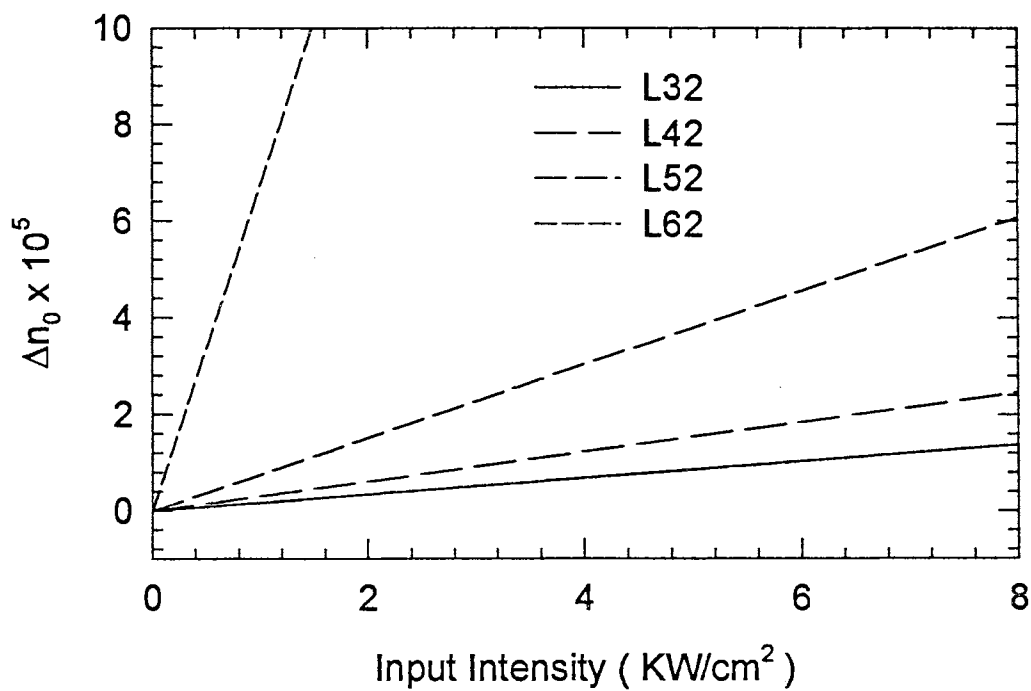


Fig. IV.11 The change in refractive index for the lead silicate glasses

Thus, from the Intensity-scan data, we can conclude that the lead silicate glasses have a positive thermal nonlinear refraction coefficient γ_{th} . As the plots show, the transmission data scales very linearly with the incident beam power verifying the circular beam limit of the Intensity-scan theory presented in Chapter II. We should reiterate that the thermal nonlinearity reaches a steady-state situation during the passage of the pulse. Thus, the Δn we measured is the steady-state value. Recall that Eq. II.45 is derived assuming a square pulse with an instantaneous nonlinearity or, equivalently, a cw laser in which the nonlinearity has reached steady-state. Therefore, Eq. II.45 can be directly used without having to perform a time-average over the pulse duration. In Fig. IV.11, we show the change in the on-axis on-focus refractive index as a function of input intensity. This range of Δn_0 is typical for glasses.

What is remarkable about the technique is that we can readily measure very small induced phase distortions. For example, the L32 sample at 20 mW has a normalized transmission value of 0.998. The change in refractive index at this power is 9.5×10^{-7} which corresponds to a phase-shift of only 0.017 rad or a wave-front distortion of about $\lambda/370$. The sensitivity of the technique could be enhanced by using a reference arm as introduced by Ma *et al.*¹² for the Z-scan technique. The reference arm is identical to the main arm of the Intensity-scan setup consisting of the focusing lens followed by the far-field aperture. This would greatly improve the signal to noise ratio.

The nonlinear refraction coefficients for the lead silicate glasses are shown in Table. IV.9 along with the effective sample thickness L_{eff} and the slope of the transmission lines. There is an overall uncertainty in γ_{th} of about 10% that arises primarily from the uncertainty in the slope calculations taken from scans at

Table IV. 9 Values of γ_{th} , L_{eff} , and transmission slopes of the lead glasses.

Sample	L_{eff} (mm)	γ_{th} (cm ² /GW)	slope ($\times 10^{-4}$ /mW)
L32	1.452	1.72	-0.8738
L42	1.442	3.07	-1.553
L52	1.494	7.59	-3.976
L62	1.373	67.7	-32.55

different points within the sample. The value of γ_{th} increases with PbO concentration. However, there is a large increase in γ_{th} from L52 to L62. This peculiar behavior of L62 having optical properties that are quite different from the other lead silicate glasses will emerge as a common theme. We have already seen this behavior with the absorption measurements in the last section.

To understand what material parameters affect Δn_0 , we will investigate their inter-relationship. We begin with the heat diffusion equation given by

$$\nabla^2 T(\mathbf{r}, t) + \frac{g(\mathbf{r}, t)}{k_{th}} = \frac{1}{D} \frac{\partial T(\mathbf{r}, t)}{\partial t} \quad \text{for } 0 < r < \infty, t > 0$$

$$T(\mathbf{r}, t) = T_0 \quad \text{for } 0 < r < \infty, t = 0. \quad (\text{IV.10})$$

Here, $T(\mathbf{r}, t)$ is the temperature at position \mathbf{r} and time t , k_{th} is the thermal conductivity (W/m°C), D is the thermal diffusivity (m²/s) and $g(\mathbf{r}, t) = \alpha I(\mathbf{r}, t)$ is the heat generation rate (W/m³). We solve the heat diffusion equation in two-dimensions neglecting heat diffusion along the z -axis, $\partial^2 T / \partial z^2 \cong 0$. In addition,

we will use cylindrical coordinates and assume a circular Gaussian beam. The above equation can be solved by using Green's functions given by

$$G(r, t; r', t') = \frac{1}{4\pi D(t-t')} \exp\left\{-\frac{|r-r'|^2}{4D(t-t')}\right\}. \quad (\text{IV.11})$$

where we now interpret r as a radial coordinate. This is the temperature distribution in the x - y plane, which is initially at $T = 0$, due to an impulsive heat source of strength unity located at r' and releasing its heat spontaneously at t' .

The temperature distribution is found to be

$$\begin{aligned} T(r, t) &= \int_0^\infty G(r, t; r', 0) T_0 2\pi r' dr' + \frac{D}{k_{th}} \int_0^t dt' \int_0^\infty G(r, t; r', t') g(r', t') 2\pi r' dr' \\ &= T_0 + \frac{P_0 \alpha}{4\pi k_{th}} \left[-Ei\left(-\frac{2r^2}{8Dt + w^2}\right) + Ei\left(-\frac{2r^2}{w^2}\right) \right] \end{aligned} \quad (\text{IV.12})$$

where Ei is the exponential integral and we have used a square pulse of power P_0 . The exponential integral can be expanded as

$$-Ei(-x) = -\xi - \ln x + x - \frac{1}{4}x^2 + O(x^3) \quad (\text{IV.13})$$

where $\xi \cong 0.5772$ is known as Euler's constant. Thus the change in temperature can be written in the parabolic approximation as

$$\Delta T(r, t) \cong \frac{P_0 \alpha}{4\pi k_{th}} \left\{ \ln(1 + t/2t_c) - \frac{2r^2}{w^2} \left(\frac{t/2t_c}{1 + t/2t_c} \right) \right\} \quad (\text{IV.14})$$

However, we are interested in the on-axis change in the index of refraction and can set $r = 0$. The on-axis change in refractive index is then given by

$$\Delta n(0, t) = \frac{dn}{dT} \Delta T(0, t) = \frac{P_0 \alpha}{4\pi k_{th}} \frac{dn}{dT} \ln(1 + t/2t_c) \quad (\text{IV.15})$$

The above equation has been shown to accurately predict the thermal lensing behavior of millisecond pulses in glasses by St. John *et al.*⁶ The only disadvan-

tage of Eq. IV.15 is that it is not applicable to cw lasers because as t goes to infinity, so does ΔT . We find that the linear absorption coefficient and thermal conductivity will compete with one another to raise Δn . If k_{th} is small, then there will be significant heat localization which will tend to increase Δn . If α is large, then more of the beam's energy will be absorbed leading to a rise in temperature and again increase Δn . To maximize Δn , it is desirable to have a small k_{th} , a large α , and a large dn/dT .

In light of the above discussion, it seems clear that the much larger Δn exhibited by L62 is caused by a larger α , a larger dn/dT and a smaller k_{th} when compared to the other samples. We know that the absorption coefficient of L62 is about twice as large as that of L52. Unfortunately, we do not know the conductivity values nor the thermo-optic coefficients of these specific glasses. It seems reasonable from the structural studies made on similar glasses, that the thermal conductivity of L62 will be considerably less than that of the other samples due to its weaker structure. It also seems likely, that the thermo-optic coefficient of L62 will be considerably higher than the other samples because of the larger number of polarizable entities such as lead and oxygen ions. If k_{th} for L62 is half as large as that of L52, and also if dn/dT for L62 is twice as large as that of L52, then the difference between γ_{th} for these two samples can be understood.

Since dn/dT will invariably contain stress components, it would be interesting to see how stress affects the thermal lensing behavior of the lead silicate glasses. We will derive an expression for dn/dT that explicitly contains all the stress components. Consider the refractive index to be a function of density and temperature $n = n(\rho, T)$. The variation in n can be written as

$$dn = (\partial n / \partial \rho)_T d\rho + (\partial n / \partial T)_\rho dT. \quad (\text{IV.16})$$

In terms of the volume expansion coefficient β_{ex} and the density derivative of the refractive index $\rho(dn/d\rho) = (p_{11} + 2p_{12})n^3/6$, we can write dn/dT as

$$\frac{dn}{dT} = \left(\frac{\partial n}{\partial T}\right)_\rho - \frac{\beta_{ex}n^3(p_{11} + 2p_{12})}{6}. \quad (\text{IV.17})$$

The above thermo-optic coefficient is due to the homogeneous heating of the medium and has been previously derived by Sparks.⁷⁴ The first term in Eq. IV.17 can be positive if the absorption of the medium shifts with temperature such that Δn increases. The second term is always negative because $d\rho/dT$ is negative. Notice that there are stress components present in Eq. IV.17. This can be understood from the fact that heating the medium will change its volume and hence its dielectric constant and, thus, can be related to the photoelastic effect. The values of dn/dT that are most often reported in the literature is given by Eq. IV.17.

Now consider the effects of inhomogeneous heating. Let us take a cylindrical region of the medium with radius R and having a temperature gradient $T(r)$. A small variation in the density $\delta\rho(r)$ is given by

$$\begin{aligned} \frac{\delta\rho(r)}{\rho} &= -\frac{\beta_{ex}}{3} \frac{1+\nu}{1-\nu} \left\{ \delta T(r) + \frac{4(1-2\nu)}{(1+\nu)R^2} \int_0^R \delta T(r)r dr \right\} \\ &\cong -\frac{\beta_{ex}}{3} \frac{1+\nu}{1-\nu} \delta T(r) \quad \text{for } r \ll R \end{aligned} \quad (\text{IV.18})$$

where ν is Poisson's ratio.⁷⁵ Therefore, from Eq. IV.16, we can write

$$\begin{aligned} \frac{dn}{dT} &= \left(\frac{\partial n}{\partial T}\right)_\rho - \frac{\beta_{ex}n^3(p_{11} + 2p_{12})}{18} \frac{1+\nu}{1-\nu} \\ &= \left(\frac{dn}{dT}\right)_{\sigma=0} + \left(\frac{dn}{dT}\right)_{\sigma \neq 0} \end{aligned} \quad (\text{IV.19})$$

The first expression for dn/dT in Eq. IV.19 is due to inhomogeneous heating of the medium which is typical of laser-induced thermal lensing.⁷⁶ In the second expression, we split up dn/dT to reflect the effects of laser beam induced stress σ . The dn/dT with $\sigma = 0$ is due to homogeneous heating (the conventional value) and is given by Eq. IV.17. The dn/dT with $\sigma \neq 0$ is solely due to laser-induced stress and is described by

$$\left(\frac{dn}{dT}\right)_{\sigma \neq 0} = \frac{\beta_{ex} n^3 (p_{11} + 2p_{12})}{9} \frac{1 - 2\nu}{1 - \nu}. \quad (\text{IV.20})$$

The contributions of the stress components to the conventional value of dn/dT are shown in Table IV.10. The β_{ex} values were derived from Ref [77]. We clearly see that this contribution increases with PbO concentration. This result is not unexpected since we have shown that the lead glasses more easily strained with increasing PbO content.

Table IV. 10 Values of β_{ex} and $(dn/dT)_{\sigma \neq 0}$ for the lead glasses.

Sample	$\beta_{ex} (\times 10^6 / ^\circ\text{C})$	$(dn/dT)_{\sigma \neq 0} (\times 10^6 / ^\circ\text{C})$
L32	19	5.3
L42	24	9.5
L52	30	12
L62	35	16

(e) Z-scan and Optical Limiting

We have investigated the nonlinear properties of the lead silicate glasses on a nanosecond time scale by performing Z-scan/Optical Limiting experiments. By studying the relative self-focusing behavior of the glasses, we could determine what material characteristics are most important to the nonlinear properties. The nonlinear refraction coefficient γ found in glasses has contributions from electronic, nuclear, electrostrictive and thermal effects. The electronic or Kerr effect is due to the nonlinear deformation of the electron clouds of the constituent atoms and has a nearly instantaneous response time. The nuclear effect is due to the change in the motions of the nuclei that are induced by the optical field and has a response time on the order of nuclear motions which is about a picosecond. The electrostrictive effect is caused by the change in the refractive index due to strains induced in the material by the electric field of the laser. The thermal effect is due to the refractive index variation caused by local heating that arises from the finite absorption of laser radiation. Both the electrostriction and thermal effects have a response time $t = r/v$ that depends on the sound velocity v and beam diameter r . On a nanosecond time-scale, it is possible to have all four of the above nonlinear effects present in a glass. It was believed that in this time-scale, the thermal effect was the dominant mechanism in glasses containing heavy-metal atoms such as lead silicate glasses.^{6,7} We will try to explore what processes contribute to the nonlinear refraction coefficient in our glasses.

We performed measurements on a 1 mm and a 1.5 mm thick sample for each lead silicate glass in order to study the effects of sample thicknesses on the optical limiting behavior of the glasses. By noting the optical limiting clamping values, we could assess the usefulness of these materials for protective devices. The position of the sample relative to the focus of the beam in addition to the

sign of its nonlinearity is crucial in determining whether the sample will limit or enhance the radiation in a far-field detector.¹⁸ The best method of finding the optimal position of the sample for limiting the light in the far-field is by first performing a Z-scan. The Z-scan, depending on the size of the aperture and relative strengths of the nonlinear refraction and nonlinear absorption coefficients, will generally show a peak and a valley. The optimal sample position for performing an Optical Limiting experiment is then the Z-scan valley. This method of carrying out a Z-scan followed by an Optical Limiting experiment is the preferred choice in determining the optical limiting characteristics of a material.^{6,7,18}

A representative Z-scan and Optical Limiting data are shown in Fig. IV.12 for the 1mm thick sample and Fig. IV.13 the 1.5 mm thick sample for L62. The Z-scans were done with an input energy of 10.1 μJ and 7.7 μJ for the 1 mm and 1.5 mm thick samples, respectively, within an uncertainty of about 10%. The solid line is an application of the elliptical Gaussian beam Z-scan theory that we developed and presented in Chapter II. The agreement between theory and experiment is quite good considering the fact that the theory assumed a 100% elliptical Gaussian beam where as the actual beam was about 85-90% elliptical Gaussian. Only near the slopes of the valley of the Z-scan does the theoretical line not match the experimental data points very well for either the 1 mm or the 1.5 mm samples. This is most likely a consequence of the parabolic approximation which can be verified by comparing the wave-optics Z-scan results with that of the Gaussian beam-optics for a circular Gaussian beam.¹⁸ The theoretical fit of the Optical Limiting data is better than that of the Z-scan. The nonlinear parameters used to fit the data for L62 as shown in Fig. IV.12 and Fig. IV.13 are $\gamma = 4 \times 10^{-6} \text{ GW/cm}^2$ and $\beta = 14 \text{ cm/GW}$ which are in good agreement with Hagan *et al.*⁷⁸ It is interesting to note that the theory correctly predicts the broadening

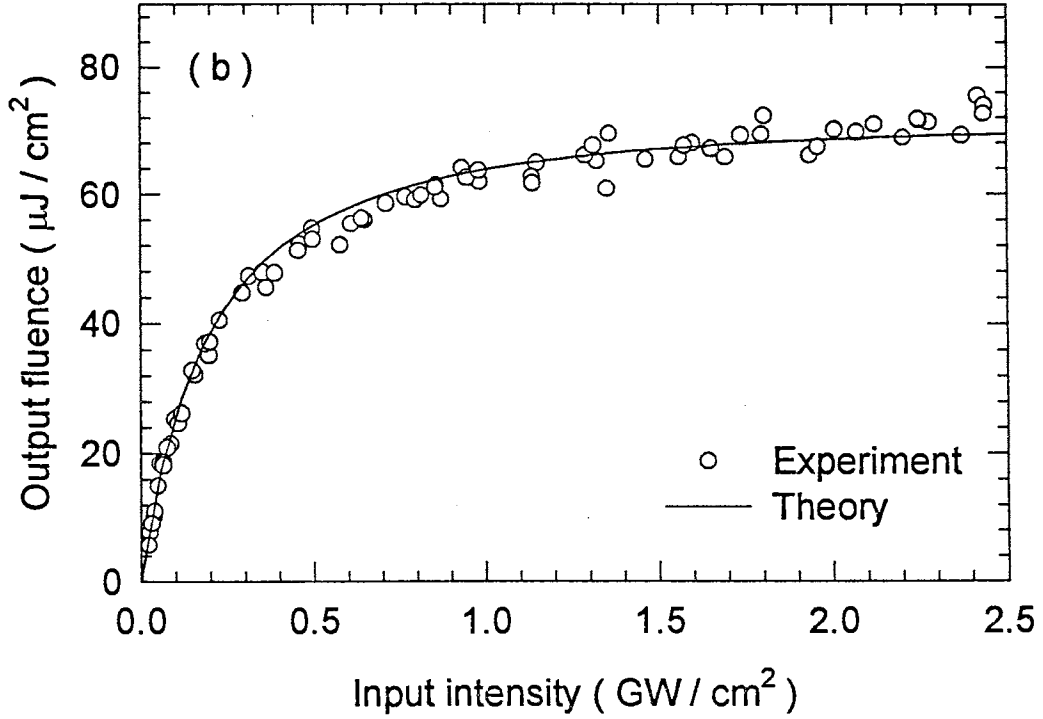
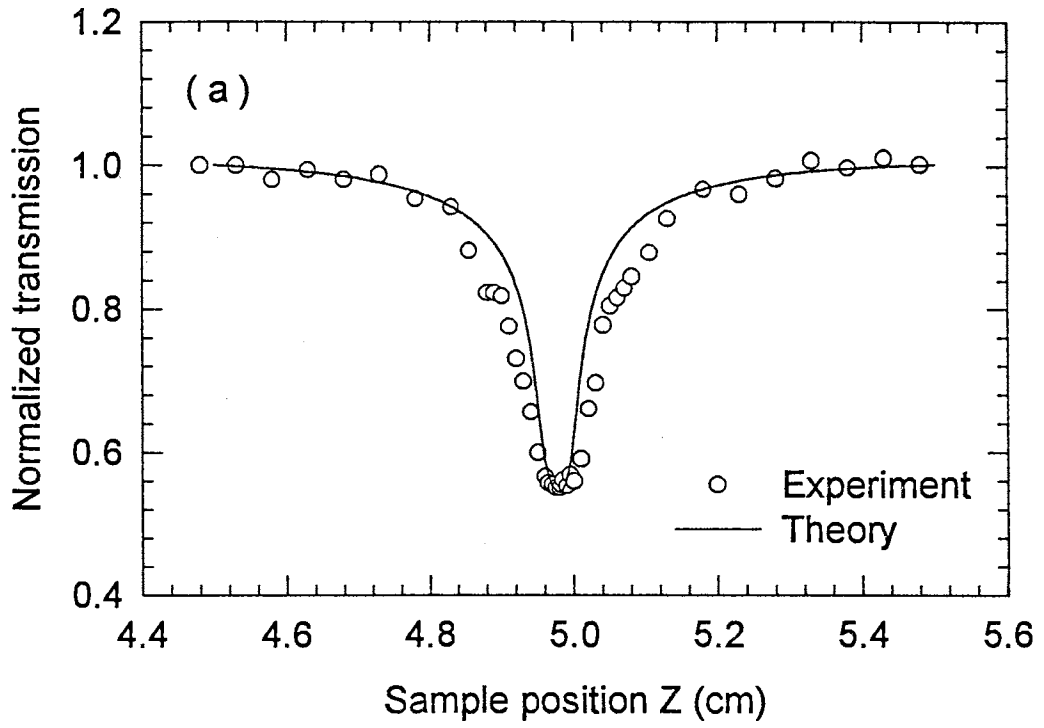


Figure IV.12 Z-scan/Optical Limiting data for L62 using a 1 mm thick sample.

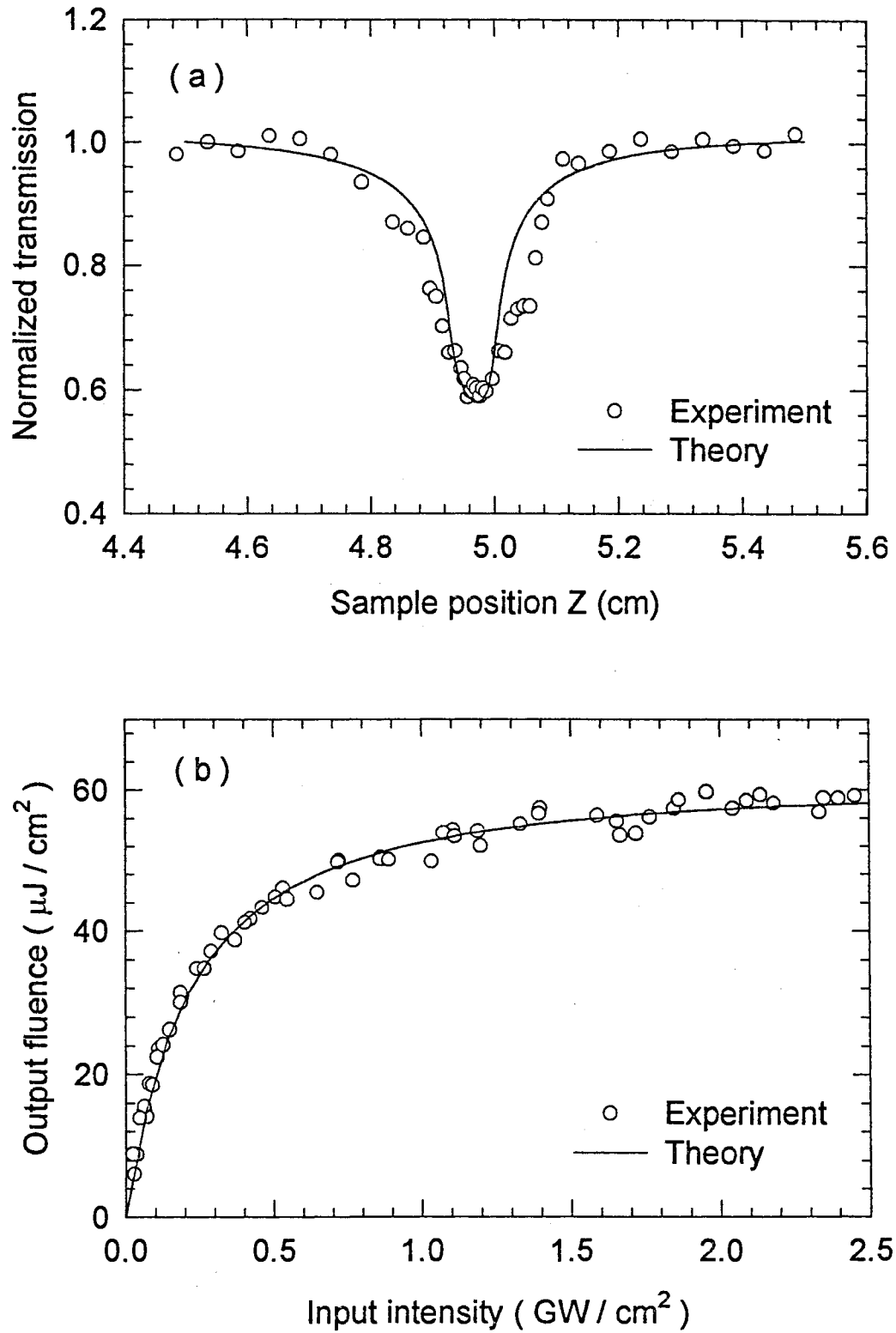


Figure IV.13 Z-scan/Optical Limiting data for L62 using a 1.5 mm thick sample.

of the valley in the Z-scan for the 1.5 mm thick sample which is attributed to the enhanced nonlinearity due to an increase in sample thickness.

Four different sets of data were available for each glass sample, two Z-scan and two Optical Limiting. Each Z-scan and Optical Limiting run was repeated several times and found to be reproducible. The Optical Limiting data for the two sample thicknesses show a difference in the clamping value. The 1 mm and 1.5 mm thick samples clamp at about $70 \mu\text{J}/\text{cm}^2$ and $60 \mu\text{J}/\text{cm}^2$, respectively. This difference in clamping value is easily understood by sectioning a sample into many slices and interpreting the enhanced nonlinear behavior as a cascading effect. That is, each slice focuses the incoming beam more within the sample than the previous slice, and the nonlinearity amplifies. Since the 1.5 mm thick sample can be sectioned more than the 1 mm thick sample, assuming equal section lengths for both sample, it is easy to see that the 1.5 mm thick sample will limit more light than the 1 mm thick sample.

The presence of a deep valley and the absence of the any peaks in the observed Z-scan can be explained as follows. The deep valley of the Z-scan is indicative of a strong nonlinear absorption coefficient. The circular aperture was set for 90% transmission of the elliptic beam which essentially means that the elongated ends of the beam was clipped. Recall, that the ratio of the semi-major to semi-minor axis was about six. Therefore, the setup was more sensitive to nonlinear absorption than nonlinear refraction since we nearly had an open aperture, and so no peaks were observed.

We simultaneously fitted the four sets of data that were available for each sample to obtain the nonlinear refraction and nonlinear absorption coefficients. Nonlinear absorption played the strongest role in fitting the theory with experiments for both the Z-scan and Optical Limiting. Nonlinear refraction played a

more involved role in the Optical Limiting data fitting than the Z-scan data in that it affected the clamping value and the curvature of optical limiting. We could thus better isolate the γ values by studying the optical limiting curves than would have been possible by studying the Z-scan data alone. The fact that the same set of nonlinear parameters fitted the data for both the 1 mm and 1.5 mm thick samples, as shown in Fig. IV.12 and Fig. IV.13, suggested that they are reasonable values for these samples.

The Optical Limiting data for all the glasses are shown in Fig. IV.14 for both the 1 mm and 1.5 mm thick samples. The clamping value is seen to rise as the PbO concentration falls. That is, the glasses with larger PbO content exhibit stronger nonlinear behavior. We should reiterate that the samples were carefully translated after each laser shot such that subsequent shots fell on undamaged material. The damage threshold was seen to rise with decreasing PbO concentration which is to be expected because the glass structure becomes weaker as the PbO content is raised. Interestingly, all the damage spots were elliptic shaped but the semi-major and semi-minor axis were flipped. This is understandable due to the fact that the larger y -axis of the beam is focused by the lens more strongly than the smaller x -axis.

The nonlinear parameters derived from the Z-scan/Optical Limiting experiments are listed in Table IV.11. Both nonlinear refraction and nonlinear absorption coefficients are seen to increase with PbO concentration. The uncertainty in these values is about 25% which is typical for Z-scan experiments with pulsed lasers and stems primarily from the uncertainty in irradiance calibration. The nonlinear refraction coefficients show a modest increase with heavy metal content, in our case lead, and confirms the trend reported by previous researchers.⁷⁹ This suggests that γ is determined not so much by structural differences of

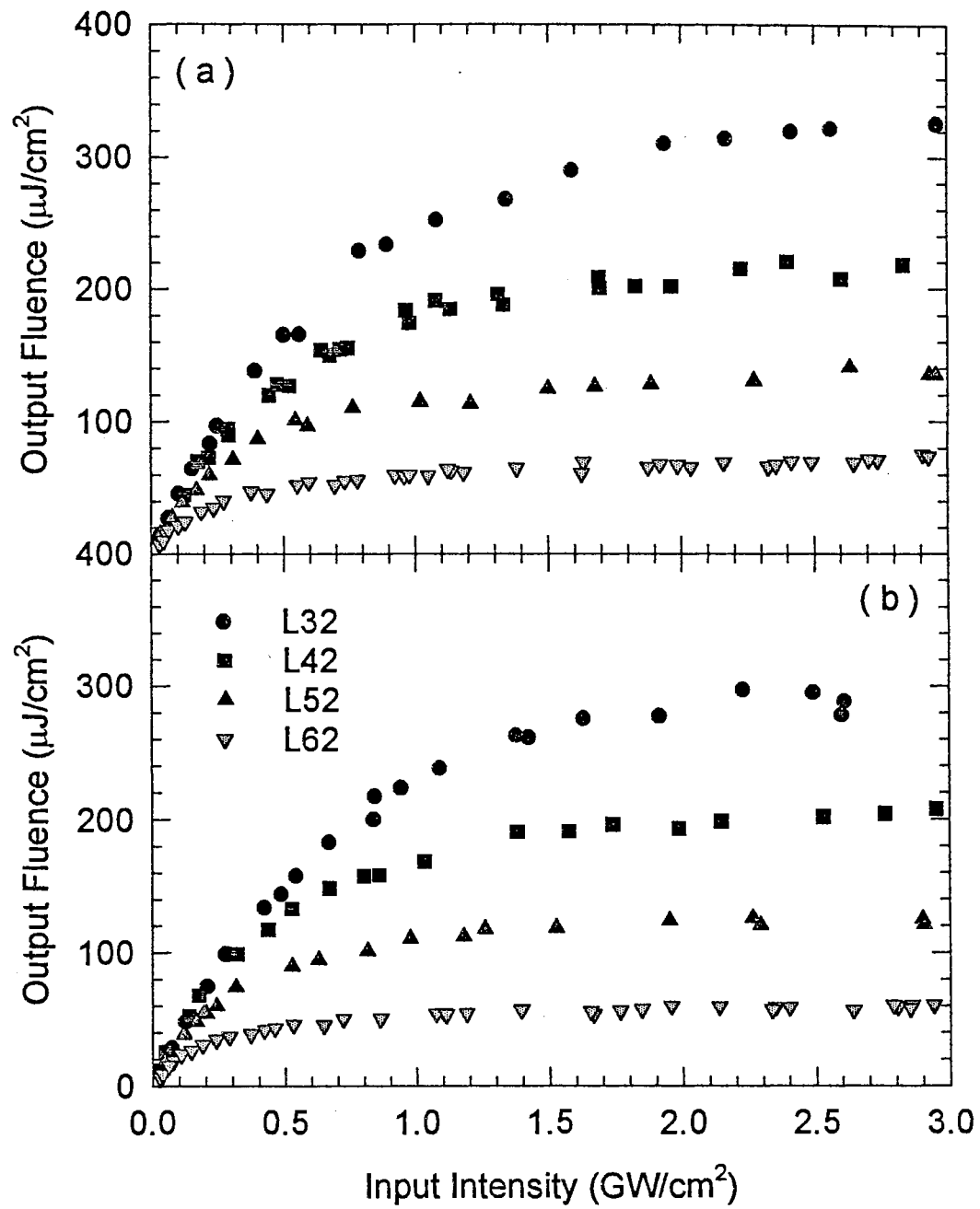


Figure IV.14 Optical Limiting data for all the lead silicate glasses. The thicknesses are (a) 1 mm thick, and (b) 1.5 mm thick.

Table IV. 11 Values of the nonlinear refraction and absorption coefficients.

Sample	γ ($\times 10^{-6} \text{cm}^2/\text{GW}$)	β (cm/GW)
L32	2.9	3.1
L42	3.2	4.6
L52	3.5	7.6
L62	4.0	14

the glasses than by the concentration of highly polarizable entities such as lead ions. In conventional silicate glasses, the network modifiers increase the number of nonbridging oxygen, which are more polarizable than the bridging oxygen, and thus there is a modest increase in the nonlinearity.⁸⁰ In lead silicate glasses, the lead enters the glass as a network former at high concentrations and a network modifier at low concentrations. Therefore, we can not solely attribute the rise in nonlinearity to the presence of nonbridging oxygen which is not expected to increase by the same amount as if lead were to enter as only a network modifier. For heavy-metal glasses, the large nonlinearity is usually attributed to the hyperpolarizability, the additional polarizability that arises due to the large electric fields of the laser, of the cations. Vogel *et al.*⁸¹ have shown that the heavy-metal cations are much more important than the oxygen anions. For the lead glasses, it is believed that the two 6s electrons in the external shell of the Pb ions are responsible for the large nonlinearity.⁸² Thus, our measurements are in agreement with the statement that large heavy-metal cations mostly determine the non-resonant nonlinearity in heavy-metal based glasses.

The large nonlinear absorption coefficients we measured have also been observed by other researchers.^{78,83} The UV absorption edges of our glasses have been shown in the temperature-dependent absorption section (See Table IV.8). There are three strong bands in the low energy spectrum of the UV absorption. The high energy bands that are present in fused quartz around 10 eV are strongly diminished as the PbO content increases.⁵⁹ The new bands due to the addition of lead are located at 6.7 eV, 5.3 eV and 4.2-4.6 eV and arose from the internal Pb $6s \rightarrow 6p$ transitions of the lead atom and the lone pair O $2p \rightarrow 6p$ transition. The incident light we used in our experiments was 460 nm or 2.7 eV. Therefore, it seems likely that the nonlinear absorption we have observed is a two-photon absorption (TPA) process to these low energy UV bands. The TPA for L62 is the largest among the these glasses. By simply adding the energy of two photons to the absorption edge we see that the incident light excites the electrons close to the 5.3 eV band. The above statement is only a possible explanation since the “optical band-gap” in glass is not well-defined as in crystals. Defining the UV absorption edge as the “optical band-gap”, although in accordance with other researchers, is arbitrary.⁷¹ We do note that the nonlinear absorption coefficient scales inversely proportional to the UV absorption-edge. However, we must also state that our experiment does not allow us to distinguish between TPA and a two-step absorption process. In TPA, the intermediate level involved in the transition is a virtual state. However, in a two-step absorption process, the intermediate level is a real state. Although there is evidence that a TPA process is at work in similar lead glasses on the nanosecond time-scale, we can not be certain which process is operating.⁷⁸ Mizrahi *et al.*⁸³ suggested that if the two-step absorption process is significant, then the nonlinear absorption will substantially decrease if the laser pulse duration is made less than the lifetime of the

intermediate state responsible for the process. There is no general theory that explains nonlinear absorption in glasses primarily because of the lack of understanding of their basic structure. There has been a theory put forward recently by Sheik-Bahae *et al.*⁸⁴ that correctly predicts the behavior of nonlinear refraction and nonlinear absorption in semiconductors. Until there is a similar theory for glasses, the explanation put forward for the nonlinear absorption in our lead silicate glasses seems reasonable.

In our experiments, an elliptical Gaussian beam was used and so the x and y directions of the beam are not affected by electrostriction or thermal effects by the same amount. For example, L32 has the highest LA phonon sound velocity among the lead glasses of about 3.85 km/s and so is expected to have a faster rise time than the other glasses. This means that the rise time of either thermal or electrostrictive effects at the focus of the x -beam is about 5 ns and for the y -beam about 1 ns. The rise times in the x and y directions will increase for the other samples because the sound velocities decrease. Since our pulse duration was 7 ns, we can conclude that thermal or electrostrictive effects have barely enough time to establish themselves. For the Z -scan experiments where the beam radii at the sample is continuously changing, thermal and electrostrictive effects will affect, at most, the data points at the center of the scan, i.e., near the focus. For the optical limiting experiment, it also does not seem likely that both effects will have sufficient time to take hold because the samples were placed several hundred microns from the geometric focus of the lens where the beam radii are larger. However, it is possible that the on-axis part of the beam may be affected by the two effects. In light of this discussion, it therefore appears unlikely that the nonlinear mechanism responsible for our observation can be attributed solely to a thermal or electrostrictive effect.

However, we can calculate the nonlinear refraction coefficient assuming that it arises from a strictly electrostrictive effect. The characteristic time for sound waves is about 100 ps. Elasto-optic effects can contribute to the self-focusing process provided that the laser pulse exists for a time longer than this characteristic time. The Brillouin scattering cross-sections must be known in order to calculate the magnitude of the nonlinearity due to electrostrictive effects. This is another reason why we performed Brillouin scattering on our glasses. Heiman *et al.*⁸⁵ have shown that the nonlinear refraction coefficient can be written in as $n_{2,es} = n^7 p_{12}^2 / 16\pi\rho v_{LA}^2$ in esu, where all the terms have their usual definitions. The SI version can be found by $\gamma_{es} = (40\pi/cn)n_{2,es}$ and are given in Table IV.12. We find that the electrostrictive contribution increases with PbO content which is expected due to the ease of straining higher PbO glasses. The contribution is also a small percent of the total nonlinear refraction coefficient. In our experiments, the contribution, if any, would be smaller.

Table IV. 12 Values of the electrostrictive nonlinear refraction coefficients.

Sample	$\gamma_{es} (\times 10^{-6} \text{cm}^2/\text{GW})$	$(\gamma_{es} / \gamma_{total}) \times 100$
L32	0.25	8.6
L42	0.39	12
L52	0.47	13
L62	0.77	19

2. Eu-doped alkali-silicate glasses

(a) Brillouin Scattering

In this section, we present the results of Brillouin scattering that have been performed on Eu-doped alkali silicate glasses that had a systematic variation of Eu_2O_3 concentration. These glasses have recently been investigated by the four-wave-mixing technique, Raman scattering, and thermal diffusivity measurements.⁸⁶ This is the first reported study of Brillouin scattering on these glasses although Brillouin scattering has been performed on similar glass systems.³⁶ Since all the error analysis discussion, correction factors, and definitions of measured quantities were included in the Brillouin scattering section for the lead glasses, we will not repeat it here.

The Brillouin shifts for these glasses along with the density and refractive index are shown in Table IV.13. The refractive index values were obtained with our modified Brewster's angle technique. However, the sample surfaces were not very well polished and lead to an uncertainty of ± 0.005 . B12 and B14 contain dual alkali and will be discussed later. We will first discuss B5-B10 that have systematic Eu variation. There appears to be a slight shift of the LA phonon towards higher energies from B5 to B10 but it is difficult to say anything conclusive about the TA shift. On the other hand, the density measurements for these glasses are interesting. It is clearly seen that the B5 sample decreases in density from 2.72 g/cm^3 to 2.41 g/cm^3 with the addition of 0.1% mole of Eu_2O_3 . This suggests that the network expands to accommodate the large Eu ions and as a result there is less mass present per unit volume. The number of Eu ions increases per unit volume as more Eu_2O_3 is added. The density is seen to increase from 2.41 g/cm^3 for B6 which has 0.1% mole of Eu_2O_3 to 2.82 g/cm^3 for B10

Table IV.13 The density, refractive index, and Brillouin shifts for the Eu-glasses.

Sample	Density (g/cm ³)	n (514.5 nm)	$\Delta\omega_{LA}$ (cm ⁻¹)	$\Delta\omega_{TA}$ (cm ⁻¹)
B5	2.72 ± 0.01	1.525 ± 0.005	0.7927 ± 0.0006	0.4742 ± 0.0005
B6	2.41 ± 0.01	1.525 ± 0.005	0.7982 ± 0.0008	0.4755 ± 0.0005
B7	2.49 ± 0.01	1.535 ± 0.005	0.7935 ± 0.0007	0.4724 ± 0.0007
B8	2.51 ± 0.01	1.535 ± 0.005	0.7976 ± 0.0007	0.4748 ± 0.0007
B9	2.58 ± 0.01	1.540 ± 0.005	0.7979 ± 0.0006	0.4736 ± 0.0005
B10	2.82 ± 0.01	1.565 ± 0.005	0.8069 ± 0.0007	0.4728 ± 0.0005
B12	2.64 ± 0.01	1.565 ± 0.005	0.8693 ± 0.0007	0.5136 ± 0.0007
B14	2.57 ± 0.01	1.555 ± 0.005	0.7867 ± 0.0002	0.4655 ± 0.0004

Table IV.14 The sound velocities, and elastic constants for the Eu-glasses.

Sample	v_{LA} (10 ⁵ cm/s)	v_{TA} (10 ⁵ cm/s)	c_{11} (10 ¹⁰ dynes/cm ²)	c_{44} (10 ¹⁰ dynes/cm ²)
B5	5.670 ± 0.126	3.392 ± 0.076	87.4 ± 4.2	31.3 ± 1.5
B6	5.708 ± 0.128	3.401 ± 0.076	78.5 ± 3.8	27.9 ± 1.4
B7	5.638 ± 0.125	3.356 ± 0.076	79.1 ± 3.8	28.0 ± 1.4
B8	5.667 ± 0.125	3.374 ± 0.077	80.6 ± 3.9	28.6 ± 1.4
B9	5.651 ± 0.124	3.354 ± 0.075	82.4 ± 3.9	29.0 ± 1.4
B10	5.623 ± 0.122	3.295 ± 0.072	89.2 ± 4.2	30.6 ± 1.4
B12	6.058 ± 0.131	3.580 ± 0.080	96.9 ± 4.6	33.8 ± 1.6
B14	5.518 ± 0.117	3.265 ± 0.071	78.3 ± 3.6	27.4 ± 1.3

which has 5% mole of Eu_2O_3 .

The sound velocity of both LA and TA phonons and corresponding elastic constants are shown in Table IV.14. Although it appears that the LA and TA sound velocities decrease slightly from B5 to B10, it is not conclusive. The elastic constants, on the other hand, show a definite density dependence from B5 to B10. This can be seen from the relationship $c = \rho v^2$, where v , in our case, does not change dramatically between samples. A plot of the Eu concentration dependence of the elastic constants is shown in Fig. IV.15. Therefore, it appears that the glass system with no Eu ions present is harder to strain applying either a compression or shear stress than it is for the same system with just a small percent (less than 5%) of Eu ions.

The Young's modulus, Bulk modulus and Poisson's ratio are presented in Table IV.15. Both the Bulk and Young's moduli show a density dependence of

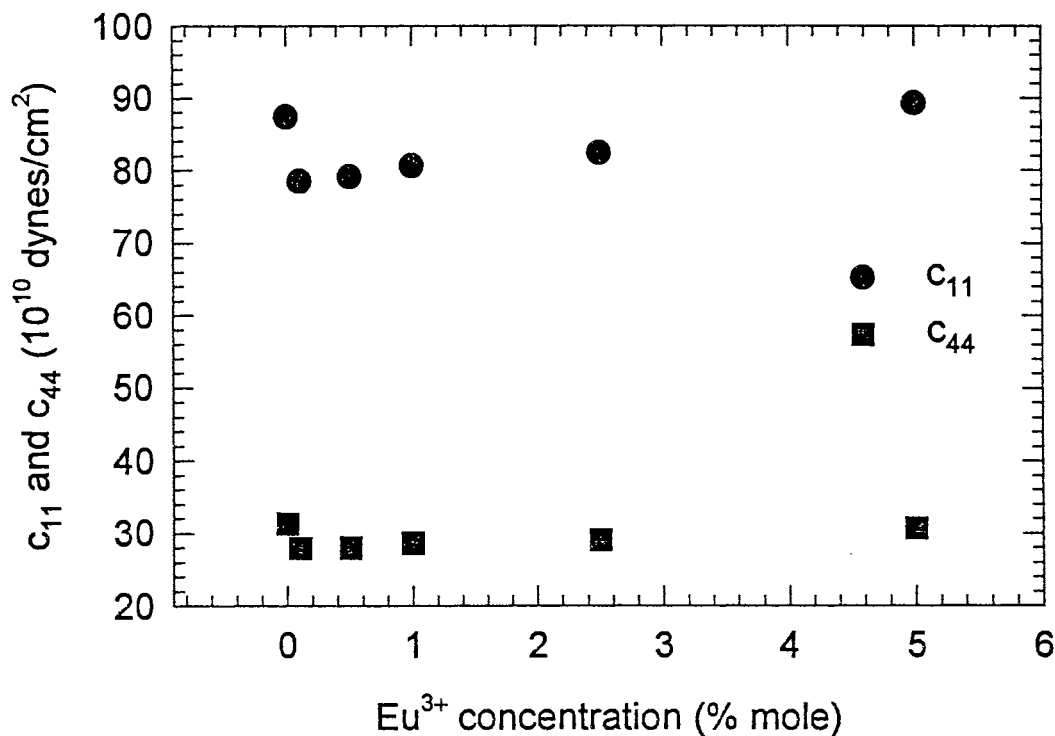


Figure IV.15. Eu concentration dependence of the elastic constants of B5 to B10.

Table IV.15 Young's modulus, Poisson's ratio, and Bulk modulus of Eu-glasses.

Sample	Poisson's ratio	Young's modulus (10^{10} dynes/cm ²)	Bulk modulus (10^{10} dynes/cm ²)
B5	0.221	38.2	45.7
B6	0.224	34.2	41.3
B7	0.226	34.3	41.8
B8	0.225	35.0	42.5
B9	0.229	35.6	43.7
B10	0.239	37.9	48.4
B12	0.232	41.6	51.8
B14	0.231	33.7	41.8

first decreasing and then gradually increasing in value as the Eu_2O_3 is increased. Recall that the density of B5 exceeds that of B9.

As we have seen in the Brillouin scattering section on lead silicate glasses, the larger the value of the Young's modulus, the more difficult it is to have the material strained by shearing stresses. Also, the larger the bulk modulus, the more difficult it is to compress the material. The Poisson's ratio increases in value from 0.221 for B5 to 0.239 for B10, indicating that the structural bonds become progressively ionic. This may be understood by the fact that the introduction of the large Eu ions in the glass network breaks more of the Si-O bonds that connects the SiO_4 tetrahedral units together, thereby creating additional nonbridging oxygen bonds. The bridging oxygen bonds are predominantly covalent bonds whereas the nonbridging oxygen bonds are more ionic in nature.

The photoelastic properties of these glasses will now be presented. The correction factors used in determining the photoelastic constants are shown in Table IV.16 and the photoelastic constants are shown in Table IV.17. We cannot conclusively say whether p_{12} shows a density dependence as expected from Carleton's model of photoelasticity. There is no clear density dependence of $|p_{44}|$ which is in agreement with what Schroeder⁶³ observed in ternary glass systems. It is interesting to note that the photoelastic properties of B5 and B6 are very similar even though there is a large difference in density. Perhaps the addition of 0.1% mole of Eu_2O_3 does not appreciably change the strain induced polarizability of the two glasses. The photoelastic constants for B5 to B10 are plotted against Eu concentration in Fig. IV.16.

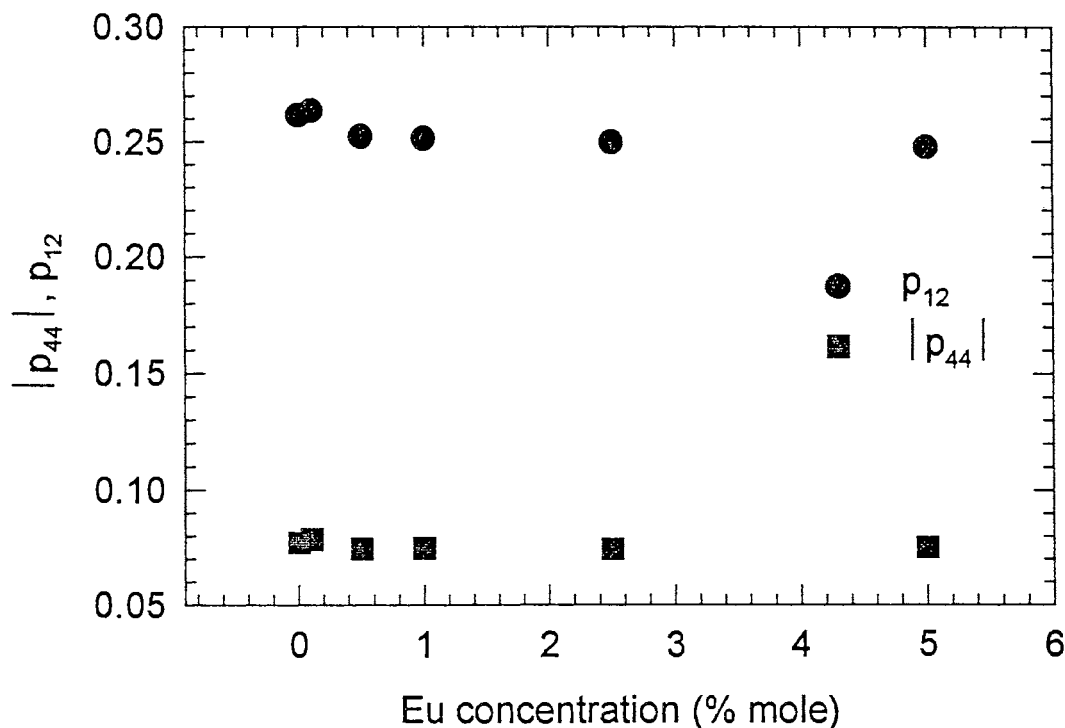


Figure IV.16. Eu concentration dependence of the photoelastic constants of B5 to B10.

Table IV.16 Correction factors for the Eu-doped alkali-silicate glasses.

Sample	ξ	Back reflection correction	Solid angle correction	Volume correction
B5	1.006	1.000	1.088	0.9992
B6	1.135	1.001	1.088	0.9992
B7	1.032	1.002	1.102	0.9991
B8	1.020	1.006	1.102	0.9991
B9	1.019	1.008	1.110	0.9991
B10	1.009	1.013	1.146	0.9988
B12	0.9587	1.001	1.146	0.9988
B14	0.9888	1.002	1.131	0.9989

Table IV.17 The photoelastic constants of the Eu-doped alkali-silicate glasses.

Sample	p_{12}	$ p_{44} $	I_{TA}/I_{LA}
B5	0.262	0.077	0.1213
B6	0.263	0.079	0.1252
B7	0.252	0.074	0.1226
B8	0.251	0.075	0.1242
B9	0.250	0.074	0.1253
B10	0.248	0.075	0.1335
B12	0.250	0.080	0.1460
B14	0.233	0.067	0.1173

Finally, we briefly discuss the results of the dual-alkali modified Eu-doped silicate glasses. The samples B12, B14, and B9 have the same 2.5% mole concentration of Eu_2O_3 but the amount of Na^+ that is in B9 is split evenly into Na^+ and Li^+ for B12, and Na^+ and K^+ for B14. The B12 sample has a density that is higher than B9. This may be understood in terms of the field produced by Li^+ . Li^+ , having the smallest ionic radius of the three alkali ions, will have a larger field than Na^+ or K^+ and will contract the network and thus increase the density of the glass. The B14 sample has a slightly lower density than B9 because the field produced by K^+ is smaller than Na^+ and will not contract the network as much. These density measurements are in agreement with those done by Gangwere *et al.*³⁶ on similar glasses.

The values of the sound velocities for both LA and TA phonons, and corresponding elastic constants for B12 and B14 show the same trend in data that was exhibited by the single alkali-modified Eu-doped silicate glasses LS and KS samples which had been investigated by Gangwere *et al.*³⁶ Namely, the Li samples (B12, LS) showed higher values of these properties than the K samples (B14, KS). For example, the elastic constants for LS were $c_{11} = 103.5$ and $c_{44} = 35.3$ and for KS were $c_{11} = 81.0$ and $c_{44} = 26.7$, all in 10^{10} dynes/cm². This trend has been attributed to the increase in alkali-oxygen bond length in going from Li to K due to the decrease in the field strength of the alkali ion.³⁶

The photoelastic constants of B12 are larger than B14. This is opposite to the trend that is displayed by LS and KS. It seems plausible that the presence of two alkali modifies the strain induced polarizability in a manner that is different from the presence of one alkali. However, more systematic studies of mixed alkali ions in such rare-earth doped silicate glasses need to be done before a coherent picture can be put forward.

(b) Intensity-scan (nanosecond)

In this section, we present the results of the nanosecond Intensity-scan measurements on the Eu-doped alkali-silicate glasses that had a systematic Eu^{3+} concentration variation. The theory and experimental parts of the technique have been presented in Chapters II and III. The procedure of deriving the nonlinear refraction coefficient from the data was done by comparing slopes of the Intensity-scan plots of our samples to that of a standard sample, which in our case was fused quartz. We used the accepted value of $\gamma = 2.5 \times 10^{-7} \text{ cm}^2/\text{GW}$ for the nonlinear refraction coefficient for fused quartz.⁸² The nonlinear refraction coefficients for the glasses are shown in Table IV.18.

A representative Intensity-scan plot is shown for B10 in Fig. IV.17. The samples were placed after the focus of the lens. The rise in transmission shown in the closed aperture Intensity-scan of Fig. IV.17a clearly indicates that the sample collimates the beam in the far-field and thus exhibits a positive nonlinear behavior. In the open aperture Intensity-scan shown in Fig. IV.17b, we failed to detect any nonlinear absorption for the range of intensities used. We always worked below the damage threshold of the glasses and did not use higher intensities for fear of damaging the samples. It may be possible that nonlinear absorption occurs at higher intensities and/or different wavelengths than the ones we used.

The nonlinear absorptive processes in glasses are not well understood. The lack of long-range periodicity in glasses means that we cannot meaningfully apply the band-gap explanation for nonlinear absorption that exists for semiconductors.⁸⁴ In addition, we do not know what electronic states would take part, if any, in the nonlinear absorption process in these modified alkali-silicate glasses. Therefore, we will not discuss nonlinear absorption any further and will try to understand the behavior of the nonlinear refraction coefficient.

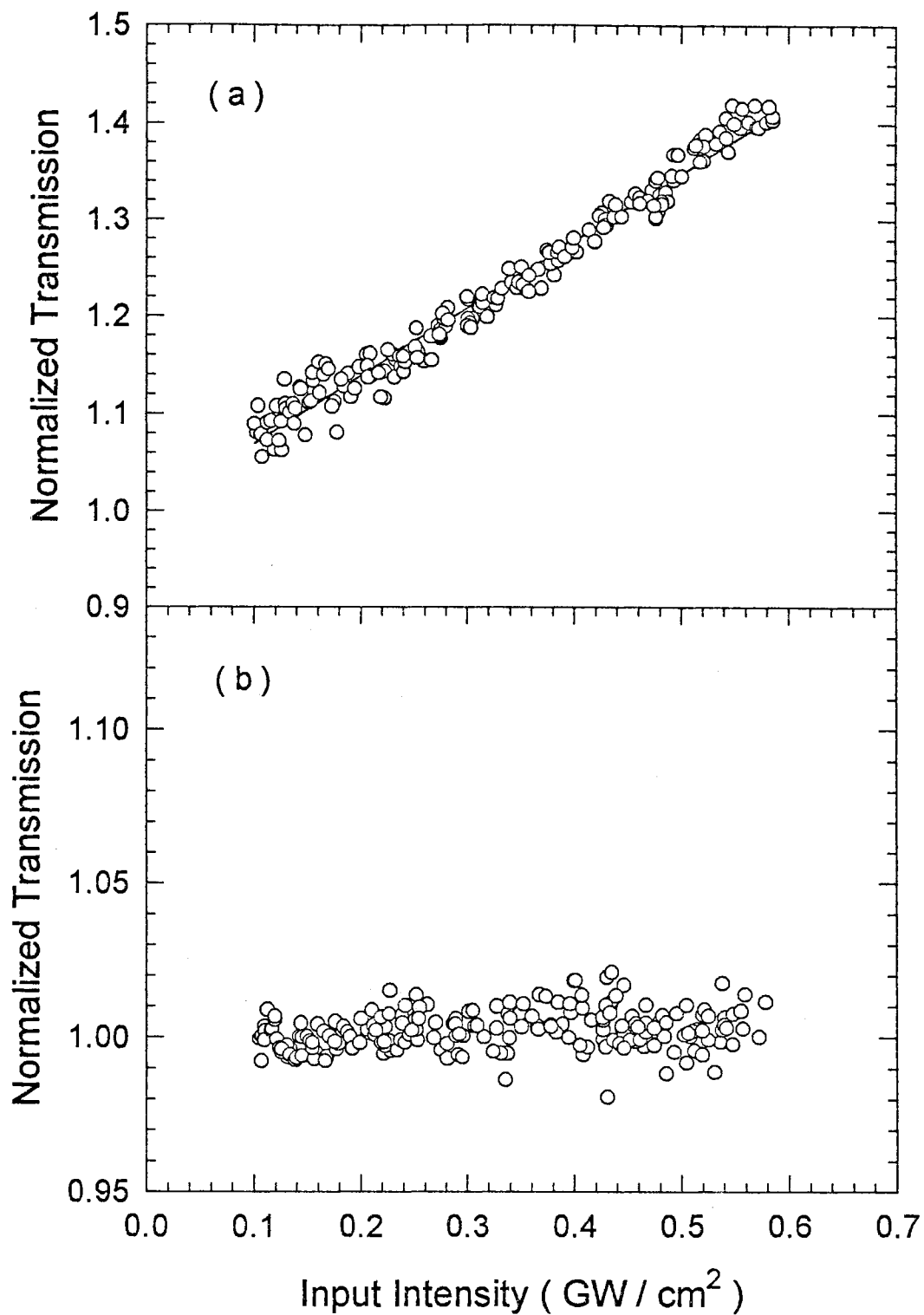


Figure IV.17 Intensity-scan data for B10. (a) closed-aperture, and (b) open-aperture. $\gamma = 21 \times 10^{-7} \text{ cm}^2/\text{GW}$.

Table IV.18 Nonlinear refraction coefficient, ratio of slopes and density values of the Eu-doped alkali-silicate glasses.

Samples	$\frac{\text{Slope}_{\text{Quartz}}}{\text{Slope}_{\text{Sample}}}$	γ (10^{-7} cm ² /GW)	Density (g/cm ³)
B5	0.63	6.4	2.72
B6	0.61	5.7	2.41
B7	0.45	6.2	2.49
B8	0.32	6.5	2.51
B9	0.28	7.6	2.58
B10	0.11	21	2.82
B12	0.29	15	2.64
B14	0.21	15	2.57
SiO ₂	1.0	2.5	2.207

As mentioned in the last section, density measurements indicate that the addition of Eu³⁺ in these glasses expands the undoped network to accommodate the large Eu ions. The γ values of all the samples are listed in Table IV.18 and have an uncertainty of about 20% that arises primarily from irradiance calibration and uncertainty in the measured slopes. We see that the value of the nonlinear refraction coefficient first decreases from 6.4×10^{-7} cm²/GW for B5, which has no Eu³⁺, to 5.7×10^{-7} cm²/GW for B6, which has only 0.1% mole of Eu₂O₃. The nonlinear refraction coefficient then begins to rise and reaches its highest value of 21×10^{-7} cm²/GW for the 5% mole of Eu₂O₃ sample B10. The nonlinear refraction coefficient is plotted as a function of Eu₂O₃ concentration in Fig. IV.18 where we

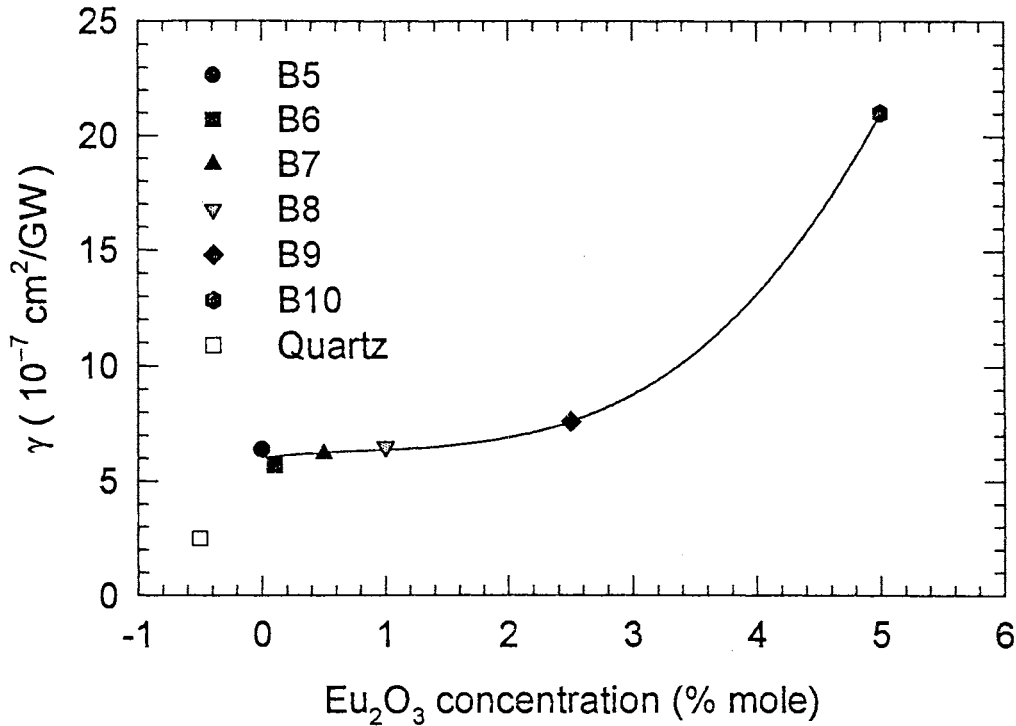


Figure IV.18 Plot of the nonlinear refraction coefficient for B5 through B10 and also showing fused quartz. The line is a guide for the eye.

see that there is almost a three-fold increase in γ value from B9 to B10, with a difference of 2.5% mole of Eu_2O_3 between the samples. We will try to understand this behavior in terms of what we believe is happening on a microscopic level.

We will first derive an expression for the nonlinear refraction coefficient based on a semiclassical model of the simple harmonic oscillator due to Boling *et al.*⁸⁷ The assumption is made that a transparent dielectric can be adequately described by a solid made of atomic or molecular constituents and that each constituent exhibits a linear electronic polarizability $\alpha^{(1)}$ and an electronic hyperpolarizability $\alpha^{(3)}$. The microscopic polarizability $p_i(t)$ induced in the i th constituent by an incident light wave $E_0 \cos \omega t$ is given by

$$p_i(t) = \alpha_i^{(1)} E_0 \cos \omega t + \frac{1}{6} \alpha_i^{(3)} (E_0 \cos \omega t)^3. \quad (\text{IV.21})$$

The macroscopic polarization P is taken to be the sum of the microscopic polarization by $P = \sum_i N_i p_i$, where N_i is the number density of the i th constituent.

By approximating the local field correction with the Lorentz function $(n^2 + 2)/3$, Boling *et al.*⁸⁷ expressed the third-order nonlinear susceptibility as

$$\chi_{1111}^{(3)}(-\omega:\omega, \omega, -\omega) = \frac{1}{24} \left(\frac{n^2 + 2}{3} \right)^4 \sum_i N_i \alpha_i^{(3)}(\omega). \quad (\text{IV.22})$$

Thus, we can see that the nonlinear refraction coefficient will depend on the hyperpolarizability and the number density of each constituent.

Nasu *et al.*⁸⁰ have shown that the nonbridging oxygen has a larger $\alpha^{(3)}$ than a bridging oxygen. They were able to derive the hyperpolarizabilities of the following ions reported in (esu 10^{-35} cm³/ion): (1) bridging oxygen $\alpha^{(3)} = 0.43$, (2) nonbridging oxygen $\alpha^{(3)} = 0.60$, (3) Na⁺, $\alpha^{(3)} = 0.60$, (4) K⁺, $\alpha^{(3)} = 1.0$, and (5) Rb⁺, $\alpha^{(3)} = 2.2$. From their findings, it appears that the contribution to the total nonlinear refraction coefficient of the individual chemical species increases with increasing ionic radius. Since the valence electrons of large ions can be considered spherical, they can be easily distorted by strong optical fields. The bridging oxygen are covalently bonded, and their electrons are not expected to distort as much as the nonbridging oxygen.

The glass structure becomes more ionic as the Eu₂O₃ concentration is increased. This is due to the fact that the systematic addition of the large Eu ions increasingly breaks some of the oxygen bonds that connect the SiO₄ tetrahedral units together. For example, we would expect to find more nonbridging oxygens in B10 than in B5 per molar volume. However, we note from Table IV.18 that

there appears to be a density dependence of the nonlinear refraction coefficient. This may be understood in terms of the total number of hyperpolarizable entities and the magnitude of their $\alpha^{(3)}$ that exist in the glass per unit volume. For the B5 sample, there are more hyperpolarizable entities in a unit volume of the glass than B6 and, therefore, should expect the nonlinear refraction coefficient to be larger for B5 than B6. The density of the glasses steadily increases from B6 to B10 with Eu ion concentration due to the larger mass of the ion. The Eu^{3+} ion is expected to exhibit a large $\alpha^{(3)}$ because of its large ionic radius. Therefore, we should expect the nonlinear refraction coefficient to increase for B6 to B10 as the number of Eu^{3+} increases per unit volume. This conclusion appears to be supported by our data. The almost three-fold (2.8) increase in γ from B9 to B10 does not seem unreasonable if we assume that the number density of Eu^{3+} doubles in going from B9 to B10 and also increases the number density of the nonbridging oxygen.

Finally, we consider the B12 and B14 samples that contain mixed alkali. The percent of Na^+ present in B9 is equally split into Li^+ and Na^+ for B12 and K^+ and Na^+ for B14. We did not detect any differences in γ between the samples. In addition, the γ value is about twice that of B9 which just contains Na^+ . We would expect B14 to have a larger γ than B12 because of the larger $\alpha^{(3)}$ of K^+ and B9 to have a larger γ than B12 since the $\alpha^{(3)}$ of Na^+ is expected to be larger than that of Li^+ .⁸⁰ It appears that the presence of mixed alkali ions enhances the nonlinearity that is not apparent from the simple model of Boling *et al.*⁸⁷ Additional studies need to be done concerning the contributions to γ from this mixed alkali-effect before commenting any further.

(c) Intensity-scan (millisecond)

We report the results from the millisecond Intensity-scan experiments that were performed on the Eu-doped alkali-silicate glasses that had the alkali ion replaced systematically from Li, Na, K, Rb, to Cs. These glasses had been investigated by Gangwere *et al.*³⁶ by Brillouin scattering and Behrens *et al.*³⁵ by four-wave mixing and were available to us. Unfortunately, the Eu-doped alkali-silicate glasses with systematic Eu-variation were not available for this study. However, we expect the B10 sample to have a thermal nonlinearity comparable to the NS sample due to their similarity in composition.

The glasses were fairly thick ranging from 2.75 mm to 4.37 mm but were optically *thin* when compared to the Rayleigh range of 12.1 mm, and we could safely use the thin lens approximation to derive the nonlinear refraction coefficients. Like the lead silicate glasses, the samples were placed before the focal point of the lens. The Intensity-scan plots are shown in Fig. IV.19, and the corresponding steady-state change in the index of refraction are shown in Fig. IV.20. From the Intensity-scan plot, we can conclude that the thermal nonlinear refraction coefficient γ_{th} is positive because of the negative slope. The γ_{th} values of the glasses are listed in Table IV.19 along with their absorption coefficients. These values do not follow a trend based on compositional characteristics such as increasing ionic radii of the alkali ions. They do, however, strongly follow the strength in absorption. The KS sample has the highest absorption coefficient of 1.98 cm^{-1} and has the highest γ_{th} value of $27.6 \text{ cm}^2/\text{GW}$. The RS sample has the smallest absorption coefficient of 0.24 cm^{-1} and therefore has the smallest γ_{th} value of $4.35 \text{ cm}^2/\text{GW}$. Since Δn_0 is directly proportional with α , these results are understandable. We are unaware of any thermo-optic coefficients derived for

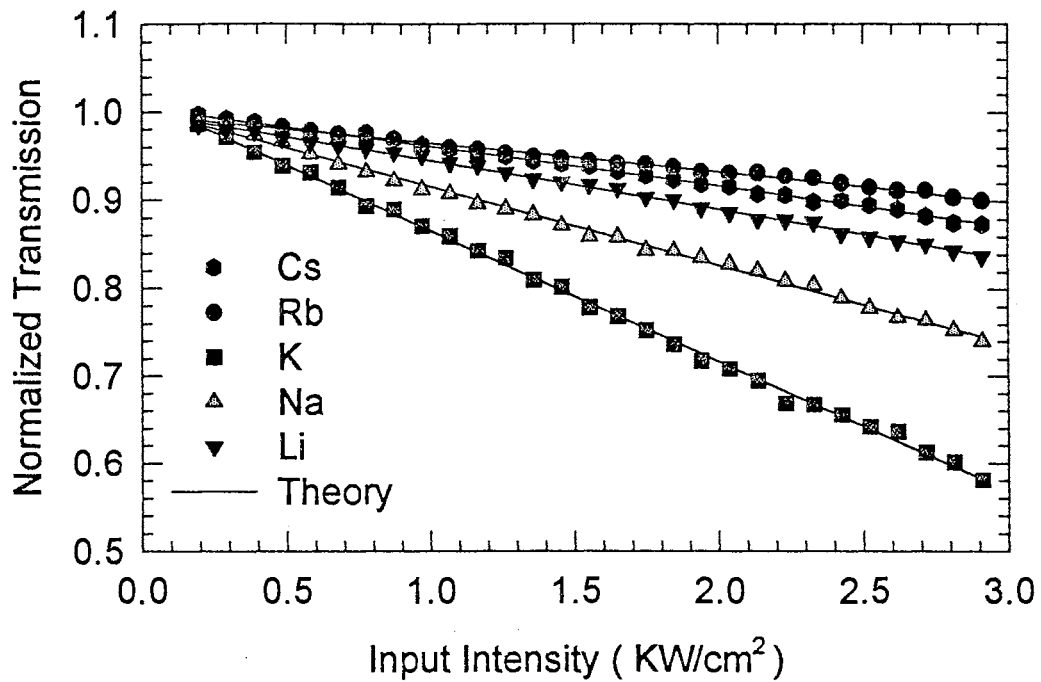


Fig. IV.19 Intensity-scan data for the Eu-doped alkali silicate glasses.

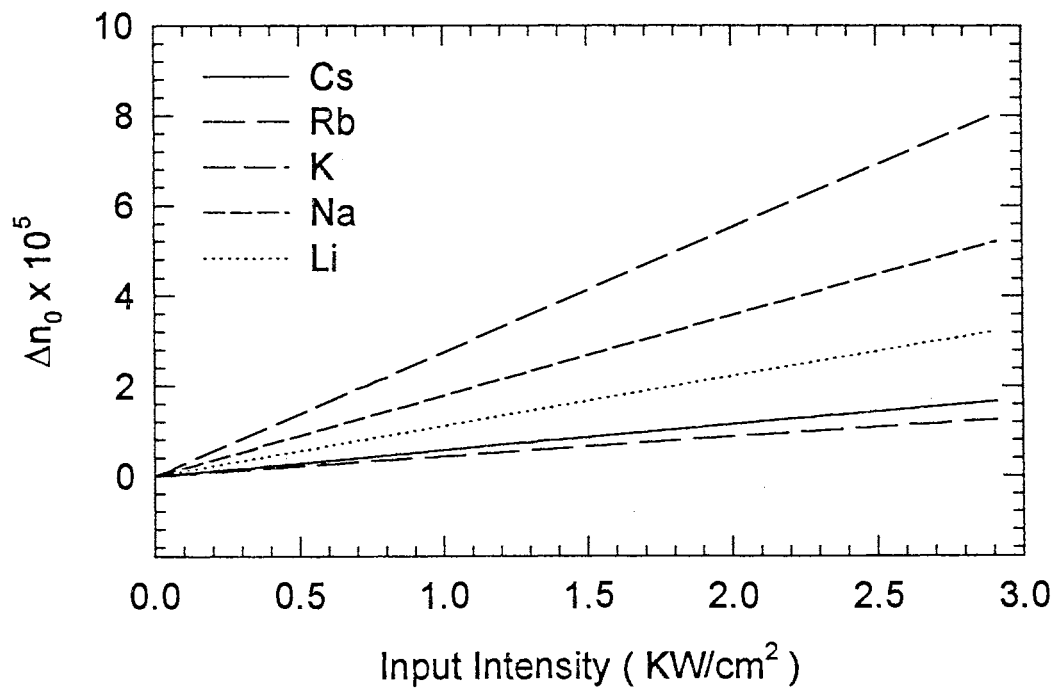


Fig. IV.20 The change in refractive index for the Eu-doped alkali silicate glasses.

Table IV.19 The thermal nonlinear refraction coefficients for the alkali-silicate glasses along with the absorption coefficients.

Sample	α (cm ⁻¹)*	γ_{th} (cm ² /GW)	slope ($\times 10^{-4}$ /mW)
LS	0.6	11.1	-5.308
NS	1.49	17.9	-8.585
KS	1.98	27.6	-14.39
RS	0.24	4.35	-3.144
CS	0.43	5.74	-4.312

* After Ref. [36].

these glasses but expect dn/dT to increase in the direction from Li to Cs because of the increasing polarizability of the alkali ion.⁸⁰ The graph in Fig. IV.21 clearly shows the absorption dependence of the thermal nonlinearity for these glasses. Therefore, it seems from our data that the absorption coefficient is the dominant factor that determines the thermal nonlinearity and also that the dn/dT values of the glasses are probably similar in magnitude. If dn/dT was the dominating factor, we would expect γ_{th} to increase from Li to Cs as can be seen from Eq. IV.15.

By using the photoelastic constants and Poisson's ratio from Ref. [36], we may derive the contributions of laser induced stress to the conventional dn/dT value of these glasses. These values are shown in Table IV.20 along with the relevant parameters taken from Ref. [36]. The volume expansion coefficients β_{ex} are not known for these glasses and so we show $(dn/dT)_{\sigma=0}/\beta_{ex}$. We also show the value of $(dn/dT)_{\sigma=0}$ using a constant value for $\beta_{ex} = 21 \times 10^{-6} \text{ K}^{-1}$ for all the

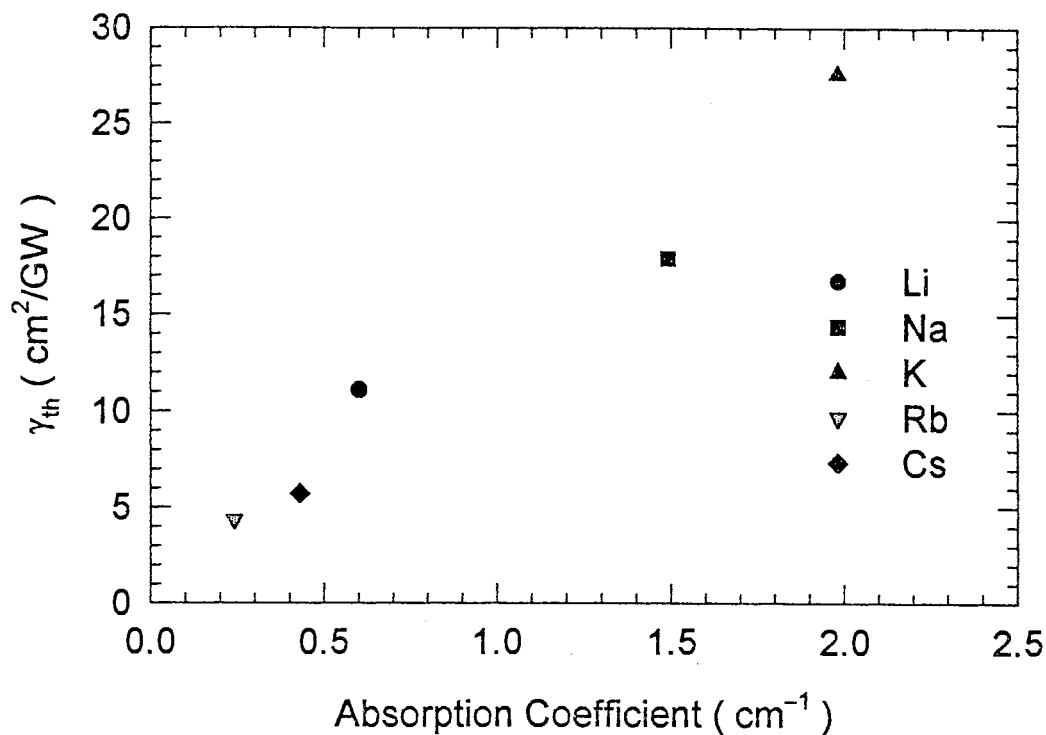


Fig. IV.21 Plot of γ_{th} versus α for the Eu-doped alkali silicate glasses.

samples. This β_{ex} value is for a sodium silicate glass with 15% Na_2O . The laser induced stress dn/dT is shown to increase as the alkali is changed from Li to Cs. This is expected because Gangwere *et al.* have shown that the glasses strain easier by changing the alkali from Li to Cs. The reason for this can be traced back to the increase in bond length between the alkali and the nonbridging oxygen due to the decrease in field strength of the alkali ion in going from Li to Cs.

Finally, we calculate the electrostrictive contribution to the nonlinear refraction coefficient which is shown in Table IV.21. Although we have designated it by γ_{th} , there are actually other nonlinear effects that take place. The electrostrictive contribution is shown to increase as the alkali is changed from Li to Cs

but minuscule compared to the total nonlinear refraction coefficient. This justifies our using the designation γ_{th} .

Table IV.20 The laser induced stress dn/dT for the alkali-silicate glasses along with photoelastic constants and Poisson's ratio.

Sample	p_{12}^*	p_{11}^*	Poisson's ratio*	$(dn/dT)_{\sigma \neq 0} / \beta_{ex}$	$(dn/dT)_{\sigma \neq 0}$ ($\times 10^6 \text{ K}^{-1}$)
LS	0.191	0.087	0.24	0.147	3.09
NS	0.230	0.126	0.24	0.177	3.71
KS	0.207	0.125	0.25	0.159	3.33
RS	0.244	0.158	0.25	0.186	3.91
CS	0.251	0.183	0.26	0.199	4.18

* After Ref. [36].

Table IV.21 The electrostrictive contribution to the total nonlinear refraction coefficient along with LA sound velocity and density.

Sample	v_{LA} (km/s)*	density (g/cm^3)*	γ_{es} ($10^{-8} \text{ cm}^2/\text{GW}$)
LS	0.6	3.22	5.02
NS	1.49	3.21	7.73
KS	1.98	3.15	6.97
RS	0.24	3.47	9.57
CS	0.43	3.74	11.4

* After Ref. [36].

CHAPTER V

SUMMARY AND RECOMMENDATIONS

This dissertation concerned the nonlinear optical properties of binary lead silicate and Eu-doped alkali-silicate glasses. We attempted to understand the nonlinear optical properties in terms of the compositional changes that occurred between samples of the same family and also used some simple models that relate the nonlinear refraction coefficient to the hyperpolarizabilities of the constituents ions and other material properties. Based on the current level of understanding of the structure of glasses, the conclusions drawn from our results provide reasonable explanations of the observed nonlinear behavior.

We will first summarize the main findings of the lead silicate glasses. The consensus appears to be that PbO can act as a network modifier at small concentrations and a network former at large concentrations. The major disagreement seems to be in the manner in which PbO forms a network. The Brillouin scattering results indicate that the glass structure becomes progressively weaker as the PbO concentration increases. The gradual disappearance and reappearance of the TA phonon as the PbO content increased from 32% to 62% (mole) was interpreted as an indication of a structural change from a stronger silicate-based glass to a weaker lead-based glass.

The nonlinear optical properties of the lead silicates were seen to increase with PbO concentration on both the nanosecond and millisecond time-scales. The

optical Kerr effect is most likely the dominating factor to the nonlinear refractive index on the nanosecond time-scale. The thermal and electrostrictive effects did not have sufficient time to develop, and thus their contributions to γ are much smaller. The large hyperpolarizability of the lead ions seems to be the cause of the large γ values observed. The nonlinear absorption coefficient β was also seen to increase with PbO content and the electrons taken part in the process were probably excited to the 5.3 eV band in the UV spectrum. The β values were also seen to scale inversely with the UV absorption edge. The millisecond Intensity-scan results showed that the thermal change in the refractive index also increased with PbO content and was due to the large polarizability of the lead and non-bridging oxygen ions. The laser-induced stress contribution to the conventional value of the thermo-optic coefficient was seen to increase with PbO content because it became progressively easier to stress the glasses.

The elastic properties of the first family of the Eu-doped alkali-silicate glasses showed a density dependence. The photoelastic behavior (at least $|p_{44}|$ and perhaps p_{12}) was in accordance with the theory developed by Carleton. The nonlinear refraction coefficient on the nanosecond time-scale for the same family of Eu-doped alkali-silicate glasses showed that the hyperpolarizability of the Eu^{3+} ion was a large contributing factor. No nonlinear absorption was detected for the intensity range and wavelength used in the experiment, though it may be observable at higher intensities and/or other wavelengths. The thermal change in the index of refraction as determined from the millisecond Intensity-scans for the second family of Eu-doped alkali-silicate glasses showed that the absorption coefficient was the determining factor.

Finally, we mention specific advances we have made in nonlinear optics. A generalized theory was developed to account for beam ellipticity for the popular Z-scan and related Intensity-scan techniques for both optically *thin* and *thick* media. It should be mentioned that we were the first to investigate the effects of beam ellipticity on these two nonlinear optics techniques. For the Intensity-scan, we have shown that if there is uncertainty about the quality of the beam profile, then it is possible to take the ratio of slopes to determine the nonlinear refraction coefficient. The Intensity-scan technique was extended to the millisecond time-scale to detect thermal nonlinearities and was shown to be highly sensitive to small wavefront distortions. A modified version of the familiar Brewster's angle technique was also developed to measure the refractive indices of materials both quickly and accurately.

The nonlinear optical properties of glasses need to be investigated further from both a fundamental and technological point of view. In particular, we need to understand the role of nonlinear absorption better both theoretically and experimentally. The dispersion of the nonlinear refraction coefficient and its behavior near resonance would also prove interesting. By comparing and contrasting data for γ and β over a wide frequency range with that of semiconductors, it may be possible to develop a consistent theory that explains the nonlinear behavior of glasses. Glasses with high nonlinear refraction coefficients, such as the lead silicate system, should be studied in the femtosecond regime to determine their electronic nonlinearity without having complications from other effects. Determining the nuclear contribution to the nonlinear refraction coefficient for these glasses from Raman scattering measurements could possibly be done in the future. A knowledge of the origin and dispersion of γ and β is essential to a better understanding of nonlinear optical properties of glasses.

BIBLIOGRAPHY

1. M. Sheik-Bahae, A. A. Said, and E. W. Van Stryland, *Opt. Lett.* 14, 955 (1989).
2. M. Sheik-Bahae, A. A. Said, T. H. Wei, D. J. Hagan, and E. W. Van Stryland, *IEEE J. Quantum Electron.* QE-26, 760 (1990).
3. A. A. Said, M. Sheik-Bahae, D. J. Hagan, T. H. Wei, J. Wang, J. Young, and E. W. Van Stryland, *J. Opt. Soc. Am. B* 9, 405 (1992).
4. M. Sheik-Bahae, J. Wang, R. Desalvo, D. J. Hagan, and E. W. Van Stryland, *Opt. Lett.* 17, 258 (1992).
5. J. Wang, M. Sheik-Bahae, A. A. Said, D. J. Hagan, and E. W. Van Stryland, *J. Opt. Soc. Am. B* 11, 1009 (1994).
6. W. D. St. John, B. Taheri, J. P. Wicksted, R. C. Powell, D. H. Blackburn, and D. C. Cranmer, *J. Opt. Soc. Am. B* 9, 610 (1992).
7. B. Taheri, A. Munoz F., W. D. St. John, J. P. Wicksted, R. C. Powell, D. H. Blackburn, and D. C. Cranmer, *J. Appl. Phys.* 71, 3693 (1992).
8. H. Ma, A. S. L. Gomes, and C. B. de Araujo, *Opt. Comm.* 87, 19 (1992).
9. W. Zhao and P. Palffy-Muhoray, *Appl. Phys. Lett.* 65, 673 (1994).
10. Y. M. Cheung and S. K. Gayen, *J. Opt. Soc. Am. B* 11, 636 (1994).
11. B. A. Rockwell, W. P. Roach, M. E. Rogers, M. W. Mayo, C. A. Toth, C. P. Cain, and G. D. Noojin, *Opt. Lett.* 18, 1792 (1993).
12. H. Ma, A. S. L. Gomes, and C. B. de Araujo, *Appl. Phys. Lett.* 59, 2666 (1991).
13. J. Castillo, V. P. Kozich, and A. Marcano O., *Opt. Lett.* 19, 171 (1994).
14. T. Xia, D. J. Hagan, M. Sheik-Bahae, and E. W. Van Stryland, *Opt. Lett.* 19, 317 (1994).
15. J. G. Tian, W. P. Zang, and G. Zhang, *Opt. Comm.* 107, 415 (1994).
16. D. V. Petrov, A. S. L. Gomes, and C. B. de Araujo, *Appl. Phys. Lett.* 65, 1067 (1994).
17. R. L. Sutherland, *Appl. Opt.* 33, 5576 (1994).

18. M. Sheik-Bahae, A. A. Said, D. J. Hagan, M. J. Soileau, and E. W. Van Stryland, *Opt. Eng.* **30**, 1228 (1991).
19. J. A. Hermann and R. G. McDuff, *J. Opt. Soc. Am. B* **10**, 2056 (1993).
20. P. B. Chapple, J. Staromlynska, and R. G. McDuff, *J. Opt. Soc. Am. B* **11**, 975 (1994).
21. W. Zhao and P. Palffy-Muhoray, *Appl. Phys. Lett.* **63**, 1613 (1993).
22. S. M. Mian and J. P. Wicksted, *J. Appl. Phys.* **77**, 5434 (1995).
23. S. M. Mian and J. P. Wicksted, *J. Opt. Soc. Am. B* **13**, 856 (1996).
24. A. J. Twarowski and D. S. Klinger, *Chem. Phys.* **20**, 253 (1977).
25. E. W. Van Stryland, H. Vanherzeele, M. A. Woodall, M. J. Soileau, A. L. Smirl, S. Guha, and T. F. Boggess, *Opt. Eng.* **24**, 613 (1991).
26. A. Yariv, *Quantum Electronics*, 3rd ed., (Wiley, New York, 1989), Ch. 6.
27. B. Taheri, H. Liu, B. Jassemnejad, D. Appling, R. C. Powell, and J. J. Song, *Appl. Phys. Lett.* **68**, 1317 (1996).
28. H. Z. Cummins and P. E. Shoen, *Laser Handbook*, (North-Holland Publ. Co., 1972), Ch. E1.
29. F. W. Dabby and J. R. Whinnery, *Appl. Phys. Lett.* **13**, 284 (1968).
30. F. W. Dabby, T. K. Gustafson, J. R. Whinnery, Y. Kohanzadeh, and P. L. Kelley, *Appl. Phys. Lett.* **16**, 362 (1970).
31. J. P. Gordon, R. C. C. Leite, R. S. Moore, S. P. S. Porto, and J. R. Whinnery, *J. Appl. Phys.* **36**, 3 (1965).
32. R. L. Carman, A. Mooradian, P. L. Kelley, and A. Tufts, *Appl. Phys. Lett.* **14**, 136 (1969).
33. G. S. Dixon, B. D. Gault, S. Shi, P. A. Watson, and J. P. Wicksted, *Phys. Rev. B* **49**, 257 (1994).
34. V. A. French, R. C. Powell, D. H. Blackburn, and D. C. Cranmer, *J. Appl. Phys.* **69**, 913 (1991).
35. E. Behrens, Ph.D. dissertation, Oklahoma State University (1990).
36. G. Gangwere, Ph.D. dissertation, Oklahoma State University (1990).
37. L. C. Oliveira and S. C. Zilio, *Appl. Phys. Lett.* **65**, 2121 (1994).
38. S. M. Mian, A. Y. Hamad, and J. P. Wicksted, *Opt. and Photon. News*, ELN, (May, 1996).
39. E. Hecht, *Optics*, 8th ed., (Addison-Wesley, New York, 1990), Chap. 34.
40. M. S. Whalen and J. Stone, *J. Appl. Phys.* **53**, 4340 (1982).

41. H. E. Bennett and J. M. Bennett, *Physics of Thin Films*, (Academic, New York, 1967), Vol.4
42. E. M. Rabinovich, *J. Mater. Sci.* 11, 925 (1976).
43. G. J. Bair, *J. Am. Ceram. Soc.* 13, 339 (1936).
44. J. Krogh-Moe, *Z. Phys. Chem.* 18, 223 (1958).
45. G. O. Bagdyk'yants and A. G. Alekseev, *Structure of Glass*, (Consultants Bureau, New York, 1960), Vol. 2.
46. C. Brosset, *Phys. Chem. Glass.* 4, 98 (1963).
47. P. Bray, M. Leventhal, and H. Hooper, *Phys. Chem. Glass.* 4, 47 (1963).
48. M. F. Mydlar, N. J. Kreidl, J. K. Hendren, and G. T. Clayton, *Phys. Chem. Glass.* 11, 196 (1970).
49. J. Gotz, D. Hoebbel, and W. Wieker, *J. NonCrys. Sol.* 22, 391 (1976).
50. H. Morikawa, Y. Takagi, and H. Ohno, *J. NonCrys. Sol.* 53, 173 (1982).
51. M. Leventhal and P. J. Bray, *Phys. Chem. Glass.* 6, 113 (1965).
52. M. Imaoka, H. Hasegawa, and I. Yasui, *J. NonCrys. Sol.* 85, 393 (1986).
53. R. Shuker and R. W. Gammon, *Phys. Rev. Lett.* 25, 222 (1970).
54. C. A. Worrel, T. Henshall, *J. NonCrys. Sol.* 29, 283 (1978).
55. M. Hass, *J. Phys. Chem. Sol.* 31, 415 (1970).
56. G. S. Dixon, P. A. Watson, J. P. Wicksted, and D. Bromwell, *J. Lum.* 60&61, 430 (1994).
57. V. N. Novikov, E. Duval, A. Kisliuk, and A. P. Sokolov, *J. Chem. Phys.* 102, 4691 (1995).
58. A. S. Pine, *Light Scattering in Solids I*, 2nd ed., (Springer-Verlag, New York, 1983), Vol.2.
59. E. Ellis, D. W. Johnson, A. Breeze, P. M. Magee, and P. G. Perkins, *Phil. Mag.* 40, 125 (1979).
60. K. Boer, *Survey of Semiconductor Physics*, (Van Nostrand Reinhold, New York, 1990), Ch.4.
61. J. Schroeder, *Treatise on Materials Science and Technology*, (Academic Press, New York, 1977), Vol. 12.
62. H. R. Carleton, *Amorphous Materials*, (Wiley, New York, 1972), Ch. 10.
63. J. Schroeder, *J. NonCrys. Sol.* 40, 549 (1980).
64. K. Matusita, H. Kato, T. Komatsu, M. Yoshimoto, and N. Soga, *J. NonCrys. Sol.* 112, 341 (1989).

65. K. Matusita, C. Ihara, T. Komatsu, and R. Yokota, *J. Am. Ceram. Soc.* 67, 700 (1984).
66. W. D. St. John, J. P. Wicksted, and G. Cantwell, *J. Appl. Phys.* 73, 3013 (1993).
67. B. M. Cohen, D. R. Uhlmann, and R. R. Shaw, *J. NonCrys. Sol.* 12, 177 (1973).
68. W. A. Weyl and E. C. Marboe, *The Constitution of Glasses. A Dynamic Interpretation*, (Wiley, New York, 1964), Vol. I, II.
69. A. Paul, *Phys. Chem. Glass.* 11, 46 (1970).
70. A. J. Bourdillon, F. Khumalo, and J. Bordas, *Phil. Mag.* 37, 731 (1978).
71. S. R. Elliot, *Physics of Amorphous Materials*, (Longman, New York, 1984), Ch. 5.
72. B. D. McSwain, N. F. Borrelli, and G. Su, *Phys. Chem. Glass.* 4, 1 (1963).
73. L. Prod'homme, *Phys. Chem. Glass.* 1, 119 (1960).
74. M. Sparks, *J. Appl. Phys.* 42, 5029 (1971).
75. L. D. Landau, *Theory of Elasticity*, 2nd ed., (Pergamon Press, New York, 1970).
76. A. Feldman, D. Horowitz, and R. M. Waxler, *IEEE J. Quantum Electron.* QE-9, 1054 (1973).
77. R. D. Greenough, P. Dentschuk, and S. B. Palmer, *J. Mater. Sci.* 16, 599 (1981).
78. W. F. Hagan and E. Snitzer, *IEEE J. Quantum Electron.* QE-4, 361 (1968).
79. I. Kang, T. D. Krauss, F. W. Wise, B. G. Aitken, and N. F. Borrelli, *J. Opt. Soc. Am. B* 12, 2053 (1995).
80. H. Nasu, O. Sugimoto, J. Matsuoka, and K. Kamiya, *J. NonCrys. Sol.* 182, 321 (1995).
81. E. M. Vogel, S. G. Kosinksi, D. M. Krol, J. L. Jackel, S. R. Friberg, M. K. Oliver, and J. D. Powers, *J. NonCrys. Sol.* 107, 244 (1989).
82. R. Adair, L. L. Chase, and S. A. Payne, *J. Opt. Soc. Am. B* 4, 875 (1987).
83. V. Mizrahi, K. W. DeLong, and G. I. Stegeman, M. A. Saifi, and M. J. Andrejco, *Opt. Lett.* 14, 1140 (1989).
84. M. Sheik-Bahae, D. C. Hutchings, D. J. Hagan, and E. W. Van Styland, *IEEE J. Quantum Electron.* QE-27, 1296 (1991).
85. D. Heiman, R. W. Hellwarth, and D. S. Hamilton, *J. NonCrys. Sol.* 34, 63 (1979).

86. J. P. Wicksted (private communication).
87. N. L. Boling, A. J. Glass, and A. Owyong, IEEE J. Quantum Electron. QE-14, 601 (1978).
88. P. P. Banerjee, R. G. Lindquist, J. M. Lee, and R. M. Misra, 1994 OSA Annual Meeting/ILS-X Program, WII5, p.129.
89. J. H. Marburger, Prog. Quant. Electr. 4, 35 (1975).
90. V. V. Vorob'jev, IVUZ Radiofiz. 13, 1905 (1970).
91. A. B. Schwarzburg, IVUZ Radiofiz. 12, 1775 (1970).
92. F. Cornolti, M. Lucchesi, and B. Zambon, Opt. Comm. 75, 129 (1990).
93. B. Crosignani and P. Di Porto, Opt. Lett. 18, 1394 (1993).
94. A. Yariv and P. Yeh, Opt. Comm. 27, 295 (1978).
95. J. R. Sandercock, Fabry-Perot Operating Manual (Switzerland,1994).
96. S. M. Mian, Fabry-Perot Supplementary Notes (OSU, 1994).
97. J. R. Sandercock, Sol. Stat. Comm. 26, 547 (1978).

APPENDICES

APPENDIX A

EFFECTS OF BEAM ELLIPTICITY ON THE Z-SCAN SIGNATURE

1. Introduction

A wave optics theory pertaining to Z-scans was developed by closely following the original work of Sheik-Bahae *et al.*^{1,2} so as to compare and contrast the effects of beam ellipticity. To that end, we will call the beams with circular symmetry circular beams and elliptic otherwise, though it should be clear that a circular beam is just a special kind of an elliptic beam and the theory developed applies to *all* elliptic beams. We describe the various beam shapes by an ellipticity parameter e , defined as the ratio of the semi-major to semi-minor axes. We demonstrate how the ellipticity changes the Z-scan signature and how additional peaks and valleys arise for closed apertures.

2. Theoretical Results

The overall behavior of $T(z)$ as given in Eq. II.43 is now studied. Recall that x and y continuously change throughout the Z-scan. Far away from the focus both $|x, y| \gg 1$ and so $T(z) \cong 1$. It is only when $z - z_{x,y} \approx z_{0x,0y}$ that there is appreciable change in $T(z)$ in that the transmission goes above or below the $T(z) = 1$ line. There is a null in the Z-scan when the transmission crosses this line and it

occurs when the numerator in the radical of Eq. II.43 equals zero. This translates to the following relationship between x and y :

$$x(y^2 + 3) + y(x^2 + 3) = 0. \quad (\text{A.1})$$

The solutions of this equation are $x = -y, -3/y$. When $x = -y$, the null occurs at

$$z_{null} = (z_x z_{0y} + z_y z_{0x}) / (z_{0x} + z_{0y}). \quad (\text{A.2})$$

This expression applies to both circular and elliptic beams. Note that for a circular Gaussian beam, $z_x = z_y = z_{min}$ and thus $z_{null} = z_{min}$ as it should be. On the other hand, when $x = -3/y$ another null is located at

$$z_{null} = \frac{1}{2} \left\{ (z_y + z_x) \pm \sqrt{(z_y - z_x)^2 - 12z_{0x}z_{0y}} \right\} \quad (\text{A.3})$$

which can occur *only* for an elliptic beam provided that the waist separation $|z_y - z_x|$ is greater than or equal to $\sqrt{12z_{0x}z_{0y}}$. If the waist separation is equal to this quantity, then the additional null will be located at the midpoint between the waists. If it is not, then there will be two nulls equidistant from the midpoint of the waists. It can be concluded that the Z-scan signature for such a beam may contain an additional peak and valley depending on the beam ellipticity and particular geometry used. This conclusion is in qualitative agreement with a recent experiment where the incoming beam was circular but the sample studied was anisotropic.⁸⁸ This work is conjugate to that of Ref. [88] in that in both cases, the electric field at the exit plane has a nonlinear phase shift that is anisotropic.

We now investigate the geometry-independent on-axis transmission as given by Eq. II.43 graphically. A positive nonlinearity is chosen to illustrate the theory but it is a simple matter to extend it for a negative one. A contour plot with a small nonlinearity $\Delta\Phi_0 = 0.1$ is shown in Fig. A.1 from which the effects

of beam ellipticity can be seen. All elliptic beams can be represented by a curve on this plot. We can write this quantitatively with the line

$$y = (z_{0x}/z_{0y})x - (\Delta z_{xy}/z_{0y}) \quad (\text{A.4})$$

where $\Delta z_{xy} = z_y - z_x$ is the separation of the waists, and we take w_y and w_x to be the semi-major and minor axes, respectively. Thus, for an elliptic beam the intercept is always negative ($\Delta z_{xy} \geq 0$) and the slope is always greater than 1 ($z_{0x} \geq z_{0y}$). The curves $x = -y$ and $xy = -3$ demarcates the region where the transmission goes above or below the $T(z) = 1$ line. The major and minor contours are shown with solid and dotted lines, respectively. The extraneous lines at the ends of the line $x = -y$ are just noise in producing the contour plot. By following the $y = x$ line, the circular Gaussian Z-scan is reproduced. Any other line given by Eq. A.4 represents an elliptic beam. It is easy to see from this plot how the signature gets modified and also how an additional peak and valley may appear in the Z-scan.

Some specific examples are now discussed so that the role of beam ellipticity may be better understood. We take a 250 mm focal length lens, a small nonlinearity $\Delta\Phi_0 = 0.1$, and a prefocused beam radius of $w_y = 2$ mm, $w_x = 2, 1.5, 1, 0.4, 0.3,$ and 0.2 mm. The graphs are shown in Fig. A.2. For a negative nonlinearity, the plots are identical but mirrored on the $T(z) = 1$ line. We notice that with an increase in ellipticity both peak and valley reduce from their symmetric maximum and minimum that was attained in the circular limit. However, the valley tends to approach $T(z) = 1$ sooner than the peak as the ellipticity is increased. In Fig. A.3, a Z-scan with an ellipticity of 5.5 ($w_y = 1.1$ mm, $w_x = 0.2$ mm) with the same nonlinearity is shown where an extra peak is observed at

about 195 mm. The transmission actually reaches a very weak local minimum at 52 mm. The dominant peak and valley occur at 256 mm and 236 mm, respectively. The nulls are located at 243 mm, 213 mm, and 172 mm. This particular graph (Fig. A.3) corresponds to the line $y = 16.48x - 15.05$ on the contour plot.

There is a simple physical explanation for these modifications in the Z-scan signature. It can be understood in terms of the astigmatic focus of the beams and two crossed cylindrical lenses representing the sample, each lens modifying a *beam*. If the waists are separated by a large distance, then the effects of the individual beams can be seen in the Z-scan. The smaller *x-beam* focuses closer to the lens than the *y-beam*, i.e., $z_x < z_y$ and thus there are three regions along the z axis that need to be studied closely. When the sample position z is such that $z < z_x < z_y$, the incoming focused beams incur a nonlinear phase shift that causes both of them to diverge in the far-field and the transmission drops below the $T(z) = 1$ line. If the waist separation is large ($z_x \ll z_y$), then the sample for positions $z < z_x$ may be near the maximum lensing position of the *x-beam*. In that case, as z increases from $z < z_x$ to $z > z_x$ the transmission will initially go down, pass through a local minimum, and then rise. If the waist separation is small, then the transmission will continue to go down for $z > z_x$. When $z_x < z < z_y$, the incoming *x-beam* is defocusing while the *y-beam* is still focusing at the sample position. This means that the *x-beam* tends to collimate and the *y-beam* diverge in the far-field thus raising the transmission in a competing manner. The transmission will rise as the waist separation increases, approaching the $T(z) = 1$ line and eventually surpassing it which is indicative of a secondary peak. A little further away (increasing z) in the same region, the larger

y-beam will dominate and pull the transmission below this line. If the waists are located very close to each other, then the transmission will simply go down until it reaches its minimum value and eventually rise. Finally, when $z_x < z_y < z$ both incoming beams are diverging at the sample position which tend to collimate in the far-field and thus raise the transmission until maximum collimation is reached. As the sample gets further away from both focuses, the nonlinearity induced becomes smaller and the transmission drops to the $T(z) = 1$ line.

We have numerically looked at the behavior of the peak-valley transmission difference. Since there may be an extra peak and valley in the Z-scan, we define ΔT_{p-v} as the difference between the major peak and valley near the focus of the *y-beam*. A graph is shown in Fig. A.4 where ΔT_{p-v} divided by $\Delta\Phi_0$ is plotted against beam ellipticity. We keep the large waist w_y at 2 mm and change w_x . Two different lenses are used to separate the waists; a 50 mm and 500 mm focusing lens. As the waist separation Δz_{xy} increases for a given ellipticity e , the ratio $\Delta T_{p-v} / \Delta\Phi_0$ decreases. This nonlinear change in the ratio as a function of e and Δz_{xy} is dramatic for large ellipticity.

We can now investigate the qualitative effects of beam ellipticity for the open-aperture expression. During the Z-scan, the only quantity that is changing in Eq. II.49 is the beam area. For a beam with small ellipticity and waist separation, the area decreases, reaches its minimum and then increases parabolically in a symmetric manner as a function of sample position z . Thus, the Z-scan signature is expected to resemble that of a circular beam. However, for large ellipticity and waist separation the beam area changes like an asymmetric parabola. This is because the smaller *x-beam* focuses closer to the lens than the larger *y-beam* and they change the beam area in a competing manner for positions be-

tween their focus. By following the beams, it is easy to see that the net effect is to reduce the area for positions closer to the lens and increase it for all positions past the geometric focus in an asymmetric way. Hence, in general, we can expect a small degree of asymmetry in an open-aperture Z-scan for an elliptic beam.

The geometry-independent expression can be easily obtained for the open-aperture transmission from Eqs. II.50 and II.51 and is now graphically studied. A contour plot is shown in Fig. A.5. By using Eq. A.4, one can investigate the nature of the open aperture Z-scan signature for any elliptic beam. In particular, we look at the Z-scan of beams with waists $w_y = 2$ mm, $w_x = 2, 1,$ and 0.5 mm, with $Q_0 = 0.9$, and a 250 mm focusing lens as shown in Fig. A.6. The location of the transmission minimum is dominated by the large beam and the overall Z-scan shape changes from its circular counterpart. The main feature of the plots is the fact that the transmission minimum increases with increasing ellipticity. Since the knowledge of this minimum value and input irradiance are required from the experiment to find β ,³ it is important that the beam ellipticity be considered. The other characteristic of an open aperture Z-scan is its asymmetry. A Z-scan of a beam with waists $w_y = 0.8$ mm, $w_x = 0.2$ mm with $Q_0 = 0.9$ and using the same lens is shown in Fig. A.7 where this asymmetry is clearly observable. This graph corresponds to the equation $y = 8.74x - 7.94$ on the contour plot.

An interesting aspect about the Z-scan experiment is its applicability in optical limiting experiments. For a circular beam, the sample should be placed at the maximum lensing position of the beam which is at the valley of the Z-scan. We can similarly find the optimal position of the sample for an elliptic beam by simply placing it at the waist of one of the beams and theoretically scan with the

other. That is, set $x = 0$ in Eq. II.43 (sample is placed at the waist of the x -beam) and solve for y where $T(z)$ is a minimum. We find that when $y = -1.123$ or $\Delta z_{xy} = 1.123z_{0y}$, then $T(z)$ is a minimum. Thus for a given beam ellipticity, by suitably choosing a lens it is possible to minimize the transmission in an optical limiting experiment.

3. Conclusion

We have theoretically studied the effects of beam ellipticity on both open and closed aperture Z-scans. A thin lens wave optics model was developed closely following the formalism for circular beams to which it was compared and contrasted. The beam ellipticity e and waist separation Δz_{xy} were found to greatly influence the Z-scan signature. The appearance of an extra peak and valley in a closed aperture and an asymmetry in an open aperture Z-scan is predicted by the theory. From the contour plots of the geometry-independent transmissions, it is possible to envision any kind of Z-scan based on beam ellipticity. The peak-valley transmission difference ΔT_{p-v} was found to decrease nonlinearly as a function of e . It is clear that an assumption of a circular beam regardless of its ellipticity will produce Z-scan signatures which will deviate from experimental data. The amount of deviation will depend on how elliptic and how tightly focused the beam actually is in addition to the strength of the nonlinearity. We have found that for small waist separation and ellipticity, the circular beam formalism can be a good approximation. However, the anisotropy induced by the elliptic beam should be accounted for in order to obtain better agreement between theory and experiment.

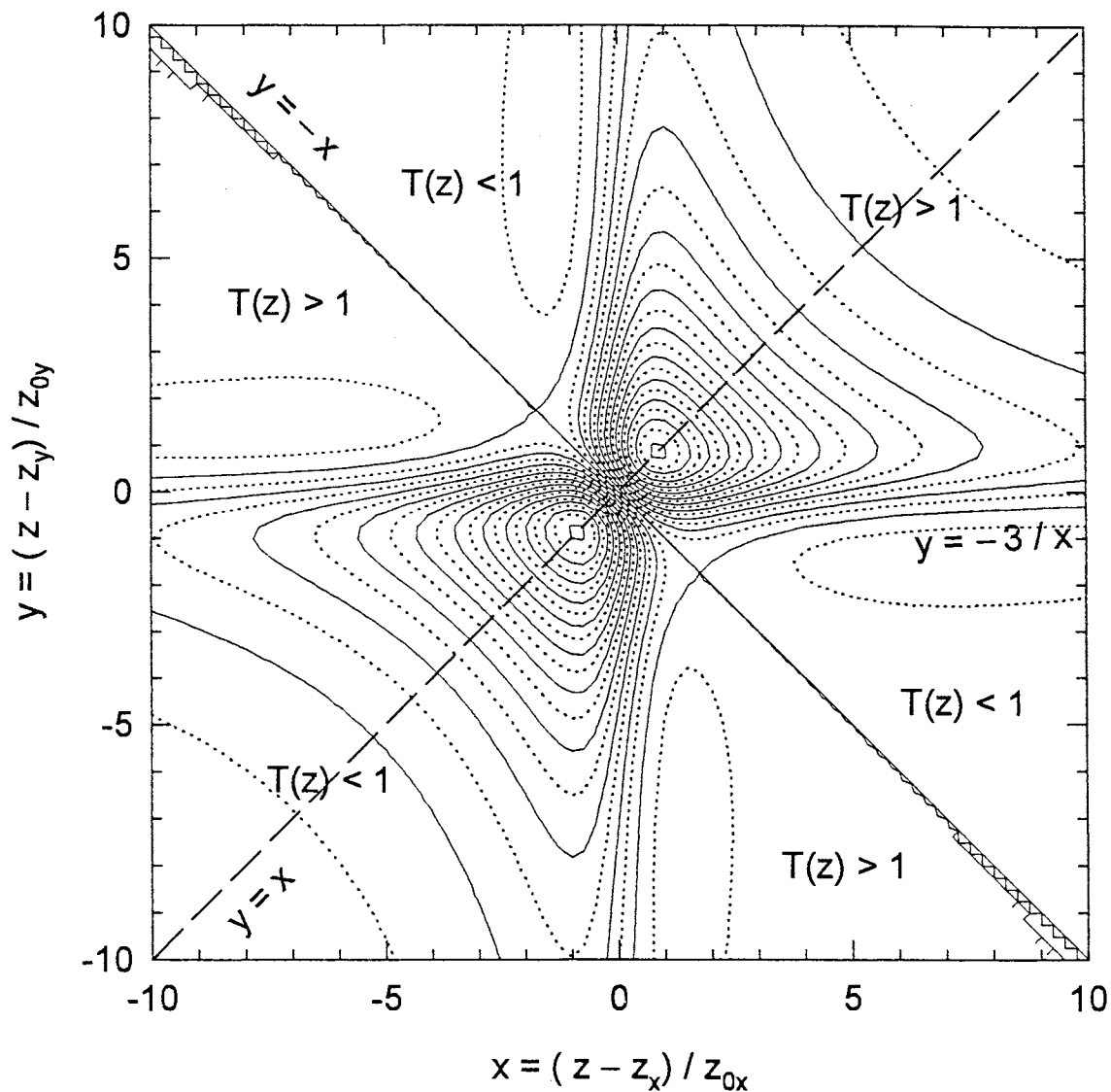


Figure. A.1 A contour plot of the closed aperture transmission. The circular beam lies along $y = x$. All possible closed Z-scan signatures can be envisioned from this plot by using Eq. A.4. The solid and dotted lines represent major and minor contour lines, respectively.

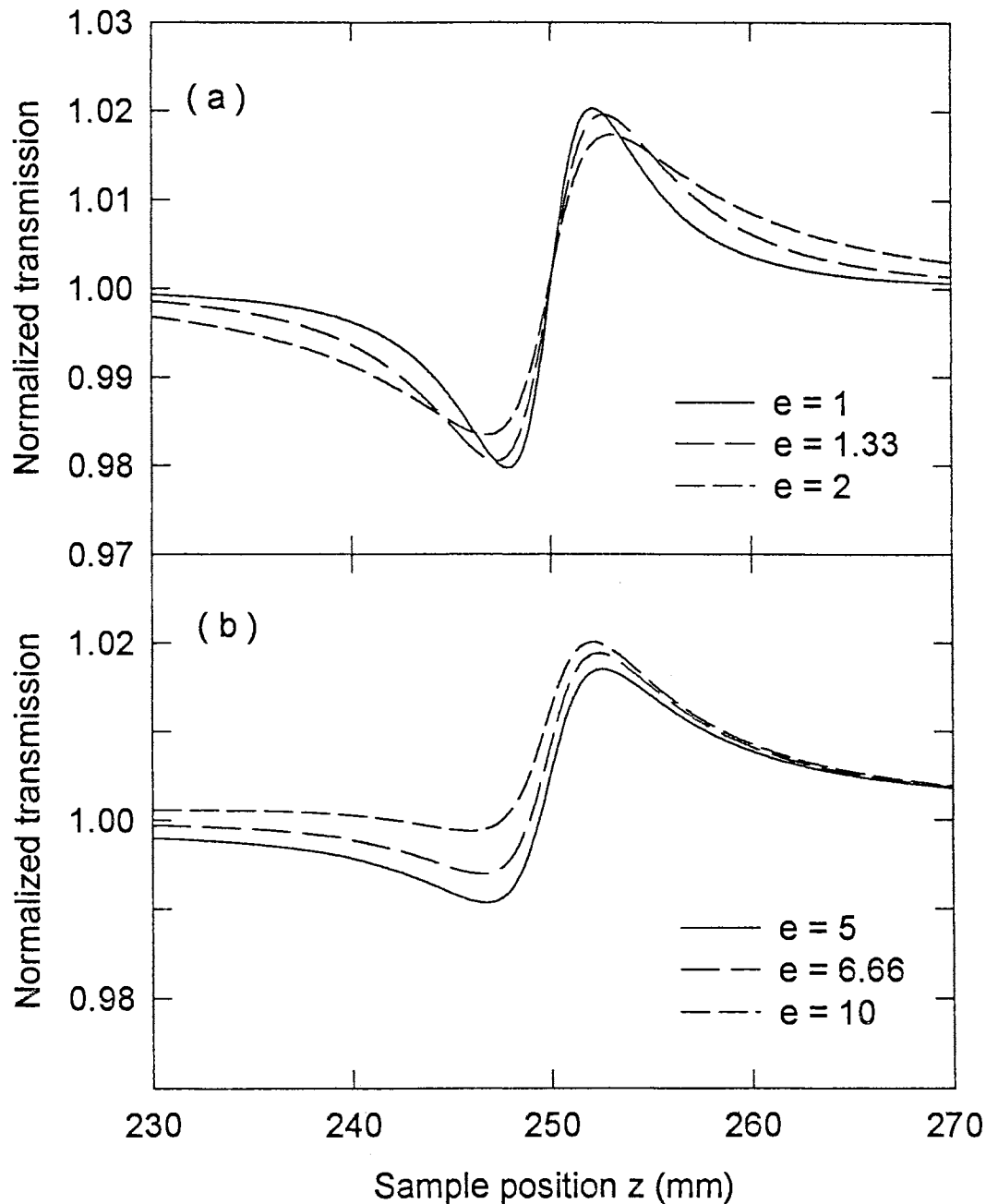


Figure. A.2 Specific examples of the effects of beam ellipticity on the closed aperture Z -scan signature. A small nonlinearity of $\Delta\Phi_0 = 0.1$ and a 250 mm focal length lens are used. The beams are characterized by their ellipticity. (a) The beams have waists $w_y = 2$ mm, $w_x = 2$, 1.5, and 1 mm. (b) The beams have $w_y = 2$ mm, $w_x = 0.4$, 0.3, and 0.2 mm.

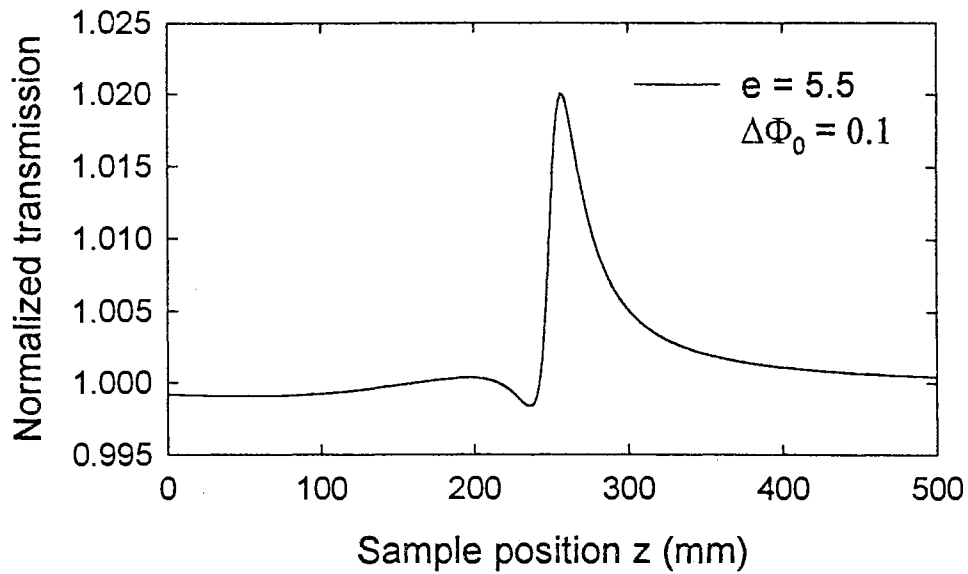


Figure. A.3 A beam with an ellipticity of $e = 5.5$ ($w_y = 1.1$ mm, $w_x = 0.2$ mm) and a sample nonlinearity of $\Delta\Phi_0 = 0.1$, is shown in a closed aperture Z-scan where an extra peak is observed. This curve corresponds to $y = 16.48x - 15.05$ as given by Eq. A.4.

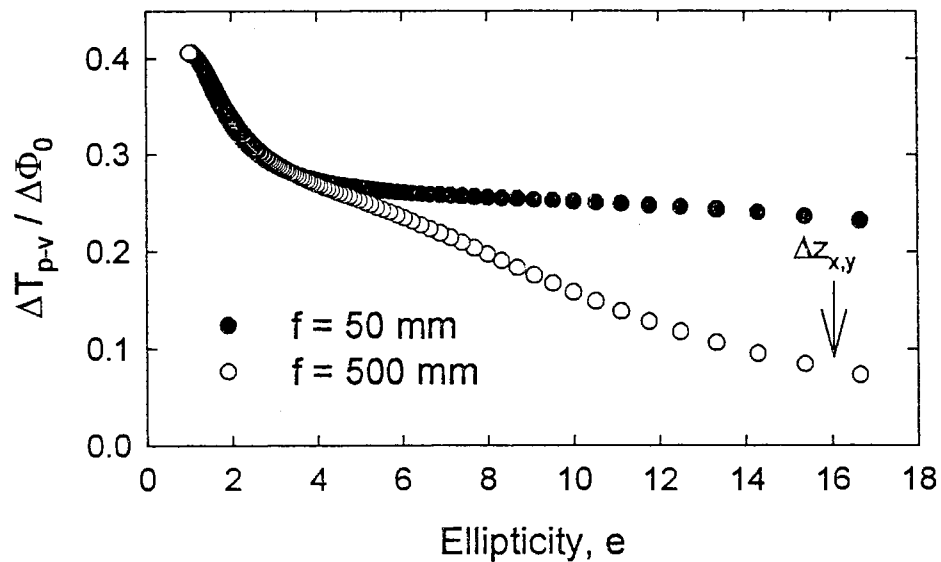


Figure. A.4 The nonlinear decrease of the ratio $\Delta T_{p-v}/\Delta\Phi_0$ as a function of ellipticity. The waist w_y is kept at 2 mm and w_x is changed. Two focusing lenses, 50 mm and 500 mm, are used to separate the waists. The arrow denotes the direction of increasing waist separation.

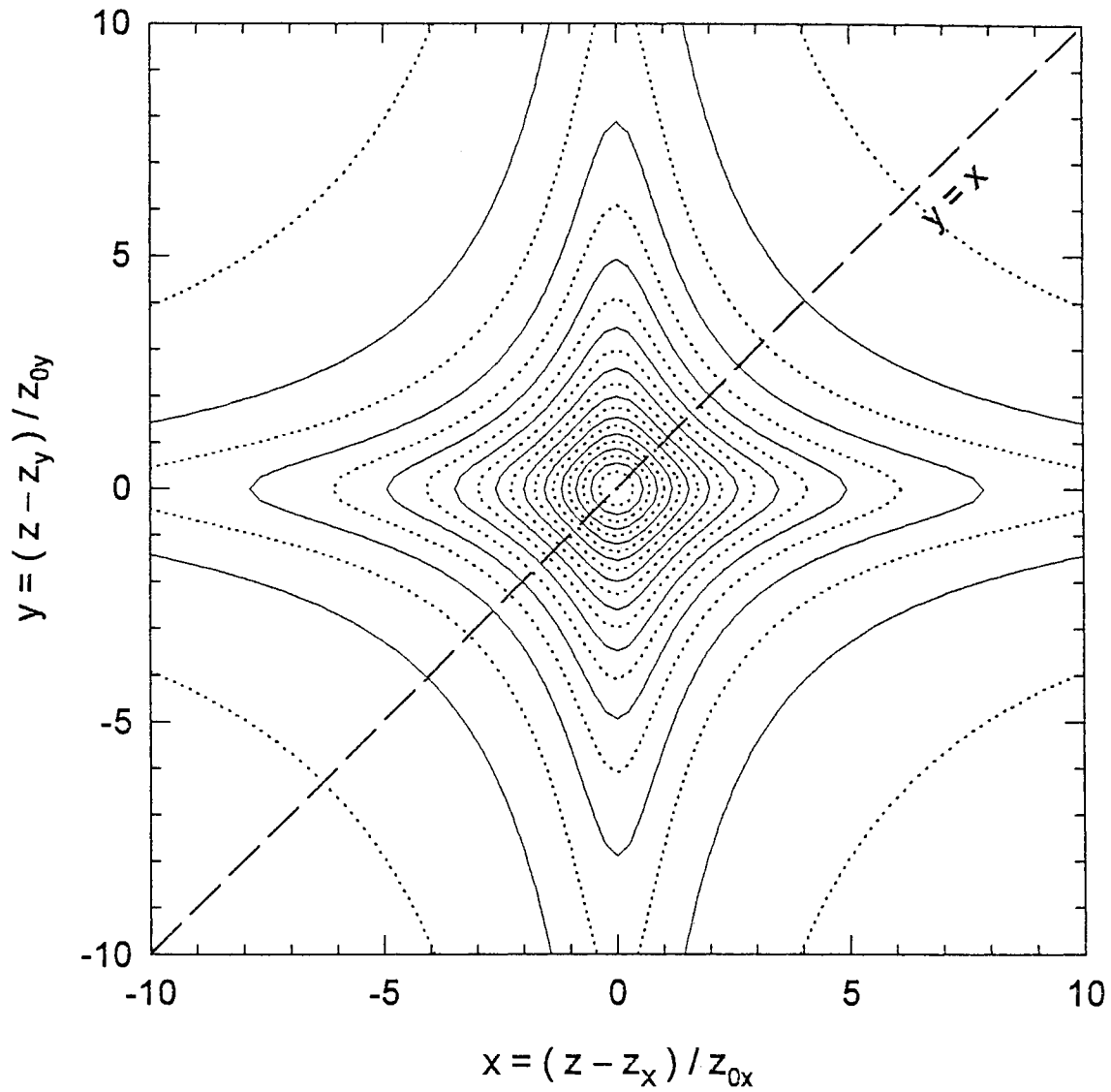


Figure. A.5 A contour plot of the open aperture transmission. The circular beam lies along $y = x$. All possible open aperture Z-scan signatures can be envisioned from this plot by using Eq. A.4. The solid and dotted lines represent major and minor contour lines, respectively.

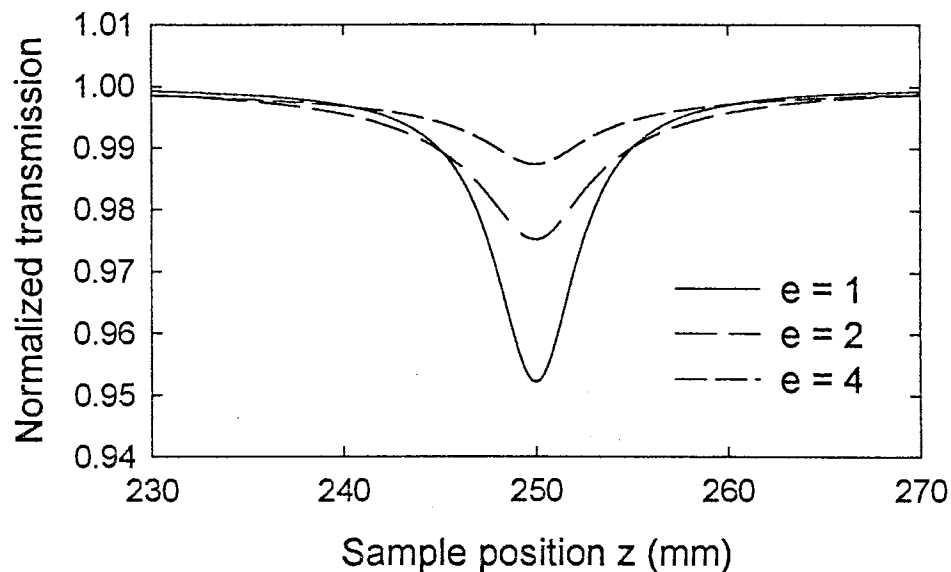


Figure. A.6 Specific examples of the effects of beam ellipticity on an open aperture Z-scan signature. A dimensionless irradiance of $Q_0 = 0.9$ and a 250 mm focal length lens are used. The beams have waists $w_y = 2$ mm, $w_x = 2, 1.0,$ and 0.5 mm, and are characterized in terms of their ellipticity.

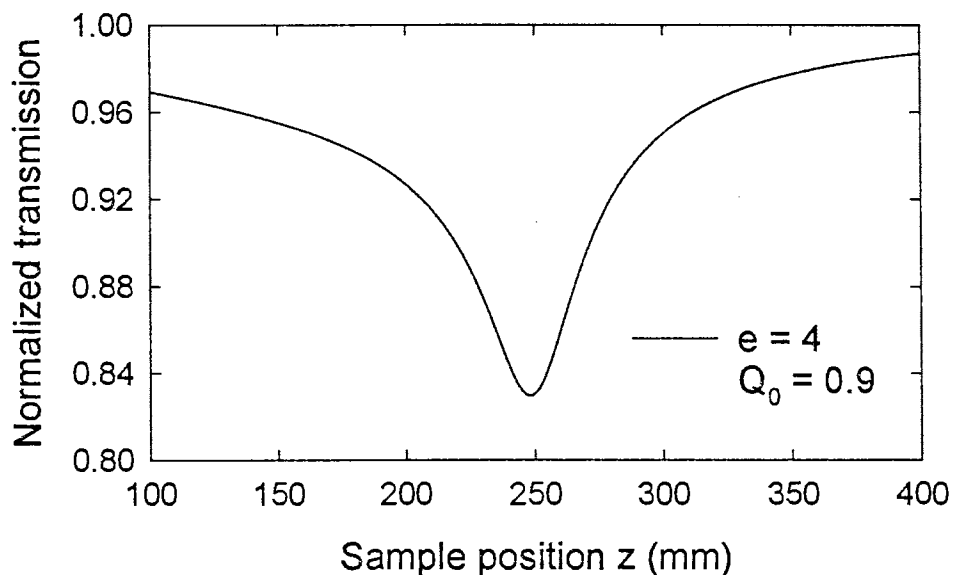


Figure. A.7 An open aperture Z-scan for a beam with waists $w_y = 0.8$ mm, and $w_x = 0.2$ mm and a focusing lens of 250 mm is shown. A dimensionless irradiance of $Q_0 = 0.9$ is used and a small degree of asymmetry is observed.

APPENDIX B

PROPAGATION OF ELLIPTIC BEAMS IN A KERR MEDIUM

1. Introduction

Self-focusing of optical beams have been studied extensively for the past three decades. Both numerical and approximate methods have been employed to solve the scalar wave equation for beam propagation in nonlinear media. The numerical study of the nonlinear wave equation with and without the paraxial approximation reveals details of the beam propagation characteristics. However, a mathematically tractable method of approaching the subject is to assume that the beam maintains its Gaussian shape as it propagates through the nonlinear media. This is known as the constant-shape approximation which Marburger⁸⁹ examines in detail. It correctly predicts the qualitative features of the beam propagation but overestimates the nonlinearity. Nevertheless, it is a useful tool in studying the nonlinear propagation of beams in Kerr media.

An elliptic Gaussian beam is the general case of the well-studied circular beam. Elliptic beam propagation in a Kerr media has been investigated by Vorob'jev⁹⁰ and Schwarzburg⁹¹ in the early seventies and again twenty years later by Cornolti *et al.*⁹² The authors all used the Eikonal method of Akhmanov, giving similar predictions. Recently, a Lagrangian method was used in connection to

a beam-deflection experiment.⁹³ Both these methods have, in common, a pair of coupled second-order differential equations for the beam radii that need to be solved numerically in order to study the beam propagation.

In this appendix, we apply the well-known q -parameter formalism to study the propagation of elliptic Gaussian beams in Kerr-type media using the constant-shape approximation. This method was first applied by Yariv *et al.*⁹⁴ to study circular beam propagation in nonlinear media. The formalism provides two new features that is not possible with the Eikonal or Lagrangian methods: it allows us to (1) derive closed form expressions for the beam radii for incremental distances, and (2) identify an ellipticity-dependent critical power for self-focusing for each one-dimensional beam. There are some important differences in the manner which an elliptic beam propagates when compared to a circular beam. We graphically demonstrate what these differences are and show the equivalence of the q -parameter formalism to the Eikonal and Lagrangian methods

2. Theory

The starting point is the detailed theory presented in Chapter II. We can easily find expressions for the beam radii and radii of curvature for each of the beams within the medium by using Eq. II.8,:

$$w_{x,y}^2(z) = w_{x,y}^2(0) \left\{ \frac{\sin^2 \varphi_{x,y} z}{\varphi_{x,y}^2} \left(\frac{1}{R_{x,y}^2(0)} + \frac{1}{d_{x,y}^2(0)} \right) + \cos^2 \varphi_{x,y} z + \frac{\sin 2\varphi_{x,y} z}{R_{x,y}(0)\varphi_{x,y}} \right\}, \quad (\text{B.1})$$

$$\text{and } \frac{1}{R_{x,y}(z)} = \frac{w_{x,y}^2(0)}{w_{x,y}^2(z)} \left\{ \frac{\cos 2\varphi_{x,y} z}{R_{x,y}(0)} + \frac{\sin 2\varphi_{x,y} z}{2\varphi_{x,y}} \left(\frac{1}{R_{x,y}^2(0)} + \frac{1}{d_{x,y}^2(0)} - \varphi_{x,y}^2 \right) \right\}, \quad (\text{B.2})$$

where $d_{x,y} = \pi n_0 w_{x,y}^2(0) / \lambda$ is the diffraction length for each beam. The positions 0 and z should more accurately be replaced by z and $z + \Delta z$, i.e., these expressions hold for incremental distances. In addition, we can identify a critical power for self-focusing for each of the beams from Eq. B.1. If the incoming beams are parallel, then the following condition holds:

$$\frac{w_{x,y}^2(z)}{w_{x,y}^2(0)} = \cos^2 \phi_{x,y} z \left(1 - \frac{1}{\phi_{x,y}^2 d_{x,y}^2} \right) + \frac{1}{\phi_{x,y}^2 d_{x,y}^2}. \quad (\text{B.3})$$

Thus, $w_{x,y}$ becomes independent of z or is trapped initially when $\phi_{x,y}^2 d_{x,y}^2 = 1$ or, equivalently, when $P / P_{crx, cry} = 1$,

$$\text{where} \quad P_{crx} = \frac{\lambda^2}{8\gamma\pi n_0} \frac{w_y(0)}{w_x(0)} = P_{cr} e(0), \quad (\text{B.4})$$

$$\text{and} \quad P_{cry} = \frac{\lambda^2}{8\gamma\pi n_0} \frac{w_x(0)}{w_y(0)} = \frac{P_{cr}}{e(0)}. \quad (\text{B.5})$$

Here, P_{cr} is the critical power for self-focusing for a circular Gaussian beam which is independent of the beam radius and $e(0)$ is the initial ellipticity. Recall that from our definition of ellipticity, $e(0) \geq 1$.

To gain more insight into the beam propagation the evolution of the q -parameters are examined. By taking a differential variation of Eq. II.6, we find

$$\frac{d}{dz} \left(\frac{1}{q_{x,y}} \right) = -\frac{1}{q_{x,y}^2} - \frac{n_{2x,2y}}{n_0}, \quad (\text{B.6})$$

from which a pair of coupled differential equations are derived:

$$\frac{d^2 w_x}{dz^2} = \frac{4}{k^2} \left(\frac{1}{w_x^3} - \frac{P/P_{cr}}{w_x^2 w_y} \right) \quad (\text{B.7a})$$

$$\frac{d^2 w_y}{dz^2} = \frac{4}{k^2} \left(\frac{1}{w_y^3} - \frac{P/P_{cr}}{w_y^2 w_x} \right). \quad (\text{B.7b})$$

These equations governing the evolution of the beam radii are the fundamental equations derived by the Eikonal and Lagrangian methods. The similarity of the above equations to that of the Newtonian mechanics suggests that the beam evolution can be viewed of as a particle of mass $k^2/2$ moving in a potential U given by

$$U = \frac{1}{w_x^2} + \frac{1}{w_y^2} - \frac{2P/P_{cr}}{w_x w_y}. \quad (\text{B.8})$$

By taking ϕz to be small in Eq. B.1, we derive an important relationship between the beam radii during propagation:

$$w_x^2 + w_y^2 = 4Hz^2/k^2 + 2z(w_{x0}\dot{w}_{x0} + w_{y0}\dot{w}_{y0}) + w_{x0}^2 + w_{y0}^2, \quad (\text{B.9})$$

$$\text{where} \quad H = \frac{k^2(\dot{w}_{x0}^2 + \dot{w}_{y0}^2)}{4} + \frac{1}{w_{x0}^2} + \frac{1}{w_{y0}^2} - \frac{2P/P_{cr}}{w_{x0}w_{y0}}. \quad (\text{B.10})$$

Here, H is the Hamiltonian of the system and the z dependence of $w_{x,y}$ is to be understood. The following replacements have been made: $w_{x,y}(0)$ with $w_{x0,y0}$ and $\dot{w}_{x0,y0} = dw_{x,y}/dz|_{z=0} = w_{x0,y0}/R_{x0,y0}$. Note that $w_{x0,y0}$ is equal to the minimum beam radii $w_{0x,0y}$ when the initial beam is parallel. The relationship expressed by Eq. B.9 can also be derived from Eqs. B.7a and B.7b.

To make the analysis easier, we will hereafter assume the incoming beam to be parallel ($\dot{w}_{x0} = \dot{w}_{y0} = 0$). The first interesting finding is that if $H = 0$, then the elliptic beam will oscillate indefinitely. The power for this beam trapping is

$$P_{trap} = \frac{1}{2}(e_0 + 1/e_0)P_{cr}. \quad (\text{B.11})$$

However, if the power is greater than P_{trap} , then the beam will focus at a distance z_f given by

$$z_f = \frac{k}{2} \sqrt{\frac{w_{0x}^2 + w_{0y}^2}{\frac{2P/P_{cr}}{w_{0x}w_{0y}} - \frac{1}{w_{0x}^2} - \frac{1}{w_{0y}^2}}} \quad (\text{B.12})$$

3. Theoretical Results

We graphically investigate the propagation of elliptic Gaussian beams as a function of input power. Our formalism provided us with separate critical powers of self-focusing for each of the beams. Cornolti *et al.*⁹² have already shown the effects of two other powers on the propagation, namely, $P = P_{trap} + P_{cr}$ and $P = 2P_{trap}$ and we will not rederive their results. For illustration, we take an elliptic beam with initial beam radii $w_y = 2$ mm and $w_x = 0.5$ mm and a positive non-linearity such that the $P_{cr} = 10$ KW. Thus, the critical powers for focusing the individual beams are $P_{crx} = 40$ KW and $P_{cry} = 2.5$ KW and the beam trapping power is $P_{trap} = 21.25$ KW. In Fig. B.1a, $P = P_{cry}$ and the y beam initially gets trapped but then diverges. However, when $P_{cry} < P < P_{trap} < P_{crx}$ the y beam and depending on the power the x beam oscillates as shown in Figs. B.1b-c. The beams become trapped when $P = P_{trap}$ and the ellipticity is shown (Fig. B.1d) to oscillate between two extrema e_0 and $1/e_0$. When $P > P_{trap}$, the beams will oscillate and then focus as in Fig. B.2a. However if $P = P_{trap} + P_{cr}$, then the beams focus with no crossing (Fig. B.2b). Interestingly, when $P = 2P_{trap}$ the beam focuses with constant ellipticity as shown in Fig. B.2c. In all the above cases, the beam ellipticity never exceeded its initial value during propagation. This condition is violated when $P > 2P_{trap}$ as shown in Fig. B.2d.

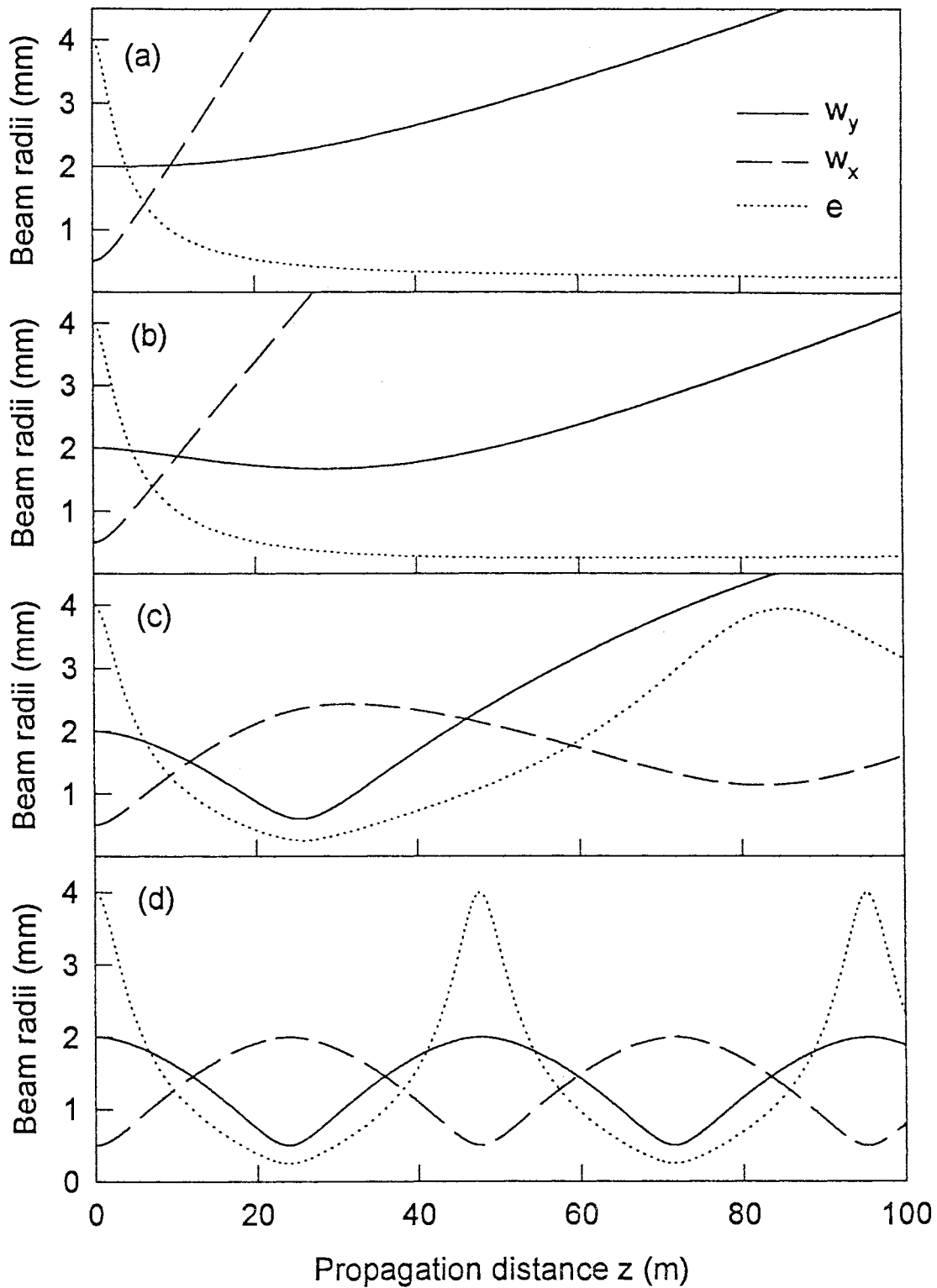


Figure B.1 Elliptic beam propagation in Kerr media. $P_{crx}=40$ KW, $P_{cry}=2.5$ KW, $P_{cr}=10$ KW, $P_{trap}=21.25$ KW. In (a) $P=2.5$ KW, (b) $P=10$ KW, (c) $P=20$ KW, and (d) $P=21.25$ KW.

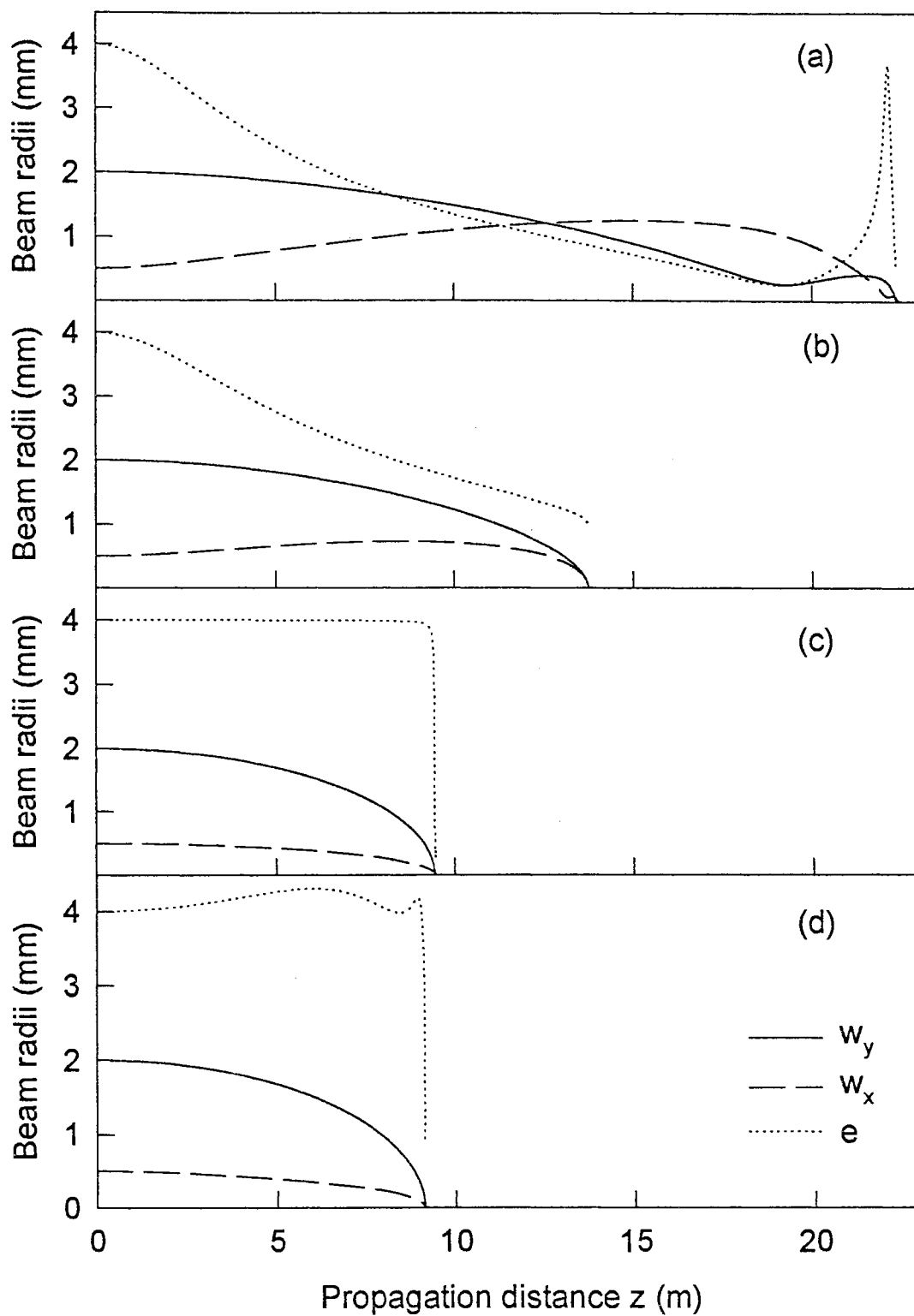


Figure B.2 Elliptic beam propagation in Kerr media. $P_{crx}=40\text{KW}$, $P_{cry}=2.5\text{KW}$, $P_{cr}=10\text{KW}$, $P_{trap}=21.25\text{KW}$. In (a) $P=22\text{KW}$, (b) $P=31.25\text{KW}$, (c) $P=42.5\text{KW}$, and (d) $P=44\text{KW}$.

APPENDIX C

MULTI-PASS TANDEM FABRY-PEROT INTERFEROMETER

An FP interferometer consists of two plane mirrors that are highly polished (typically $\lambda/100$ or better) and are held very parallel to each other. One is usually fixed and the other is movable. If the mirrors are separated by a distance L , then the transmission T is given by

$$T = \frac{T_{\max}}{1 + (4F^2 / \pi^2) \sin^2(2\pi L/\lambda)} \quad (\text{C.1})$$

where, T_{\max} is the maximum possible transmission which is determined by system losses, and F is the finesse which is a quality factor that depends primarily on mirror reflectivity and flatness. From Eq. C.1, it is clear that only the wavelengths λ that satisfy the standing wave condition of $L = \frac{1}{2} p\lambda$, where p is an integer, will transmit. If the spacing L is varied, the FP will transmit light at different wavelengths and can thus be used as a spectrometer. A typical FP transmission is shown with three orders in Fig. C.1. The spacing between the transmission peaks $\Delta\lambda$ is called the free spectral range (FSR) and the full-width at half maximum of the peak $\delta\lambda$ determines the resolution. The finesse of the FP is defined as, $F = \Delta\lambda/\delta\lambda$. It is important to point out that the FP will transmit all light satisfying the standing wave criteria; so the observed spectra must lie

sirable to have a FSR large enough to encompass the spectrum of interest. However, by increasing the FSR, we decrease the resolution.

This is when the tandem operation of two FP interferometers becomes useful, i.e., operating two FP interferometers one after the other. Each FP transmits independently and their transmission will depend on their individual mirror spacing (See Fig. C.1). If the ratio of the mirror spacing of one FP to the other is always a constant, then the transmission from the tandem system will be a combination of the two spectra. It is easy to see from Fig. C.1 that the central peak of both the FP interferometers will combine but the side peaks will cancel one another, i.e., when one FP transmits the other does not. What remains is a central transmission peak with several “ghost” peaks arising from the minute transmission overlap of the side orders. The side peaks will eventually align and give rise to another transmission peak but this will occur after many orders (about 20 in our case). Thus, we can increase the FSR while maintaining the same resolution.

We spectrally analyzed the signal from our Brillouin scattering experiments using a multi-pass tandem Fabry-Perot interferometer developed by Dr. J. R. Sandercock. Traditional FP interferometers suffer from nonlinear scans, mirror tilting during the scan, and stability problems and they are not particularly suitable for tandem operation. Changing the mirror spacing is also tedious. These difficulties are not present in the Sandercock design. This system makes use of a compound translation stage for scanning which is the key element that makes this design superior to other systems. Complete details of the interferometer construction and operation can be found in the manual⁹⁵ and our supplementary notes.⁹⁶ However, we do highlight some of the design features so that the basic operating and alignment procedures become clearer. All instruments necessary

for monitoring and stabilizing the FP came with the system. There are two FP interferometers in the Sandercock system which are operated in tandem to give the high resolution needed for Brillouin scattering. The arrangement of the mirrors are shown in Fig. C.2. There is a deformable parallelogram at the base of the compound translation stage on which the two scanning mirrors are placed. It is acted upon by a single piezoelectric transducer which ensures that the mirrors will always scan synchronously and linearly.

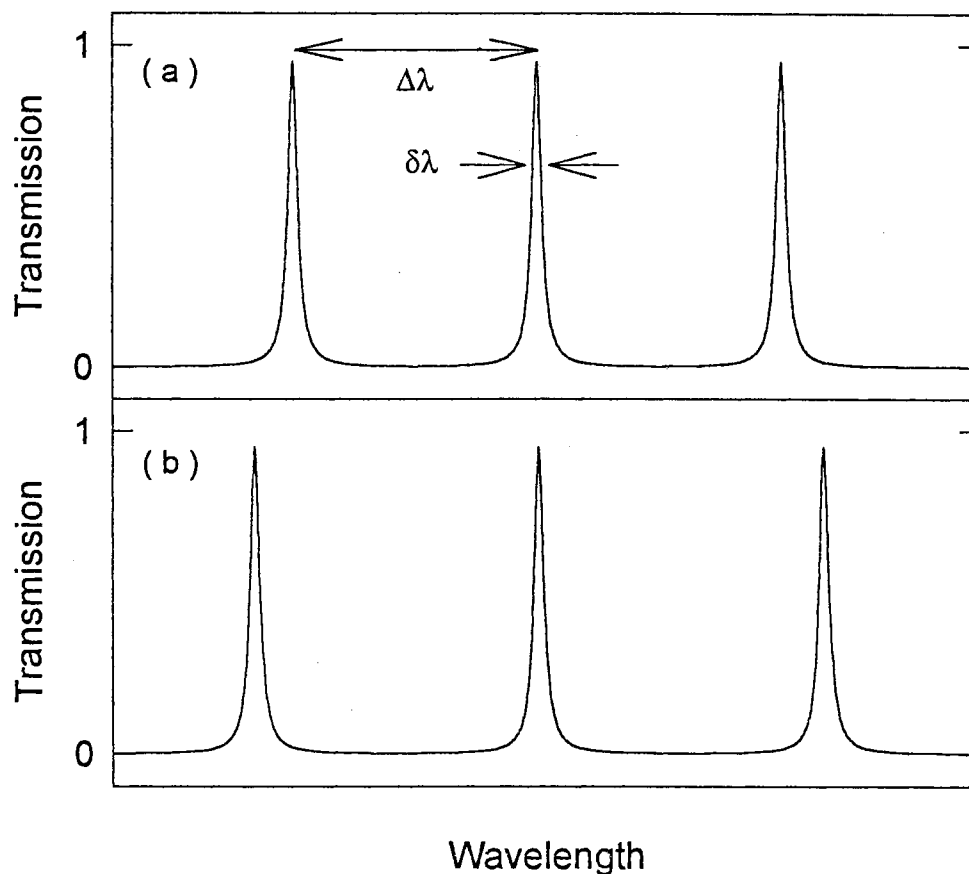


Figure C.1 A transmission spectrum of a Fabry-Perot interferometer. $\Delta\lambda$ is the free spectral range and $\delta\lambda$ is the full-width at half maximum. The length of the cavity in (a) is larger than that of (b). In a tandem system, both the transmissions spectra from (a) and (b) combine to give a large free spectral range and high resolution.

This is used for small scanning displacements, typically less than $3\ \mu\text{m}$. The deformable parallelogram stage rests on a crossed roller translation stage that is used for large mirror spacing displacements, typically several millimeters. All parts of the mirrors move to within a few angstroms during a scan of $3\ \mu\text{m}$ and about $0.5\ \mu\text{m}$ during a large mirror spacing displacement of a few millimeters. Furthermore, the relative spacing of the two FP interferometers is always within $2\ \text{nm}$ and is maintained during scanning. This level of stability can not be achieved with the traditional FP.

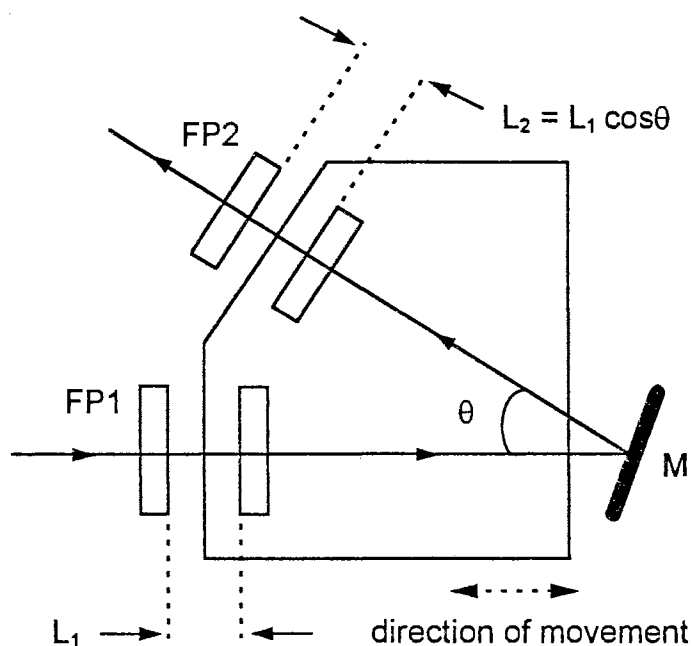


Figure C.2 Compound translation stage of the FP interferometer with two mirrors mounted on the stage. The ratio of L_1 to L_2 is fixed. Both FP's always scan synchronously.

interferometers operating in tandem. Another impressive feature is that we can scan up to ten orders with each order being identical.

The first interferometer (FP1) spacing is monitored with a capacitor and is displayed to within 5 μm on a micrometer gauge on the side of the interferometer box. We therefore know the mirror spacing very accurately and do not have to indirectly calculate it using known Brillouin shifts of a standard sample such as fused quartz. The scattered light passed through both FP mirrors three times (multi-pass) and through many other optical elements before going into the light detection system. Such multi-passing greatly enhances the contrast or signal to noise. The interferometer control unit had knobs to finely adjust the vertical and horizontal orientation of the nonscanning interferometer mirrors and also the relative spacing between the interferometers. A coarse adjustment of these mirror orientations and separation were placed on the side of the "light-tight" interferometer box in the form of toggle switches.

A light modulator in the form of a mechanical shutter also came with the FP system. It was mounted on the outside of the interferometer opening and had a variable pinhole entrance on the front face and a diffuser on one of the side faces. A weak reference beam was guided on to the diffuser where a beam splitter inside the modulator directed it to the FP mirrors. The modulator would be timed such that when the strong Rayleigh signal from the sample was about to be scanned the shutter would open and let the reference beam through while blocking the signal from the sample. This was always used during our experiments. There is also an output pinhole within the interferometer box which is set to be 1.5 times larger than the input pinhole. The setting of both pinholes determines the overall finesse.

A unique and very useful feature of the Sandercock system was the ability to align both FP mirrors without having to even open the interferometer box. That is, the alignment could be done electronically from outside the interferometer. The reference beam was always used for this purpose. This was accomplished with a set of optics that could be moved in and out of the beam path leading to the mirrors. The optics would guide the reflected signal into the detection system and the mirrors could be aligned in reflection mode. The reflection spectra looked like a high background plateau punctuated with sharp valleys representing the transmission of the FP mirrors. Such a spectra is shown in Fig. C.3 with two orders from both FPs. The second interferometer (FP2) was deliberately misaligned so that we could calculate the correspondence of the FSR of FP1 with the channel numbers of the data acquisition system.

In practice, we would use the interferometer controls to maximize the depth of the transmission valleys and then adjust the relative spacing of the two FP interferometers such that the valleys of one pair would coincide. The system would be then switched to transmission mode by moving the alignment mode optics out of the way. The single resulting transmission peak would then be moved to the middle of the scan and improved upon by the fine adjustments on the interferometer control unit. The stabilizers were then turned on and a window would be set on the spectra covering the central peak to blank out the Rayleigh line during scanning.

The overall performance of the FP interferometer can be checked by looking at the Brillouin scattered light from Plexiglas[®]. In a backscattering geometry, the Brillouin shifts of the LA phonons (TA phonons are not allowed in backscattering) should be at 0.547 cm^{-1} , and should give 5-10 cts/ms/mW (5 is

more common). We always measured 3-4 cts/ms/mW due to the low quantum efficiency of the PMT.

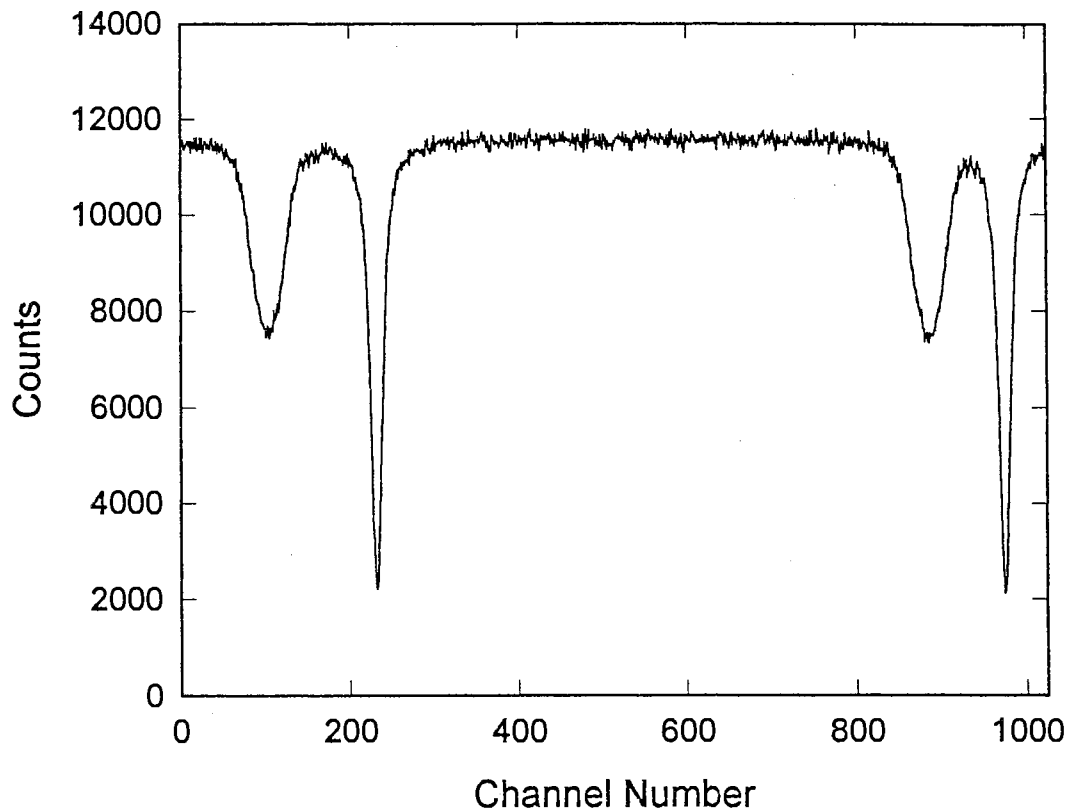


Figure C.3 Reflection spectra of the tandem FP interferometer. The smaller peak is that of FP2 and was deliberately misaligned. The separation of the FP1 valleys was recorded. This allowed us to make a correspondence between the channel numbers of the multichannel analyzer and our FSR

We conclude this FP section by showing a high quality scan of a silicon wafer (001) that was taken in a back-scattering geometry (Fig. C.4). The results agree with those taken by Sandercock⁹⁷ and are discussed in detail in his paper. The longitudinal, transverse, surface phonons and the central mode along with the Rayleigh peak are clearly seen. The laser power at the sample was 60 mW. The incident light was horizontally polarized and hit the sample at the Brewster's angle of 76° . The scattered light collected was unpolarized.

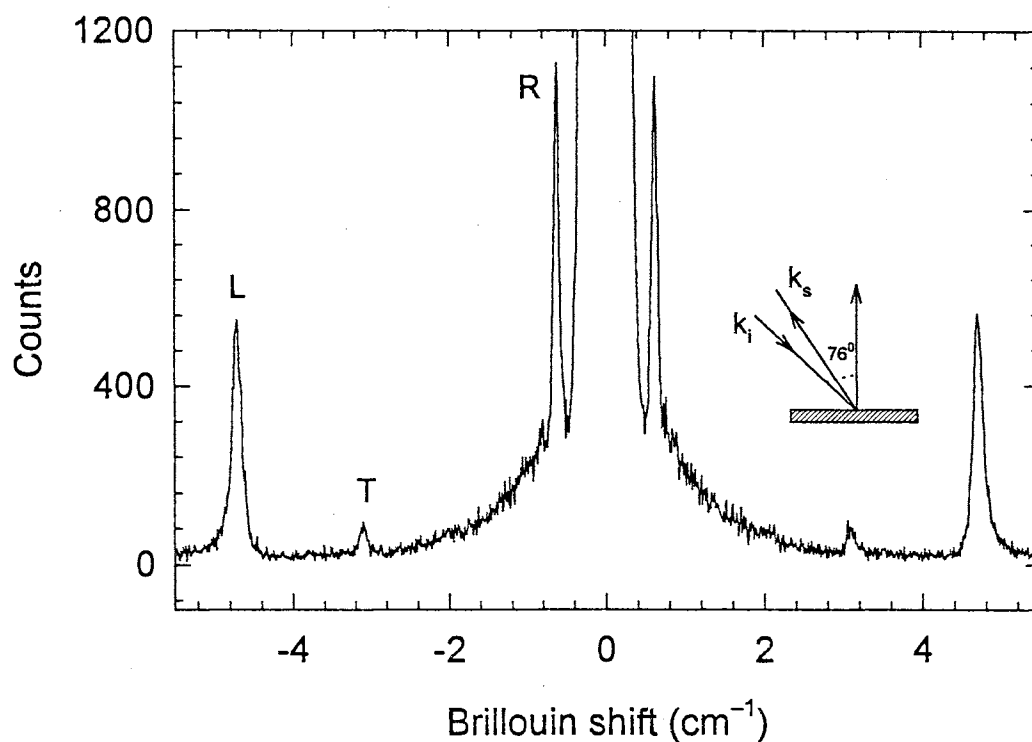


Figure C.4 Brillouin spectra of Si (001) showing bulk transverse (T) and longitudinal (L), surface phonon (R), and central mode with the Rayleigh line using 514.5 nm. The sample is opaque at this wavelength.

2

VITA

SHABBIR M. MIAN

Candidate for the Degree of

Doctor of Philosophy

Thesis: NONLINEAR OPTICAL PROPERTIES OF LEAD SILICATE
AND EUROPIUM-DOPED ALKALI-SILICATE GLASSES

Major Field: Physics

Biographical:

Personal Data: Born in Dhaka, Bangladesh, on July 14, 1969, the son of
Abdul Jalil and Hasina Mian.

Education: Received Bachelor of Arts degree in Physics and Mathematics
from Berea College, Berea, Kentucky, in May 1990. Completed the
requirements for the Doctor of Philosophy degree with a major in
Physics at Oklahoma State University, Stillwater, Oklahoma, in
December 1996.